

Project No. 10-94

**MITIGATION OF WELDMENT CRACKING OF
HIGHWAY STEEL STRUCTURES DUE TO THE
GALVANIZING PROCESS**

FINAL REPORT

**Prepared for
NCHRP
Transportation Research Board**

of

The National Academies of Sciences, Engineering, and Medicine

**Caroline Bennett
Jian Li,
The University of Kansas
Lawrence, KS**

**Adolfo Matamoros
University of Texas San Antonio**

Permission to use any unoriginal material has been
obtained from all copyright holders as needed.

ACKNOWLEDGEMENT OF SPONSORSHIP

This work was sponsored by one or more of the following as noted:

- American Association of State Highway and Transportation Officials, in cooperation with the Federal Highway Administration, and was conducted in the National Cooperative Highway Research Program,
- Federal Transit Administration and was conducted in the Transit Cooperative Research Program,
- Federal Aviation Administration and was conducted in the Airport Cooperative Research Program,
- Research and Innovative Technology Administration and was conducted in the National Cooperative Freight Research Program,
- Pipeline and Hazardous Materials Safety Administration and was conducted in the Hazardous Materials Cooperative Research Program.
- Federal Railroad Administration and was conducted in the National Cooperative Rail Research Program,

Which is administered by the Transportation Research Board of the National Academies.

DISCLAIMER

This is an uncorrected draft as submitted by the Contractor. The opinions and conclusions expressed or implied herein are those of the Contractor. They are not necessarily those of the Transportation Research Board, the National Academies, or the program sponsors.

CONTENTS

1	Appendix A: Description of Current Practice
18	Appendix B: Literature Review
47	Appendix C: Stress-Strain Curves
61	Appendix D: Supporting Results for Computational Simulations

APPENDIX A

Description of Current Practice

A comprehensive literature review was performed in Task 1 of 10-94, and an extensive summary of findings based upon review of technical articles is provided in Appendix B. Individual studies have also been referenced throughout the main body of this report. In the following sections, a concise review of relevant national and international standards and specifications, state DOT practices (including materials selection, geometric detailing, welding procedures, and galvanizing procedures), Galvanizers' bath selections, and two case studies are provided.

Relevant National and International Specifications and Standards

The primary standards / specifications in the United States, as well as other countries, that are relevant to the problem of weldment cracking of highway structures due to the galvanizing process are listed in the following, and relevant provisions are discussed.

AASHTO LRFD Specifications for Structural Supports for Highway Signs, Luminaires, and Traffic Signals (AASHTO, 2015)

The AASHTO LRFD Specifications for Structural Supports for Highway Signs, Luminaires, and Traffic Signals (referred to herein as the "AASHTO Sign Specifications") contains provisions that govern the design of welded highway structures pertinent to the 10-94 project. The AASHTO Sign Specifications cover all structures applicable to 10-94 except for bridge superstructures. Chapter 5 of the AASHTO Sign Specifications provides minimum requirements for steel structures, and largely focuses on geometric and welding requirements.

Regarding material selection, the AASHTO Sign Specifications note that: "Grades of steel listed in the Standard Specifications for Highway Bridges are applicable for welded structural supports for highway signs, luminaires, and traffic signals." Other steels are permitted to be used, as deemed acceptable by the user. For steels thicker than 0.5 in., Section 5.4 includes a provision that the main load carrying tension members must meet the Charpy V-Notch impact requirements in the Standard Specifications for Highway Bridges. Overall, the material requirements within the AASHTO Sign Specifications are really quite broad, and leave great discretion to the owner in assigning acceptable material grades.

Tubular structures are permitted to be round or multisided. However, the AASHTO Sign Specifications acknowledge that multisided tubular structures may be more susceptible to in-service fatigue cracking due to stress concentrations at the bend corners based on work performed by (Roy, 2011). Therefore, the provisions in Section 5.6.2 include a minimum requirement for number of sides (AASHTO Eqn 5.6.2-1) and a minimum internal bend radius of five times the tube wall thickness or 1.0 in., whichever is larger. The minimum number of sides for multisided tubular sections is summarized here in Table A-1.

Table A-1: Minimum number of sides for multisided tubular sections, adapted from (AASHTO, 2015)

Tube Diameter, D	Minimum Number of Sides
Up to 13 in.	8
Greater than 13 in. and up to 28 in.	12
Greater than 28 in. and up to 50 in.	16

In addition to acknowledging the potential for sharp bend radii to lead to fatigue failures, the Commentary to Section 5.6.2 also notes that sharp bend radii may be susceptible to strain-age embrittlement, cold-worked embrittlement, and hydrogen embrittlement, which may be associated with early fatigue cracking in-service. The Commentary discussion suggests that a minimum bend radius of five times the tube wall thickness can mitigate the possibility of such embrittlement. Finally, the Commentary also discourages use of square and rectangular cross-sections due to higher incidences of fatigue cracking.

Section 5.6.3 of the AASHTO Sign Specifications specifies minimum thickness for transverse plates, which includes base plates attached to pole structures; these minimums have been shown in Table A-2. The reasoning for specifying minimum base plate thickness is to improve the fatigue strength of the welded connection between the tube and base plate.

Table A-2: Minimum transverse plate thickness for tube-to-transverse-plate connections, adapted from (AASHTO, 2015)

Tube Diameter, D	Minimum Transverse Plate Thickness
Up to 8 in.	1.5 in.
Greater than 8 in.	2.0 in.

Geometric requirements for stiffened socket-type connections are provided in Section 5.6.4, and for backing rings in Section 5.6.5.

As stated in Section 5.14 of the AASHTO Sign Specifications, welded connections for structural supports for highway signs, luminaires, and traffic signals are governed by the AWS Structural Welding Code D1.1 – Steel (AWS, 2010). As covered in Section 14.4.4.6 of the AASHTO Sign Specifications, “Tube-to-Transverse-Plate Connection Welds,” either a full-penetration groove weld or a socket-type joint with two fillet welds may be used. When fillet welds are used, unequal-leg geometries are specified for the tube-to-transverse plate connection, with the longer leg contacting the tube surface at 30 deg. The fillet weld details described are required with the intent of improving the connection’s fatigue performance over that which would be achieved using equal-leg fillet welds. After fabrication (but before galvanizing), all welds are to be visually inspected, and all full-penetration groove welds must be inspected through magnetic-particle (Vincent) or ultrasonic testing (UT), depending upon the thinnest material. If the thinnest material is less than ¼-in. thick, then MT is to be used. Otherwise, UT is to be used. The owner may alternatively specify that radiographic testing or destructive testing. After galvanizing, full-penetration welds connecting a tube-to-base plate that have a constant-amplitude fatigue threshold of 10 ksi or less are to undergo UT inspection for toe cracks. A required length of all partial-penetration groove welds and fillet welds are to be inspected for a random 25% of structures post-galvanization.

Section 14.4.7.3 of the AASHTO Sign Specifications, “Galvanized Structures,” provides some minimal requirements for galvanizing steel structures. The provisions state that “hot-dip galvanizing shall conform to the requirements of AASHTO M111 (ASTM A123).” Additionally, a preference regarding the silicon content of the steel material is made: “Tubular steel pole shafts to be galvanized preferably shall have a silicon content equal to or less than 0.06 percent. Other components, such as base plates, should have silicon content controlled as required to prevent detrimental galvanizing effects.” It is noted that these provisions regarding the silicon content of the steel are currently not requirements.

AASHTO-LRFD Bridge Design Specifications (AASHTO, 2017)

The AASHTO-LRFD Bridge Design Specifications govern the design of new steel bridge superstructures. The AASHTO-LRFD Bridge Design Specifications refer to AWS D.15, The Bridge Welding Code, for welding procedures. Galvanizing of steel bridge superstructures is not explicitly addressed in the Specification.

ASTM A123: Standard Specification for Zinc (Hot-Dip Galvanized) Coatings on Iron and Steel Products (ASTM, 2013a)

ASTM A123 is equivalent to AASHTO M111, and is the general specification governing galvanized coatings on steel structures. This specification provides required thicknesses and finish requirements of the zinc coating for various coating grades, and covers how to evaluate whether standards have been met in physical structural specimens. All state DOT specifications refer to ASTM A123 (AASHTO M111) in their specifications for galvanizing requirements.

ASTM A123 refers to ASTM B6 for the zinc material used in the galvanizing bath, but does allow galvanizers to add trace amounts of “certain elements” to the galvanizing bath to enhance the finish of the galvanized product, so long as the bulk chemistry of the galvanizing bath remains at least 98% zinc by weight. Stated examples of elements that might be added to the galvanizing bath include aluminum, nickel, and tin.

ASTM A143: Standard Practice for Safeguarding Against Embrittlement of Hot-Dip Galvanized Structural Steel Products and Procedure for Detecting Embrittlement (ASTM, 2007)

ASTM A143 focuses on prevention of embrittlement phenomenon (strain-aging, hydrogen, and cold-working) throughout the hot-dip galvanizing process, and also provides test procedures for detecting embrittlement.

With regard to minimizing embrittlement produced by cold-working, ASTM A143 suggests that a cold-bending radius of three times (3x) the section thickness will usually ensure satisfactory performance. When necessitated, it notes that thermal treatment may be applied before the steel is galvanized. For members that have been subjected to cold-bending, the specification suggests a maximum of 1100 °F to avoid excessive grain growth, or to fully normalize the steel by performing the heat treatment in a range of 1600-1700 °F.

ASTM A143 states that when hydrogen embrittlement is a concern, heating the steel element to 300 °F after pickling and before galvanizing should aid in expelling any hydrogen absorbed during the acid pickling process. When concerns include the potential for over-pickling or when very high strength steel is used ($F_u > 150$ ksi), an alternative to acid pickling (abrasive blast cleaning and flash pickling) may be used.

ASTM A143 states that the responsibility for avoiding embrittlement phenomenon rests with the designer. A simple bend test is prescribed in ASTM A143 for testing specimens that have completed the galvanizing process, allowing the tester to compare the performance of the galvanized steel to that of black steel in terms of the degree of bending sustained. A separate test is provided for steel angles.

The test procedures described in ASTM A143 do not appear to be easily applied to the types of galvanized welded steel highway structures being studied in 10-94 (sign structures, luminaires, traffic structures, bridge superstructures). Additionally, the test methods cannot capture the effects of liquid metal assisted cracking (LMAC), often referred to as liquid metal embrittlement (LME). Finally, the ASTM A143 specifications appear to have been adopted by only one of the 50 State DOTs.

AWS D1.1: Structural Welding Code

AWS D1.1 provides a set of comprehensive requirements in design, qualification, fabrication, and inspection of weldments for both tubular and nontubular steel structures. The former is directly applicable to highway sign, luminaire, and traffic signal structures. A concise summary of requirements pertinent to the 10-94 project are presented here.

To prevent local buckling or other local failure modes, for circular sections, AWS D1.1 requires that the diameter/thickness ratio shall be less than $3300/F_y$ [for F_y in ksi].

To improve fatigue behavior of tubular structures, AWS D1.1 specifies that “the toe of weld may be peened with a blunt instrument, so as to produce local plastic deformation which smooths the transition between weld and base metal, while introducing a compressive residual stress.”

In terms of base-metal notch toughness requirement, for tubular sections used as a main member in structural nodes under cyclic or fatigue loading, it is required to “demonstrate CVN test absorbed energy of 20 ft·lb [27 J] at the Lowest Anticipated Service Temperature (LAST),” for base-metal thicknesses of 2 in. or greater or base-metal thicknesses of 1.0 in. or greater with a specified yield strength of 50 ksi or greater.

To avoid cold cracking, AWS D1.1 provides two methods in Annex I which include HAZ hardness control and hydrogen control. The HAZ hardness control method is restricted to fillet welds and is based on the assumption that cracking can be prevented if the hardness of the HAZ is kept below certain critical value. The critical hardness depends on a number of factors such as steel type, hydrogen level, restraint, and service conditions. To control the HAZ hardness, the cooling rate is restricted below a critical value based on the hardenability of the steel. On the other hand, the hydrogen control method is mainly based on results of restrained PJP groove weld tests. This method estimates the preheat necessary to allow enough hydrogen to diffuse out of the joint so that the average hydrogen quantity in the join is below a critical value after it has cooled down to about 120 °F.

AWS D1.5: Bridge Welding Code

The AWS D1.5 governs welding fabrication for welded highly steel bridges and bridge components. It is not applicable to structures composed of structural tubing, for which the AWS D1.1 should be followed.

Japanese Standard JIS G 3129: High tensile strength steel for tower structural purposes (JIS, 2005)

While the JIS G 3129 standard applies to a very specific type of structure, this Japanese standard is notable and pertinent to the 10-94 project for its inclusion of a crack sensitivity equivalent for hot-dipped zinc coatings, *CEZ* (JIS, 2005), as shown in Equation A-1.

$$CEZ = C + \frac{Si}{17} + \frac{Mn}{7.5} + \frac{Cu}{13} + \frac{Ni}{17} + \frac{Cr}{4.5} + \frac{Mo}{3} + \frac{V}{1.5} + \frac{Nb}{2} + \frac{Ti}{4.5} + 420B \quad \text{Equation A-1}$$

$$\leq 0.44\%$$

The purpose of the CEZ expression is to limit susceptibility to LMAC during the galvanizing process by closely controlling the steel chemistry.

Japanese Standard JIS H 8641: Hot dip galvanized coatings (JIS, 2007)

The JIS H 8641 governs the general aspects of hot-dip galvanizing steel structural components in Japan. It is the Japanese equivalent to ASTM A123. Relevant areas in which the JIS H 8641 standard differs from the ASTM A123 standard are:

- The galvanizing bath must be at least 97.5% pure zinc (compared against 98% in the ASTM A123 standard)
- The JIS standard encourages control of the steel substrate being galvanized: “For the substrate, the quality of material shall be clarified beforehand for preventing the abnormal dispersion in quality of material coating. Moreover, especially the silicon (Si) and phosphorus (P), among the chemical components of substrate, influence greatly the quality of material of coating, therefore their quantities should be confirmed.”

The JIS standard also discourages:

- Welded connections between plates having extreme differences in thickness. However, it does not quantify what is meant by “extreme differences in thickness.”
- Structural combinations of dissimilar metals.
- Large residual stresses. The JIS standard instructs that the residual stress should be removed through use of an adequate heat treatment.

British Standard BS EN ISO 1461: Hot dip galvanized coatings on fabricated iron and steel articles – Specifications and test methods (BS, 2009a)

The BS EN ISO 1461 governs the general aspects of hot-dip galvanizing steel structural components in the United Kingdom, and is a European Standard. It is the UK equivalent to ASTM A123. Relevant areas in which the BS EN ISO 1461 standard differs from the ASTM A123 standard are:

- The galvanizing bath must be at least 98.5% pure zinc by mass (compared against 98% in the ASTM A123 standard)
- The composition and any properties of the basis metal that might affect hot-dip galvanizing, including specification for the steel supply condition, must be provided if requested by the purchaser.
- The presence of flame-cut, laser-cut, or plasma-cut surfaces on the work must be information that is provided to the purchaser if requested.

British Standard BS EN ISO 14713: Zinc coatings – Guidelines and recommendations for the protection against corrosion of iron and steel in structures (BS, 2009b)

The BS EN ISO 14713 provides guidelines and recommendations regarding the general principles of design for articles to be hot-dip galvanized. This particular standard is another European Standard, in this case adopted as a UK National standard. This is a rich standard, with a number of provisions that are relevant to the problem being addressed in 10-94. A summary of the most relevant provisions are provided here, with attention focused on topics that are not necessarily present (or that are described to a lesser degree) in ASTM A123 and ASTM A143.

- Whenever possible, articles should be designed to enable coating in a single application.
- The BS EN ISO 14713 standard makes note of the fact that some elements in steel chemistries negatively impact the galvanized coating (silicon and phosphorus are given as examples), as shown in Table A-3.

Table A-3: Coating characteristics related to steel composition (adapted from Table 1 of BS EN ISO 14713) (BS, 2009b)

Category	Typical levels of reactive elements	Additional information	Typical coating characteristics
A	<0.04% Si and <0.02%P	See Note 1	
B	0.14%Si to 0.25%Si	Fe/Zn alloy may extend through to the coating surface. Coating thickness increases with increasing silicon content. Other element may also affect steel reactivity. In particular, phosphorus levels greater than 0.035% will give increased reactivity	Coating has a shiny appearance with a finer texture. Coating structure includes outer zinc layer.
C	> 0.04%Si to <0.14%Si	Excessively thick coatings may be formed	Coating has a darker appearance with a coarser texture. Iron/zinc alloys dominate coating structure and often extend to the coating surface, with reduced resistance to handling damage.
D	>0.25%Si	Coating thickness increases with increasing silicon content	

Note 1) Steels with compositions satisfying the formula $Si + 2.5P \leq 0.09\%$ are also expected to exhibit these characteristics. For cold-rolled steels, these characteristics are expected to be observed when the steel composition satisfies the formula $Si + 2.5P \leq 0.04\%$.

Note 2) The presence of alloying elements (e.g. nickel) in the zinc melt can have a significant effect on the coating characteristics indicated in this table. This table does not provide relevant guidance for high-temperature galvanizing (i.e., immersion in molten zinc at 530°C to 560°C)

Note 3) The steel compositions indicated in this table will vary under the influence of other factors and the boundaries of each range will vary accordingly.

- Distortion cracking is discussed in the BS EN ISO 14713 standard as being a potential source of cracking when internal stresses (including residual and thermal) overcome the tensile resistance of the article being dipped. The standard points the user to rely on past experiences to avoid this source of cracking from occurring. It is also acknowledged that the problem may be exacerbated for high-strength steels ($F_y > 95$ ksi), and that some of these effects might be mitigated through stress relieving treatment before pickling / dipping.
- BS EN ISO 14713 addresses hydrogen embrittlement by stating that “Structural steels are not normally embrittled by the absorption of hydrogen during pickling, and hydrogen remaining (if any) does not, in general, affect structural steels. With structural steels, absorbed hydrogen is discharged during hot-dip galvanizing. If steels are harder than approximately 34 HRC, 340 HV, or 325 HB, care is necessary to minimize hydrogen absorption during surface preparation. The welds and heat affected zones (HAZ) of structural steels do not normally exceed a hardness value of 340 HV. Consequently these zones are not normally embrittled by the absorption of hydrogen during pickling.” (BS, 2009b)
- BS EN ISO 14713 addresses cold-working induced embrittlement by instructing the user to keep local cold deformations as low as possible through design and fabrication sequences. When this is not possible, heat treatment is recommended to relieve stresses before pickling / dipping is suggested. Additionally, the standard instructs that deleterious effects from cold-working embrittlement can be avoided by selecting steel with good toughness properties.
- The standard acknowledges LMAC as a source of brittle cracking during hot-dip galvanizing, but little direct guidance is offered.

German Standard DIN EN ISO 1461: Hot dip galvanized coatings on fabricated iron and steel articles – Specifications and test methods (DN, 2009)

The DIN EN ISO 1461 standard governs the general aspects of hot-dip galvanizing steel structural components in Germany, and is a European Standard. It is identical to the BS EN ISO 1461 standard. Therefore, relevant areas in which the DIN EN ISO 1461 standard differs from the ASTM A123 standard are not duplicated here.

DASSt-Richtlinie 022: Guideline for hot-dip-zinc-coating of prefabricated load-bearing steel components (DASSt, 2009)

DASSt-Richtlinie 022 is a German guideline aimed at mitigating cracks from forming in steel structure components during the hot-dip galvanizing process. In comparison to US standards, it is most analogous to ASTM A143. The DASSt guideline is intended to supplement the European Standard EN ISO 1461 by specifying the composition of the zinc alloy and the execution of the zinc-coating process with regard to the type of steel component, structural detailing, and fabrication processes. Therefore, the DASSt-Richtlinie 022 guideline is highly applicable to the research being conducted in 10-94.

The DASSt guideline is applicable to the following EN steel grades, with minimum yield strength shown here for context: S235 (33 ksi), S275 (36 ksi), S355 (50 ksi), S420 (60 ksi), S450 (65 ksi), and S460 (67 ksi).

The fundamental approach of the DASSt guideline is to control strains that occur in a steel element being galvanized such that they remain less than the strain capacity of the element. This is expressed in the DASSt guideline as:

$$\varepsilon_E < \varepsilon_R \quad \text{Equation A-2}$$

where ε_E is the strain demand, including the residual strains in the member being dipped and ε_R is the strain capacity (ultimate strain) of the steel material in the zinc.

The DASSt guideline allows for two means of meeting this requirement:

1. Using a simplified procedure that involves classification of the prefabricated steel element into various “Construction Classes” (dependent on cross-section depth, material strength, and toughness), “Detail Classes” (dependent upon local strain requirements, in turn dependent upon geometric detailing), and “Thickness Classes” (dependent upon thickness of the product, which is associated with the dip holding time). Use of the simplified procedure is contingent upon complying with a series of conditions pertaining to the design, detailing, and fabrication procedures; preparation of the steel before dipping; zinc alloy; dipping process; and inspection criteria.
2. A numerical assessment of Eqn. 2 may be performed using the provisions in Annex 4. The numerical assessment procedure is quite complicated, and can require testing of long-notch tension specimens (LNT specimens) in the galvanizing bath to quantify ε_R . The basis of the numerical procedure is work reported in the JRC report titled “Hot-dip-zinc coating of prefabricated structural steel components” (M. P. Feldmann, T.; Schafer, D.; Pope, R.; Smith, W.; Sedlacek, G., 2010).

When requirements of the DASSt-Richtlinie 022 are met based on meeting a series of conditions (Option 1), the following list summarizes some notable requirements that are placed on the structure and galvanizing process:

- Materials that are welded must meet minimum toughness requirements as described in EN 1993-1-10; the highest level specified is J0.
- Specification of the permitted level of cold-forming (ε_{pl}) is required

- Significant detailing and fabrication constraints, including:
 - Minimizing large thickness/stiffness transitions at welds
 - Specifying welding sequences
 - Prohibiting intermittent welds
 - Not exceeding the weld size needed to satisfy the design
 - Avoiding overlap in parts (avoiding explosive vaporization during dipping)
 - Avoiding excess length in fillet welds (avoiding the superposition of residual stresses from welding and thermal cutting at plate ends)
 - Ensuring a maximum surface hardness of 340 HV at cut edges
 - Consideration of strain limits deduced from inner permissible radii, r , according to the design standards
- Pickling time (diluted hydrochloric acid) should be as short as possible. Therefore, steel components with heavy mill scale should be blasted fit the dipping process. After pickling, the steel parts should be rinsed in a water bath before fluxing in an aqueous solution of chlorides. The salt content of the fluxing bath should be greater than 400g/litre. After fluxing, the part is to be dried in open air or in a drying oven.
- The temperature of the part at the time of dipping should be at least +68 F. This may require preheating.
- The galvanizing bath should not have more than the following amounts of tin, lead, and bismuth, based on weight:
 - Sn < 0.1%
 - Pb+10Bi < 1.5% in other words, < (1.5% Pb + 0.15% Bi)
 - Ni < 0.1%
 - Al < 0.1%
 - Sum of total additional elements (without Zn+Fe) < 0.1%
- The zinc alloy should be chemically tested monthly for compliance
- Dipping of the steel part should be rapid and with a steep angle to keep thermal stresses across the profile depth small
- The minimum dipping speed is 31.5 in/min (0.8m/min)
- The holding time in the zinc bath should be kept low (maximum holding time is specified as 27 minutes for materials greater than 1.2 in. thick; thinner materials are not subject to restriction)
- After galvanizing, all steel components should be visually inspected for cracks.

Summary of Existing Standards and Specifications

The summary of standards and specifications described in the above sections provides a succinct overview of the major governing documents currently in-place in the United States and in other countries that have closely considered the issue of cracking occurring due to the galvanizing process. Currently, the U.S. provisions are comparatively silent on the issue when compared to the specifications in place in Europe and Japan.

It is also notable that the approaches taken in Europe and in Japan fundamentally differ. The DAST-Richtlinie 022 adopted in Germany (DAST, 2009) takes an approach to mitigating cracking that is strongly-focused on detailing requirements and on controlling the galvanizing bath chemistry. The approach taken in Japan (JIS, 2005, 2007) strongly relies on controlling the steel chemistry.

State DOT Practices

State specifications were reviewed for all 50 states to gain an understanding for current practice regarding the design and fabrication of galvanized welded highway structures. Specification content relevant to the objective of the 10-94 project was categorized on the basis of materials selection, geometric detailing,

welding processes and preparation, and galvanizing processes. A summary of the findings from this portion of the literature review is presented here.

State DOT Practice: Materials Selection

The following list summarizes all material grades included in the State DOT specifications for various structure types. In general, ASTM A36 was the specified material for base plates. ASTM A53 Gr B, Type E or S; ASTM A595, Gr A; and A500 Gr B were the most common specifications for steel pipes and tubes for use in overhead sign structures and traffic structures. When specifications specifically discussed HMIP structures, material with a minimum $F_y=50$ ksi was commonplace (ASTM A572-50 and ASTM A595 Gr A being the commonly-specified grades). Highway bridge steel was specified to meet ASTM A709 (AASHTO M270) requirements, and it was not common to find preferences on material grade within the ASTM A709 specification specifically called out. However, experience has shown that ASTM A709 Gr 50, 50W, 70W, and HPS70W comprise the majority of newly-constructed steel bridge superstructures.

Overhead Sign Structures

Grades of steel listed in various DOT specifications: ASTM A595 Gr A (low carbon steel tubes); ASTM A53 Gr B, Type E or S (steel pipes); ASTM Gr A36 (shapes, plates, and bars); ASTM A618 (welded and seamless HSLA tubing); ASTM A595, Gr A; ASTM A500 Gr B (cold-formed welded and seamless structural tubing); ASTM A501 (hot-formed welded and seamless structural tubing); ASTM A106 Gr B (steel pipe); ASTM A139, Gr B (steel pipe); ASTM A847 (weathering steel tubing); ASTM A252 Gr 2 (steel pipe); ASTM A572-50; ASTM A572-55; ASTM A519-4140 annealed; ASTM A108; ASTM A992

Traffic structures (mast-arm signal structures)

Grades of steel listed in various DOT specifications: ASTM A53 Gr B, Type E or S (steel pipes); ASTM Gr A36 (shapes, plates, and bars); ASTM A618 (welded and seamless HSLA tubing); ASTM A1011, SS, Gr 50; ASTM A572-50; ASTM A595, Gr A; ASTM A500 Gr B (cold-formed welded and seamless structural tubing); ASTM A501 (hot-formed welded and seamless structural tubing); ASTM A106 Gr B (steel pipe); ASTM A139, Gr B (steel pipe); ASTM A847 (weathering steel tubing); ASTM A252 Gr 2 (steel pipe); ASTM A572-50; ASTM A607 Gr 310; ASTM A992

Luminaires, including High Mast Illumination Poles (HMIPs)

Grades of steel listed in various DOT specifications: ASTM A53 Gr B, Type E or S (steel pipes); ASTM Gr A36 (shapes, plates, and bars); ASTM A618 (welded and seamless HSLA tubing); ASTM A500 Gr B (cold-formed welded and seamless structural tubing); ASTM A501 (hot-formed welded and seamless structural tubing); ASTM A106 Gr B (steel pipe); ASTM A139, Gr B (steel pipe); ASTM A847 (weathering steel tubing); ASTM A252 Gr 2 (steel pipe); ASTM A572-50; ASTM A1011; ASTM A606; ASTM A656; ASTM A519-4140 annealed; ASTM A572-60; ASTM A108

Steel Bridge Superstructures

Grades of steel listed in various DOT specifications: ASTM A709 Gr 36, 50, 50W, 70W, HPS70W, 100, and 100W; ASTM A36; ASTM A572-50; HPS-70W; ASTM A709 Gr 100 or 100W; ASTM A514; ASTM A588;

Other items of interest regarding materials specifications for welded, steel highway structures in the DOT specifications:

- The Illinois DOT and Oregon DOT explicitly limit the silicon content of steel to be dipped to less than 0.04% or between 0.15-0.25%
- The New York DOT places a Carbon Equivalency (CE) requirement on all pipe used for welded applications: $CE = \%C + \%Mn/6 + \%Cu/40 + \%Ni/20 + \%Cr/10 - \%Mo/50 - \%V/10$

State DOT Practice: Geometric Detailing

In general, geometric detailing was found to not be very prescriptive in the various DOT specifications. Most specifications simply point the user to either the current edition of the AASHTO Sign Specification or to the 1994 edition of the AASHTO Sign Specification for geometric design. However, the following list notes some commonalities, and some notable individual provisions.

- Many DOTs specify a range of minimum cold-bending radii, usually depending upon the thickness, t , of the plate material. A range that is commonly included in the specifications is $2t - 4t$ ($2t$ for thinner material, and $4t$ for thicker material).
- Alaska DOT, Kentucky DOT use a range of $1t - 2t$, dependent upon the plate thickness
- Many DOTs specify minimum base plate thicknesses. These are often on the order of 2 in. – 2.5 in. thick.
- The Alaska DOT uses a range of 2.5 – 3 in.
- A common geometric configuration for poles, posts, and mast-arms is to use continuously tapered steel tubes that include a single longitudinal weld seam.
- Most DOTs allow either round or multisided poles for use as tapered HMIP structures; however, many DOTs show round poles on standard drawings.
- The Maine DOT specifies a minimum number of sides on a polygonal pole to be 12

State DOT Practice: Welding Processes and Preparation

As should be expected, State DOTs consistently referred to AWS D1.1 for overhead sign structures, traffic structures, and luminaires (or noted that AWS D1.1 should be the governing specification where tubular structures are welded) and AWS D1.5 was referred to as governing the welding of steel superstructures. The following list notes commonalities between the state DOT specifications applicable to the 10-94 project, and also notes some individual provisions.

- Many state DOTs prohibit circumferential butt welds for round cross-sections (no butt-welded splices); those that allow them require these welds to be CJP groove welds.
- Many state DOTs explicitly prohibit electroslag welding for steel bridges.
- Longitudinal seam welds are specified to be continuous; most DOTs require there to be no more than one longitudinal weld. Those that allow two require that the seams be on opposite sides of the cross-section.
- Alabama DOT requires submerged arc welding for all shop-welding. Delaware DOT prohibits gas metal arc welding (GMAW).
- Welds to base plates are generally specified to be 100% full-penetration welds or a socket-type connection with a weld provided at top and bottom of the base plate, circumferentially around the pole
- The Mississippi DOT requires that all welds be mechanically cleaned before galvanizing

State DOT Practice: Galvanizing

DOT specifications consistently pointed to the ASTM A123 (AASHTO M111) specification as governing the galvanizing process to be used for overhead sign structures, traffic structures, and luminaires. Galvanizing steel bridge superstructures was not specifically discussed in any of the DOT specifications, but also was not excluded. Overall, provisions in the state DOT specifications were quite limited with respect to galvanizing requirements, and most DOTs had few or no additional specifications beyond what

is included in ASTM A123. Notably, only one DOT specification references the ASTM A143 standard (Nevada DOT), by stating “Take precautions against embrittlement, warpage, and distortion in accordance with ASTM A143 and ASTM A384”.

- Some DOTs specified that closed hollow sections must have vent holes at each end of the member.
- Many DOTs specified that galvanization of the structural members should occur after all fabrication processes (welding, drilling, punching, cutting, etc.) have been completed.
- The Alaska DOT requires that each component be galvanized in one dip only. Additionally, they only allow the dry kettle method of fluxing for high tower poles (concentrated zinc ammonium chloride flux solution heated to 130 °F). Finally, the Alaska DOT also specifies that Prime Western (PW) zinc heated to approximately 825 F be used as the galvanizing bath.
- The Georgia DOT requires that “All components galvanized in accordance with ASTM A123 shall be quenched immediately upon removal from the zinc bath.”
- The Maine DOT requires that steel should be cleaned prior to galvanizing in accordance with SSPC-SP 6. They also prohibit chromate quenching and all other types of quenching after galvanizing.
- Some state DOTs require that exposed welds (other than fillet welds) be ground flush with the base metal before galvanizing.
- The South Carolina DOT states that “Galvanizing component parts during fabrication is permitted if the weld and cut areas are shop-treated by an approved field galvanizing process.”
- Texas has a substantial component to its specification focused on galvanizing. It states that “If problems develop during galvanizing of welded material, the Engineer may require a compatibility test of the combined galvanizing and welding procedures... and may require modification of one or both of the galvanizing and welding procedures.” The Texas DOT requires draining of the galvanizing bath to the small end of the tapered sections that are assembled using slip-joint splices. The Texas Specifications also state that “Ensure cleaning and galvanization does not produce hydrogen embrittlement.”
- The Virginia DOT Specifications note that “Galvanizing surfaces that have been damaged or have uncoated areas shall be repaired in accordance with ASTM A780, except that repair materials shall not contain lead or cadmium.”

Current Galvanizing Practice – Bath Chemistry

The American Galvanizer’s Association (AGA) provided the research team with results from a survey that was administered to 49 galvanizing plants in 2007. The results provided information regarding the galvanizing bath composition used at those plants, as well as the type of zinc used at the plants.

Figure A-1 presents the distribution of type of galvanizing used in the US plants in 2003 and 2007. As shown in the graph, in 2007, approximately 20% of galvanizing plants were using Prime Western grade zinc, 15% using High Grade, 19% using Special High Grade, and 6% were using a combination. It is notable that between 2003 and 2007, a significant decrease in usage of Prime Western grade zinc was noted, while a corresponding increase in usage of Special High Grade zinc occurred.

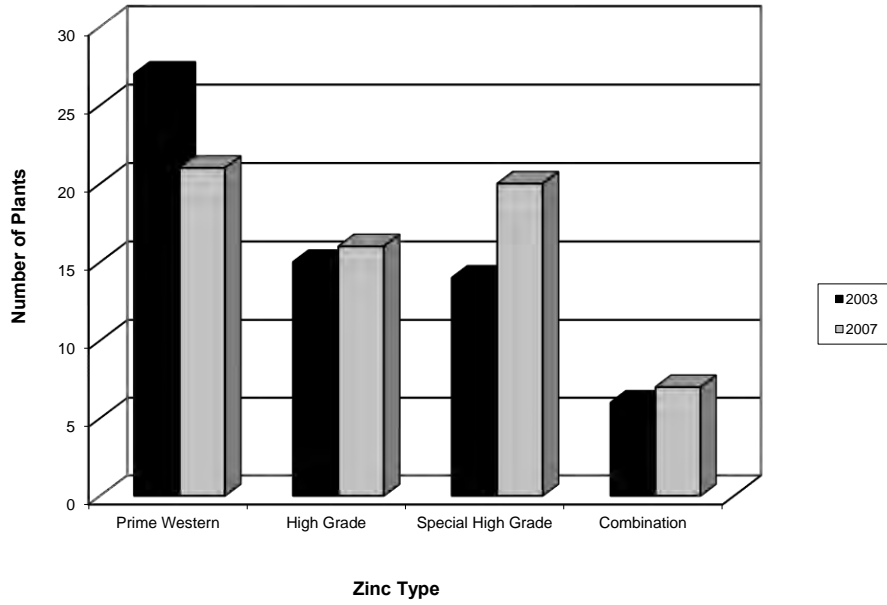


Figure A-1: Distribution of galvanizing zinc-type used in US galvanizing plants in 2007 and 2003, from (AGA, 2007)

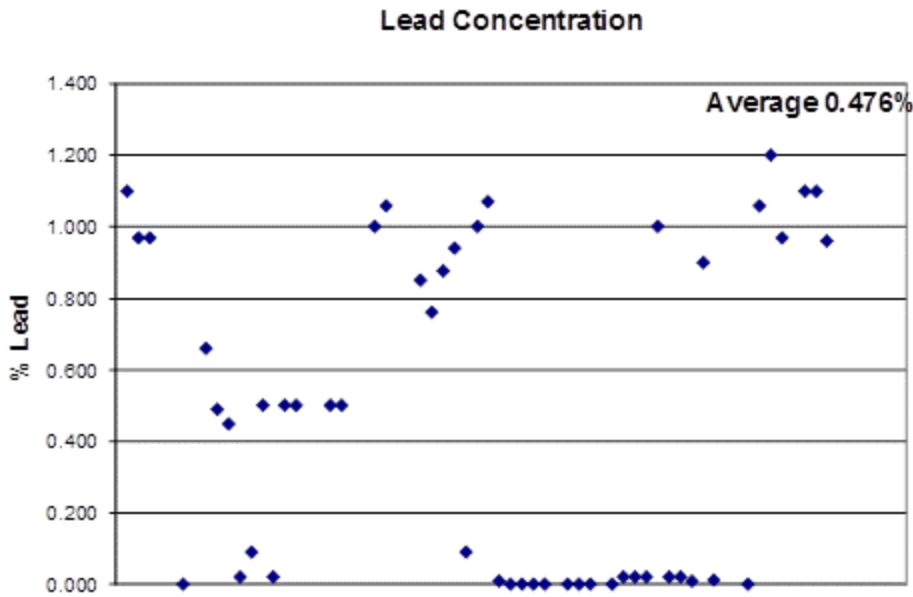


Figure A-2: Distribution of lead (Pb) concentration used in US galvanizing plants in 2007, from (AGA, 2007)

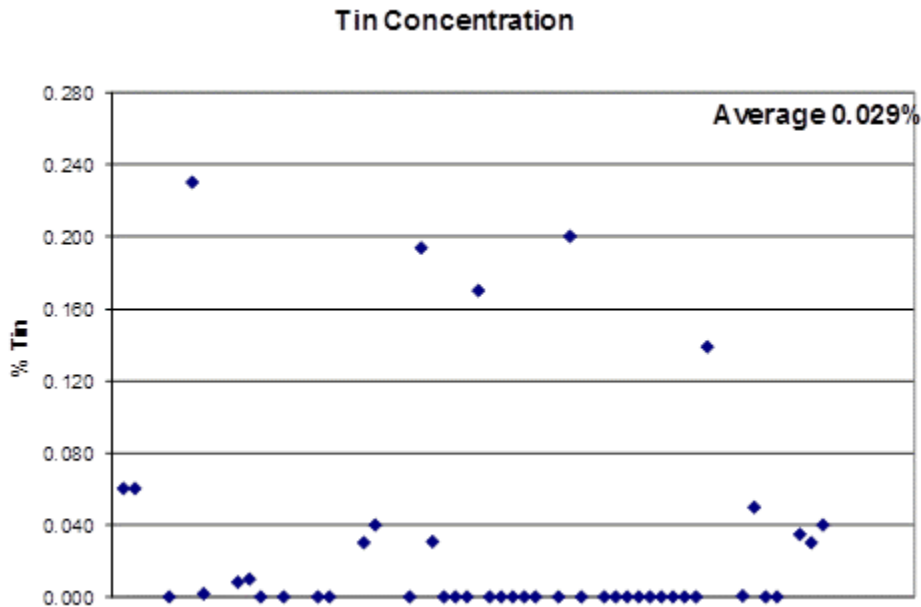


Figure A-3: Distribution of tin (Sn) concentration used in US galvanizing plants in 2007, from (AGA, 2007)

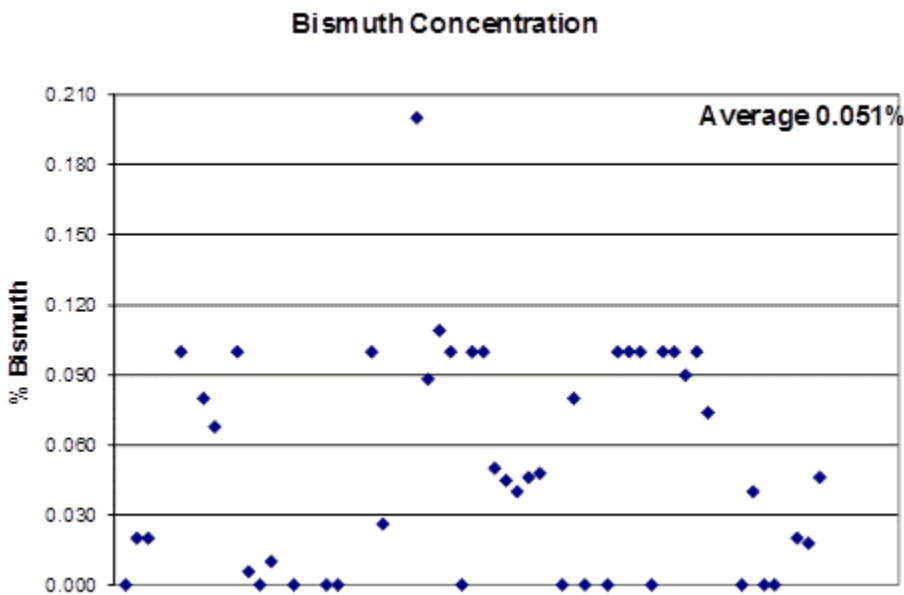


Figure A-4: Distribution of bismuth (Bi) concentration used in US galvanizing plants in 2007, from (AGA, 2007)

Figure A-2, Figure A-3, and Figure A-4 present the levels of lead (Pb), tin (Sn), and Bismuth (Bi) used in the galvanizing baths at the 49 plants responding to the survey. The survey results indicate that use of lead and bismuth in galvanizing baths is quite common, while use of tin is less common. The most

commonly used concentration for lead was 1%, and the most commonly used concentration for bismuth was 0.1%. These findings support the use of the latter concentrations (1% Pb and 0.1% Bi) in the research plan.

Additionally, the survey results showed that approximately 20% of the galvanizers reporting data were using a combination of Pb and Bi with relative combinations of Zn + 1% Pb + 0.1% Bi. Another 40% of respondents indicated that they were using Zn + Bi + Pb, but in various other combinations. The 1% Pb + 0.1% Bi was the most frequent combination of Pb and Bi concentrations reported. (AGA, 2007)

Case Studies – Experience with Cracking during the Galvanizing Process

Case Study: Valmont Industries Experience

Representatives from the 10-94 research team visited Valmont Industries in Valley, NE in August 2014. During that visit, representatives from Valmont made a formal presentation (Higgins, 2014) to the research team regarding their fabrication and galvanizing practices, as well as their experiences with cracking in welded, highway structures occurring due to the galvanizing process.

Materials that are commonly-used by Valmont include leveled coil steel (A36 and A572-50/55/65 compliant) and Gr. A572-50/55/65, A633-E, and A588 plate steel. To process the steel into different sizes, a rotary shear (600-1200 fpm) is used for edge trimming and coil dividing. Thermal cutting is often used for plate that is 3/16 in. – 6 in. thick; the speed used varies from 10-220 inches/minute.

To create tapered poles, various forming processes are used to create round or polygonal shapes. For tapered poles with a base diameter less than 13 in. and thicknesses less than 1/4 in., the sections are formed around a mandrel and seam-welded using electric resistance welding (ERW). The poles are sometimes (normally) burnished (cold-worked) to improve the material and dimensional properties. Poles having base diameters greater than 13 in. are seamed using submerged arc welding (SAW) and / or the hybrid laser arc welding (HLAW) process. Various process are used for welding poles to base plates, including SAW (pole diameters > 13 in.), flux metal core process (FCAW) (pole diameters < 13 in.), and gas metal arc welding (GMAW) (pole diameters < 13 in.).

Valmont, like many pole manufacturers, has experienced problems with cracking at weldments that occurs during the galvanizing process. The majority of the defects experienced have occurred at the connection between the pole shaft and base plate at the toe of a fillet weld, as shown in Figure A-5. In cases where the pole was polygonal, cracks tended to occur near the corners. In general, cracking was more commonly noted in polygonal poles than in round poles.

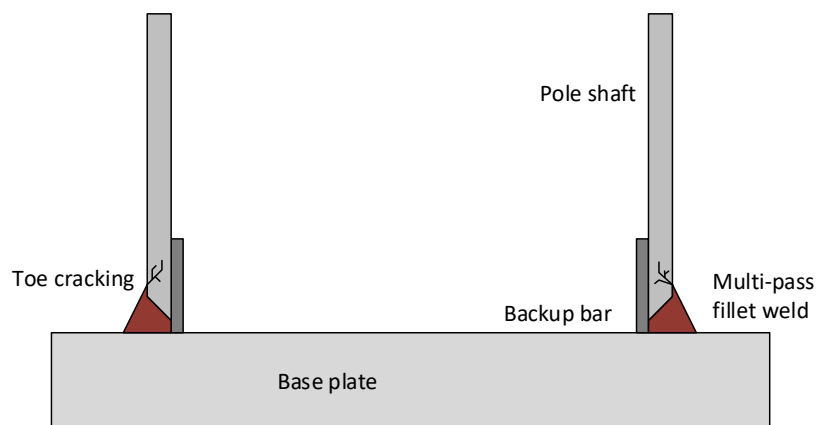


Figure A-5: Typical pole-to-base plate cracking

In 2001, Valmont plants detected failures (cracking found during weld inspections and requiring repair) at rates between 19% and 58%. (It should be noted that the 58% figure was based only one month of recorded data.) In 2002, they saw failure rates between 1% and 32%, and in 2003, they experienced failure rates between 0% and 37%. Notably, a large percentage of the failures recorded in 2002 and 2003 occurred in poles fabricated using ASTM A572-65 steel.

The decrease in failure rates that Valmont noted between 2001 and 2003 represents a significant improvement in reducing defects, and it begs the question, “what changed?” Over that time, a number of changes were implemented in fabrication procedures and material selections that seemed to correlate with improved performance:

- Welding heat input was reduced, while remaining within approved welding procedures.
- The pre-heat temperature for welding procedures was increased.
- The material specification was changed so that when A572-65 is required, A572-65 Type I or V is specified, to reduce the CEZ value for the steel.
- They considered the reported chemical composition of steel in relation to the Japanese CEZ formulae, and found that over the time period of 1999-2002, the CEZ value of steel being processed had increased from an average value of approximately 0.25 to above 0.4. It should be noted that the Japanese specifications limit the CEZ to a value of 0.44.
- The minimum cold-bend radius was changed from 2 in. to 4 in. for polygonal shapes formed using a brake press.

The Valmont experience is an important one, as they are the largest producer of galvanized highway structures in the United States. The fact that they have been able to greatly reduce in-shop cracking incidences by modifying fabrication procedures and materials selection is important, in that it shows that specifications can be written to control fabrication processes and materials selections without being unduly burdensome to the industry.

Case Study: American Institute of Steel Construction (AISC) Experience

Over the last few years, the American Institute of Steel Construction (AISC) has collected specimens from steel structures that have cracked during the galvanizing process. While analysis of the specimens was not performed under the 10-94 research program, AISC permitted the research findings to-date to be presented to the 10-94 team in December, 2014. Multiple sections were studied, including the webs of W8x40s that developed cracks in “k” area of the web.

A metallographic examination was performed in which the fracture surfaces were examined to assess the grain structure and to examine the chemical composition along the crack length. Two impactful findings were made.

(1) All cracking was found to be intergranular, as shown in Figure A-6, captured using a scanning electron microscope (SEM). The presence of intergranular cracking supports the occurrence of LMAC in these specimens.

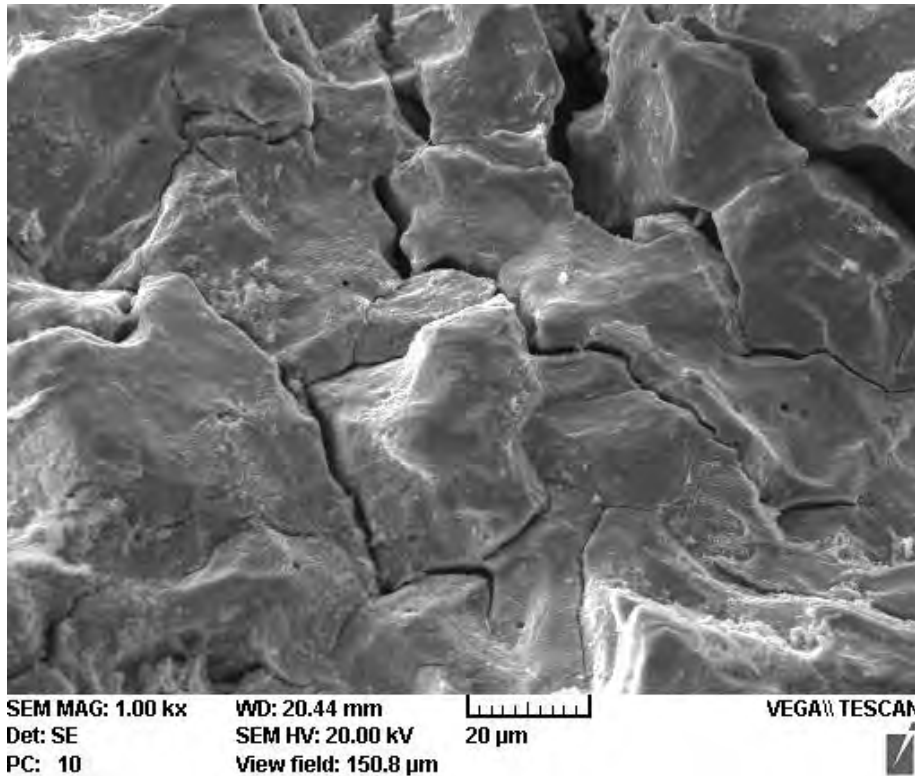


Figure A-6: Intergranular cracking in AISC specimen

(2) When the chemical composition of the crack surfaces was examined using a mass spectrometer, the relative percentage of galvanizing bath elements was found to not be uniformly distributed. One crack analyzed is shown in Figure A-7; the image shows the crack geometry, and also the locations at which readings were taken. Results for two reading locations are shown in Figure A-8 and Figure A-9. Reading location no. 1 is shown in Figure A-8; this location is somewhat removed from the crack tips. The mass spectrometer readings indicate that the composition of the material at this point along the crack is almost entirely zinc (Zn) and iron (Fe), indicating the presence of the zinc bath in the crack opening, as well as the formation of intermetallics (Zn + Fe) as would be expected. However, the reading no. 4 taken approximately 150 μ m away from reading no. 1 indicated a very different composition of elements within the crack. Reading no. 4 is much closer to the crack tip, and the elements within the crack opening include zinc (Zn), bismuth (Bi), tin (Sn), and iron (Fe). In fact, the concentration of Bi is actually greater than the concentration of Zn at this location, indicating a high concentration of this “heavy” element at the crack tip. This phenomenon has been noted in other investigations, and is a common thread in many LMAC failures (Kinstler, 2005).

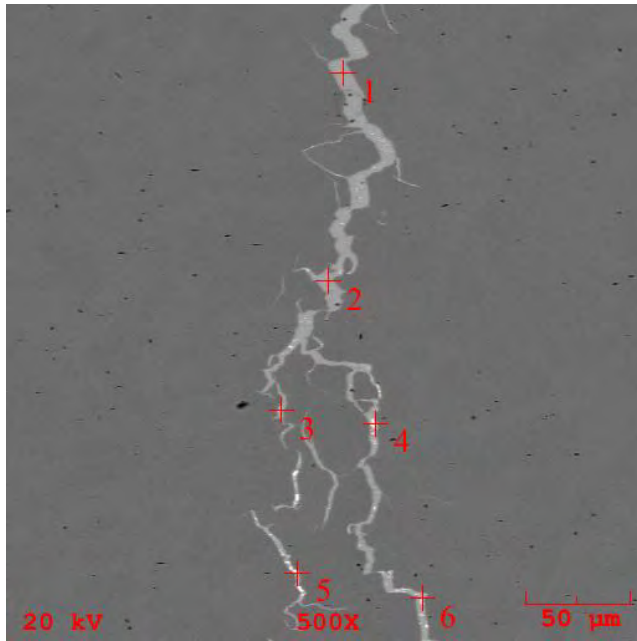


Figure A-7: Crack analyzed using mass spectrometry; locations where composition readings were taken are shown by the red numbers

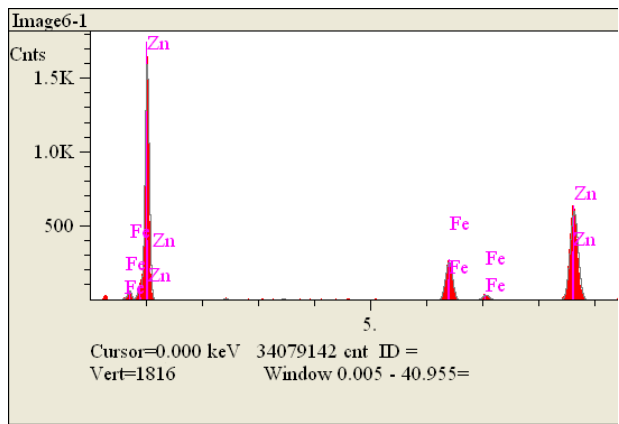


Figure A-8: Mass spectrometry results for location 1 (with reference to Figure A-7)

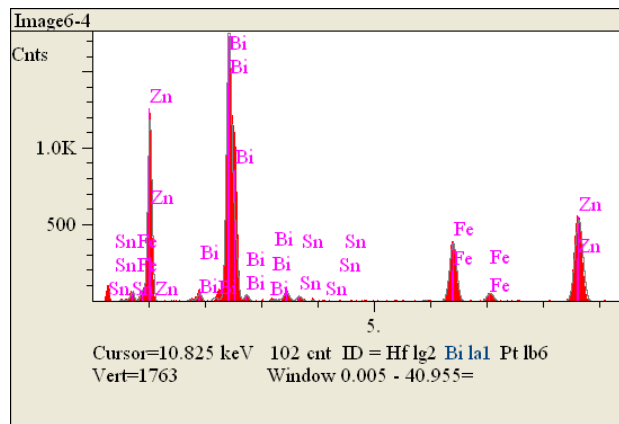


Figure A-9: Mass spectrometry results for location 4 (with reference to Figure A-7)

APPENDIX B

Literature Review

This Appendix presents a literature review of factors that have been shown to be related to cracking during galvanizing. The following topics are explored:

- Steel chemistry
- Galvanizing bath chemistry
- Residual stresses
- Cold-working
- Geometry
- Thermal stresses
- Hardness
- Welding process and effects
- Hydrogen embrittlement
- Strain age embrittlement
- Effect of galvanizing on fatigue strength of steel structures

Steel Chemistry

Effect of steel chemistry on susceptibility of steel to LMAC

Prior to the 1970s, most of the power transmission towers in Japan were manufactured using grade 400 N/mm² (58 ksi) steel. The need for larger and lighter towers by the power industry in Japan motivated the development of higher strength steels (Grades 490 and 540 in N/mm²; 71 and 78 ksi). Grade 540 steel (STK 55) was developed to have a low carbon equivalent (CE < 0.40%) to improve the weldability. One of the main concerns leading up to the development of these higher strength steels was the effect of alloy elements often added to increase the strength of the steel on LMAC during galvanizing. In order to prevent this problem, an experimental program was developed to study the effect of the chemical composition of the steel on susceptibility to LMAC, also referred to in the report as zinc-assisted cracking. In the study by the Tomoe Corporation (2001), susceptibility to liquid metal embrittlement was defined as the ratio of fracture stress in liquid zinc to that in air, both measured using notched tensile coupons (as in Figure B-1) tested at a temperature ranging between 450 and 470 °C.

$$S_{LM} = \frac{\text{notched fracture stress in liquid zinc}}{\text{notched fracture stress without zinc}} \times 100 \quad \text{Equation B-1}$$

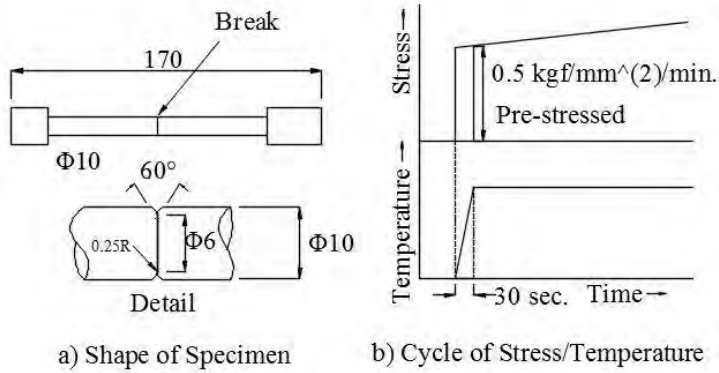


Figure B-1: Round metal bar tension test, adapted from (Tomoe Corporation, 2001).

Experimental measurements in liquid zinc were made after 400 seconds of immersion (S_{LM-400}). The threshold of 400 seconds was chosen because the value of SLM was found to be sensitive to immersion time, with a tendency for the measurements to stabilize after an immersion time of 400 seconds. The sensitivity of SLM-400 of different steels (A, B, C, D, E, F, H, J, and K) to immersion time is shown in Figure B-2.

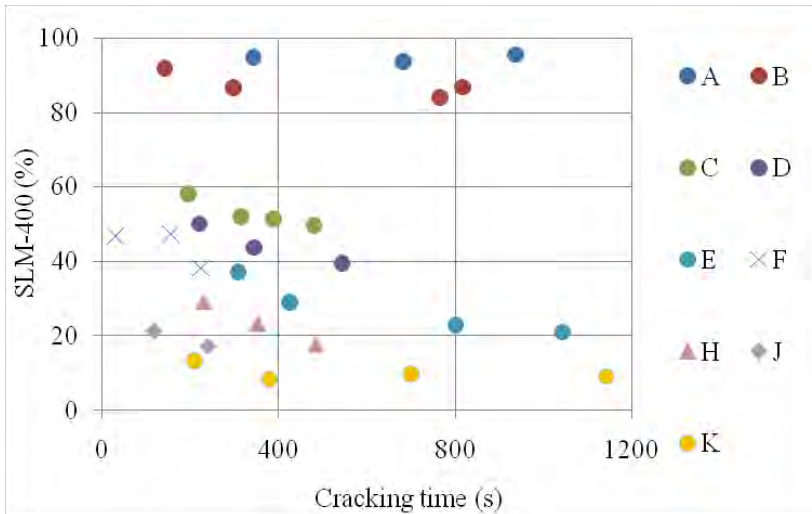


Figure B-2: Sensitivity of SLM-400 to immersion time, adapted from (Tomoe Corporation, 2001).

Companion tests were performed by steel fabricators by immersing unloaded cross-constrained joint test specimens in a zinc bath, as shown in Figure B-3. The specimens consisted of steel plates welded together in a cruciform shape, with a one-pass test bead laid on opposite corners of the joint and 20-pass constrained beads laid in the other two corners of the joint.

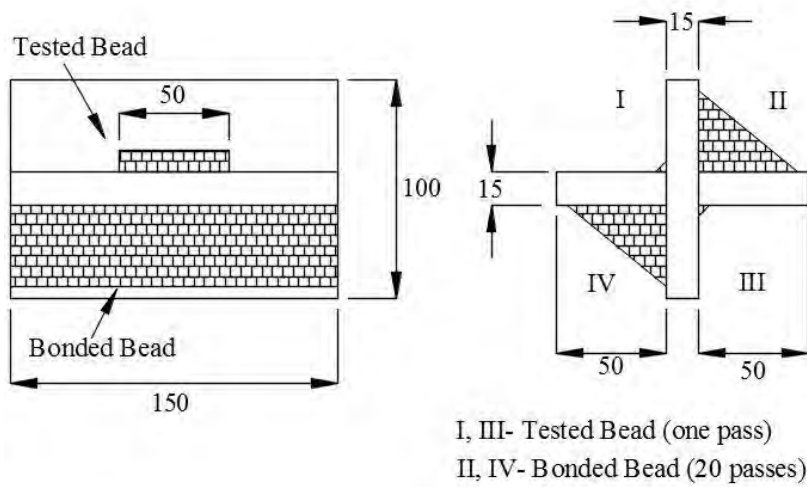


Figure B-3: Cross-constrained joint test specimen, adapted from (Tomoe Corporation, 2001).

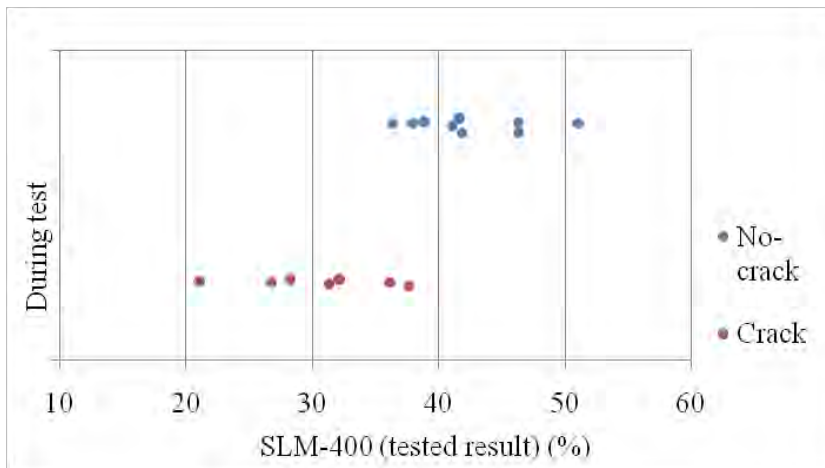


Figure B-4: Occurrence of cracks vs. SLM-400, adapted from (Tomoe Corporation, 2001).

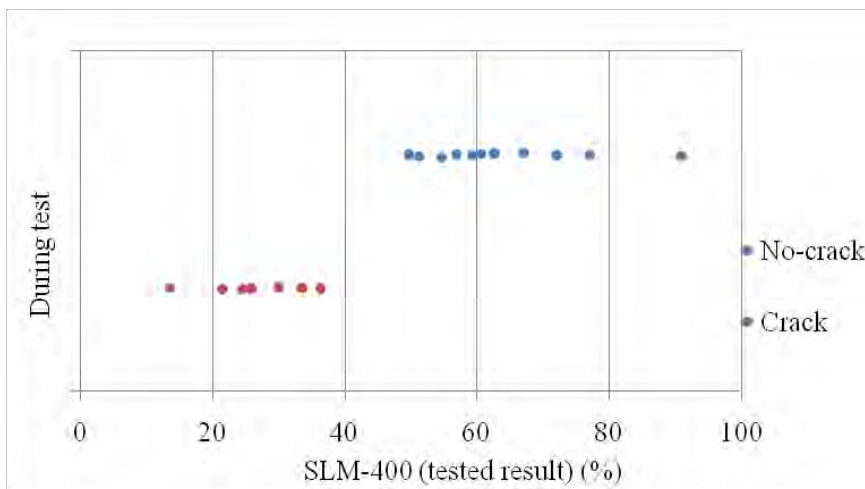


Figure B-5: Occurrence of cracks vs. SLM-400, adapted from (Tomoe Corporation, 2001).

The test piece was immersed in a molten zinc bath for 10 minutes, allowed to cool, and inspected for cracks using magnetic particle examination. Immersion tests were also performed using fillet welded sections of steel pipe towers, where the thermal stresses were significantly higher. Fabricators found by performing repeated tests of specimens in which the SLM-400 was relatively low that a minimum value of 42% was needed to prevent the occurrence of cracks during galvanizing. As seen in Figure B-4 and Figure B-5, cracks occurred when the SLM-400 value was larger than approximately 42%.

The study by Tomoe Corporation (2001) analyzed the performance of two hundred different steel samples of HT60 steel. The chemical composition of the samples was analyzed and found to have the following ranges of alloy elements, as shown in Table B-1.

Table B-1: Chemical composition of samples, adapted from (Tomoe Corporation, 2001).

Element Name	Symbol	Percent Wt.
Carbon	C	0.04 to 0.12
Silicon	Si	0.40 max
Manganese	Mn	1.20 to 1.80
Phosphorus	P	0.04 max
Sulfur	S	0.04 max
Copper	Cu	0.50 max
Nickel	Ni	0.80 max
Chromium	Cr	0.30 max
Molybdenum	Mo	0.30 max
Vanadium	V	0.09 max
Niobium	Nb	0.09 max
Titanium	Ti	0.03 max
Aluminum	Al	0.015 to 0.070
Nitrogen	N	0.0025 to 0.0080
Boron	B	0.0010 max

A correlation was established between the S_{LM-400} and the chemical composition of the steel as shown in Equation B-2:

$$S_{LM-400} = 424 - 667 C - 25 Si + (95 Mn^2 - 342 Mn) + 354 S - 230 \\ - 273 Nb - 130 Ti + (180 Cr^2 - 198 Cr) - 72 Mo - 6000 B \quad \text{Equation B-2}$$

For specimens in which $S_{LM-400} > 42\%$ a correlation was made to introduce the concept of the Carbon Equivalent Zinc (CEZ) which is as shown in Equation B-3 (adopted as a JIS standards G 3474-1988 for steel pipes and G 3129-1988 for steel plates):

$$CEZ = C + \frac{Si}{27} + \frac{Mn}{12} + \frac{V}{3} + \frac{Nb}{2.5} + \frac{Ti}{5} + \frac{Cr}{6} + \frac{Mo}{9} + 9B \\ \leq 0.28\% \quad \text{Equation B-3}$$

As shown in Equation B-3, the JIS standard requires an upper limit of 0.28% for the CEZ.

Among the first structures manufactured following this JIS standard was the Ultra High Voltage North-South Line. During fabrication of the steel towers, cracks were found at fillet welds in thin-wall steel pipes after they were galvanized. The investigation of those failures focused on thermal distortion and the chemical composition of the steel, due to the fact that traces of boron were found in the steel. A companion

study on bridge structures also showed a qualitative decrease in S_{LM-400} with increasing boron content, so a more detailed study was conducted to evaluate the effect of the amount of boron in the steel on LMAC. The follow-up study was performed using specimens from two different types of pipe and various contents of carbon, manganese and boron. The boron content was varied between 1 ppm and 5 ppm. Test results, in Figure B-6, showed that regardless of the content of manganese and carbon, the S_{LM-400} decreased linearly with the boron content up to 4 ppm, and that there were significant reductions in S_{LM-400} when the boron content was 4ppm. (UO: pipe 20 mm thick, ERW: pipe 12 mm thick).

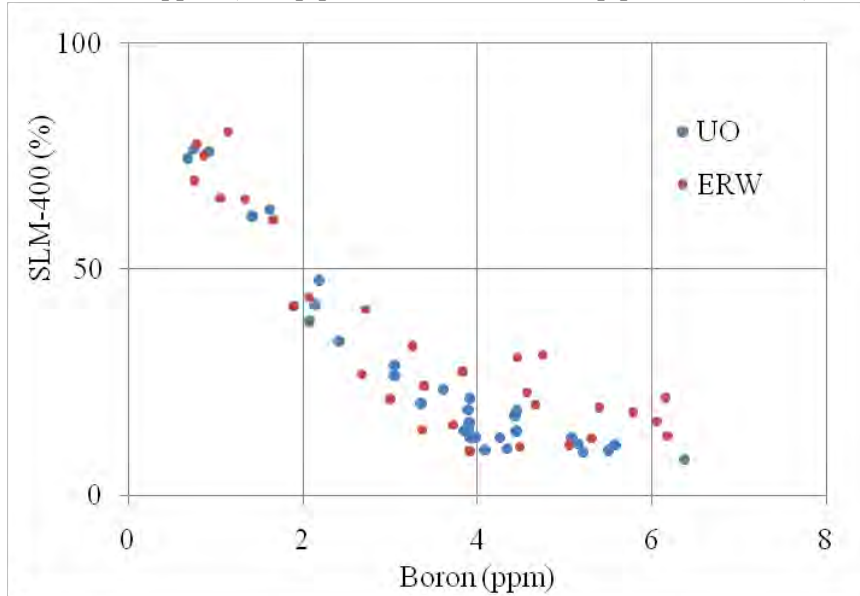


Figure B-6: Effect of Boron on SLM-400, adapted from (Tomoe Corporation, 2001).

Because the test results showed that steels with high boron content were particularly susceptible to cracking, it was decided to limit the boron content to a maximum of 2 ppm, which corresponded to an S_{LM-400} value of approximately 42%. A new linear regression was performed based solely on steel samples with boron content of 2 ppm or less, and the expressions for S_{LM-400} and CEZ were adjusted to that shown in Equation B-4 and Equation B-5 (adopted as a JIS standards G 3474-1995 for steel pipes and G 3129-1995 for steel plates):

$$S_{LM-400} = 201 - 370C - 22 Si - 51Mn - 35P + 33 S - 28 Cu - 22Ni - 87Cr - 275 V - 182 Nb - 82 Ti - 123 Mo - 24Al + 1700N - 155000B \quad \text{Equation B-4}$$

$$CEZ = C + \frac{Si}{17} + \frac{Mn}{7.5} + \frac{Cu}{13} + \frac{Ni}{17} + \frac{V}{1.5} + \frac{Nb}{2} + \frac{Ti}{4.5} + \frac{Cr}{4.5} + \frac{Mo}{3} + 420B \leq 0.44\% \quad \text{Equation B-5}$$

The new JIS standards were adopted with the requirement that the boron content be 2 ppm or less.

A follow-up study was performed using STKT590 steels to investigate the effect of steel chemistry on strain at crack occurrence in liquid zinc, ϵ_{ZC} . Experimental results showed that the strain at crack occurrence in liquid zinc, ϵ_{ZC} , was inversely proportional to the boron content in ppm, as shown in Figure B-7. This trend was similar to that observed for the relationship between S_{LM-400} and boron content, and confirms the finding that S_{LM-400} increases proportionally with ϵ_{ZC} .

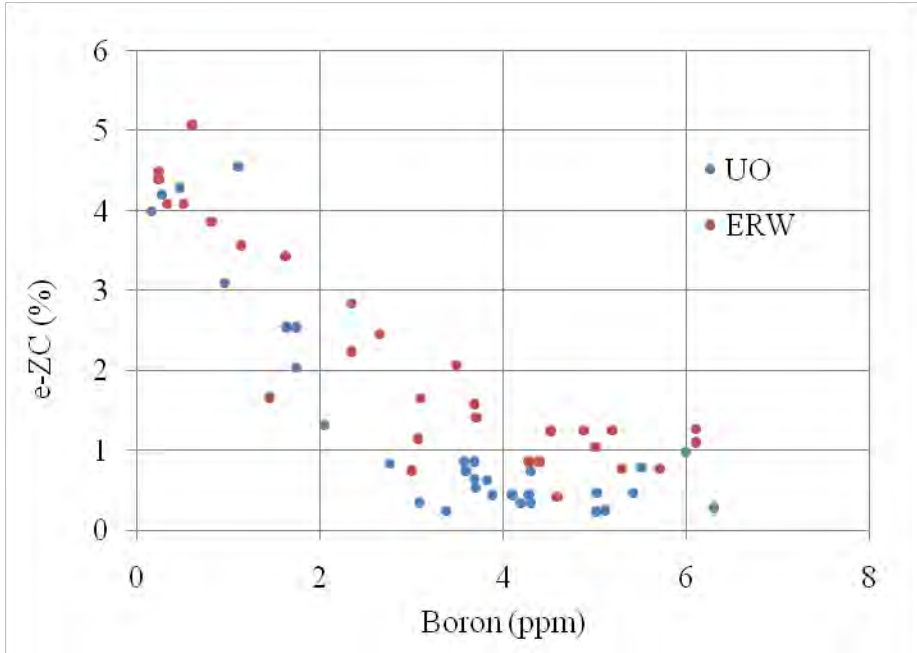


Figure B-7: Effect of boron on strain at crack occurrence, ϵ_{ZC} , adapted from (Tomoe Corporation, 2001).

For specimens in which the boron content was not limited to 2 ppm, the relationship between ϵ_{ZC} and CEZ had a high degree of scatter and there was no discernable trend, as shown in Figure B-8.

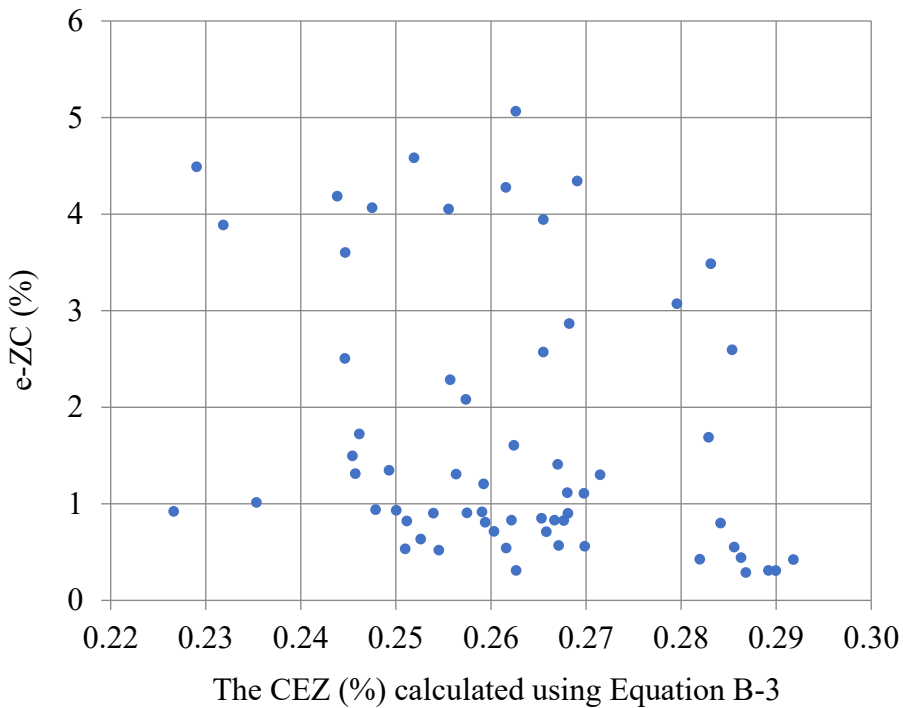


Figure B-8: The relationship between ϵ_{ZC} and CEZ, when boron content was not limited to 2 ppm, adapted from (Tomoe Corporation, 2001).

When the boron content was limited to 2 ppm, the relationship between ϵ_{ZC} and CEZ became much better defined, with the ϵ_{ZC} decreasing with increases in CEZ . The data in Figure B-9 shows that for a CEZ of 0.38% the strain at crack occurrence in liquid zinc, ϵ_{ZC} , typically exceeded 4%.

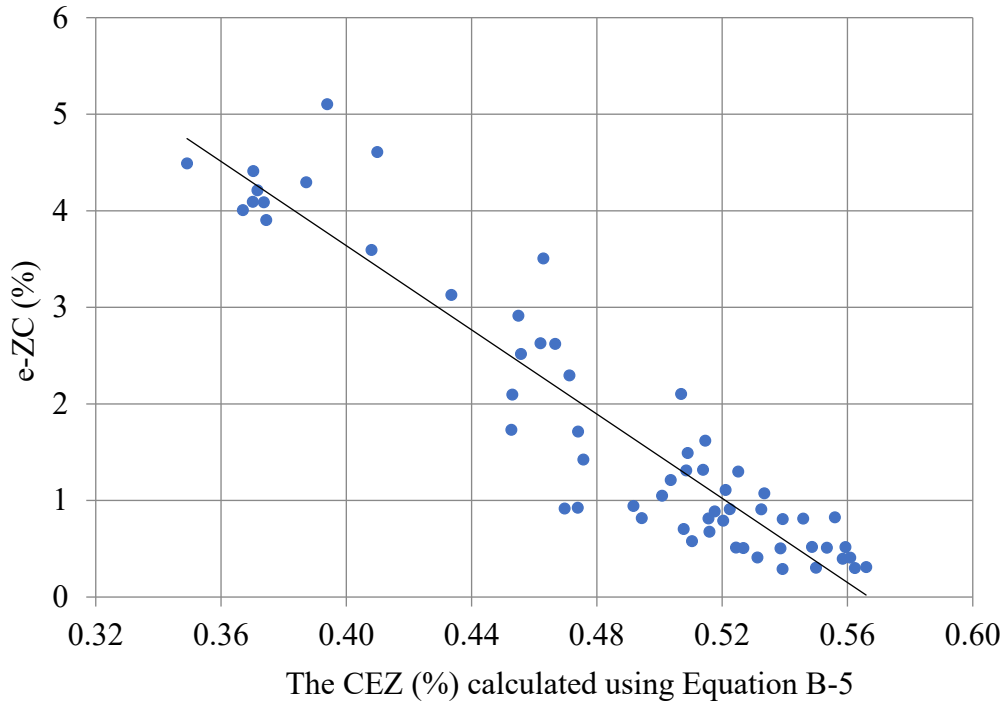


Figure B-9: The relationship between ϵ_{ZC} and CEZ , when Boron content was limited to 2 ppm, adapted from (Tomoe Corporation, 2001).

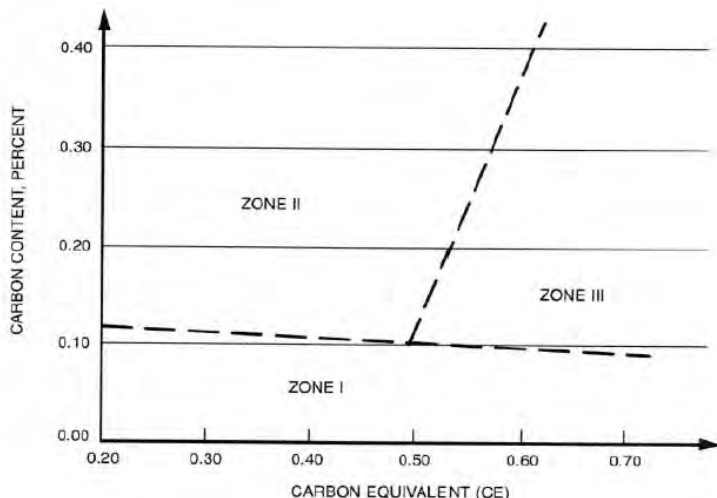
Zone classification of steels

In welding practice, weldability and hardenability are two characteristics closely related to cold cracking of welded steel structures. Weldability is the ease of welding a material, while hardenability is inversely proportional. The content of carbon plays an important role in determining steel hardenability which is the sensitivity of steel to form brittle microstructures due to weld thermal cycles. Based on a number of hardening curves of (Graville, 1975), three zones of steel was identified (as in Figure B-10) according to carbon content and carbon equivalent (Goyal, 2012):

Zone I – These types of steel have low carbon and will not produce hard HAZs susceptible to cracking under normal circumstances.

Zone II – Steel types with these compositions show steep hardening curves and the possibility of hardness control exists.

Zone III – Hardness control is not possible and welding procedures must be designed on other principles.



[CE = C + (Mn+Si)/6 + (Cr + Mo + V)/5 + (Ni + Cu)/15, where C = % Carbon, Mn = % Manganese, Si = % Silicon, Cr = % Chromium, Mo = % Molybdenum, V = % Vanadium, Ni = % Nickel and Cu = % Copper]

Figure B-10: Zone Classification of Steels (AWS, 2010), (Goyal, 2012).

Galvanizing Bath Chemistry

A typical galvanizing bath contains approximately 98% of molten zinc, and can contain other additives with different compositions. The reason for using additives has been indicated in Dugan (1999), which presented an overview on the function of minor elements (iron, aluminum, lead, bismuth, nickel, tin, copper, and cadmium). Addition of these elements can improve the appearance and structure of the galvanizing coating, and can help to control the thickness of the coating. However, some of these elements have been seen as contributors to cracking that can occur during galvanizing.

Table B-2: Experimental Galvanizing Bath Compositions, adapted from (Poag and Zervoudis, 2003).

Alloys	Purpose
SHG	Baseline
PW	Baseline (and effect of Pb)
PW + 0.05Ni	Effect of Ni
PW + Bi (from 0.1 to 0.5)	Effect of Bi (3 Bi levels)
PW + 0.1Bi + Sn (from 0.1 to 1.0%)	Effect of Sn (6 Sn levels with Bi)
PW + 0.5Sn + 0.1Bi + 0.05Ni	Effect of stress relieving, preheating, bath temperature, immersion rate, flux chemistry and surface grinding.

Note: All baths also contained 0.003 to 0.006% Al

Poag and Zervoudis (2003) conducted experiments using 31 galvanizing baths having different compositions to examine the effect of Pb, Ni, Bi, and Sn, as shown in Table B-2. The test specimens were Hollow Structural Steel (HSS) with corner radii that failed to meet ASTM (2007) requirements; the materials used were ASTM A500 and CSA G40-21-50W with the same minimum yield strength of 50 ksi. The results showed significant differences in crack probability between bath compositions. Lead was found to increase both the incidence and severity of cracking, while nickel was found to be helpful in reducing

cracking in Prime Western (PW) zinc baths. Tin and bismuth were harmful when they exceeded a certain amount, described to be 0.2% in this study.

Carpio, et al. (2009) tested the effect of liquid metal Zn baths (one bath with Zn-Pb, the other bath with Zn-Pb-Sn-Bi) on toughness of loaded compact tension (CT) specimens during immersion. The study clearly showed that the presence all liquid metals studied had a strong negative influence on embrittlement. They presented Crack Opening Displacement (COD) data for steels in the as-received condition, at 450°C in air and at 450°C in Zn-Pb-Sn-Bi liquid metal bath. They also compared the traditional Zn-Pb bath and the commonly-used Zn-Pb-Sn-Bi baths in terms of COD values during immersion in the galvanizing baths. The study showed that the Zn-Pb-Sn-Bi baths were more embrittling than the traditional Zn-Pb baths.

In another research study, Carpio, et al. (2010) tested 16 10-mm thick compact tension (CT) specimens which were made of EN 10025:4 S460M steel. They were immersed horizontally in a galvanizing bath in a crucible furnace. The chemical analysis at crack tip, presented in Table B-3, showed concentrated levels of Fe and Sn. To explain this phenomenon, consideration of the physical characteristics is needed. The melting points of Sn and Zn are 232°C and 420°C, respectively. However, the combination of Sn and Zn forms a eutectic with low melting point of 198°C. This liquid state permits Sn to penetrate and concentrate easily in some critical areas such as notches, defects, pre-existing cracks and even grain boundaries. If there is no external stress which is large enough to release it, liquid Sn will remain there, produce the brittle compound FeSn, and may create secondary cracks. This phenomenon explains why there is a high concentration of Sn at the crack tips.

Table B-3: EDS microanalysis of the crack tip, adapted from (Carpio, et al., 2009).

Element	% Weight	% Atomic
Cl	0.14	0.34
Fe	32.97	50.71
Zn	1.09	1.43
Sn	65.47	47.38
Pb	0.33	0.14

Rudd et al. (2008) performed an investigation at Aachen University in Germany, considering the effect of zinc alloys on LMAC. Three different galvanizing baths were used to investigate the effects of zinc alloys, referred to as a0, a1, and a2. Table B-4 shows the bath compositions, which included variations in lead, tin, bismuth, and nickel content. The type of test specimen used was a long notch tension, L-N(T), which is an adaptation of a compact tension (CT) specimen, with a longer notch. A drilled hole at the end of the notch tip (a keyhole notch) was made to establish a local stress concentration.

Table B-4: Zinc alloys used for testing at RWTH Aachen University, adapted from (Rudd et al., 2008).

Alloy	Pb	Sn	Bi	Al	Ni	Fe
a0	--	1.2	0.10	0.005	0.05	0.03
a1	0.7	--	--	0.005	--	0.03
a2	1	1	0.05	0.005	0.05	0.03

A universal testing machine was used to load the L-N(T) specimen while the majority of the specimen was submerged in a galvanizing bath housed in an electric furnace. Data was reported in terms of load-displacement curves, which showed early failure of the specimens in the zinc environment, as compared to in 450°C air. Effects were found to be more severe when galvanizing bath compositions were considered

in combination with other factors, such as slow loading rate and certain grades of steel. After comparing the results from testing in three alloys with different materials and loading rates, the galvanizing bath alloy *a2* (Table B-4) appeared to be the worst. However, the appearance of cracks also depended on loading rate and steel material. They also concluded that for a given grade of steel, LMAC occurred at lower stresses and strains in a Zn-Sn alloy than in a Zn-Pb alloy, and in these cases, Sn was found concentrated at the tips of cracks.

Feldman et al. (2010), which builds on the work described in Rudd et al. (2008) and also utilizes a L-N(T) specimen approach, found that the effect of some additives on the cracking susceptibility of galvanized steel structures caused a reduced strain capacity. While they studied baths that included Sn, Pb, and Bi, they organized galvanizing baths into three classes: Classes 1, 2, and 3, based primarily around Sn content as shown in Table B-5, where Class 3 was the most aggressive bath chemistry.

Table B-5: Galvanizing bath composition, classified for differentiating between steel resistances, adapted from (Feldman et al. 2010).

Classification	Percentage of Sn in the Galvanizing Bath
Class 1	Sn<0.1%
Class 2	0.1%<Sn<0.3%
Class 3	0.3%<Sn

They formulated their approach around the idea that cracks will develop when the strain demand, ε_E , exceeds the strain resistance, ε_R , as shown in Equation B-6:

$$\varepsilon_E < \varepsilon_R \quad \text{Equation B-6}$$

where ε_E was defined as the superposition of a non-stationary (time-variant) strain requirement component arising from temperature differences during the dipping process and a stationary (permanent) strain requirement component arising from the production of the semi-finished steel product used for fabrication and from the fabrication process.

The European General Galvanizer's Association (EGGA, 2014) gives some recommendations on galvanizing bath chemistry as described in the following. Notice that construction classes of inspection zone 1, 2, 3 are defined depending on profile depth, material strength and toughness of material.

- “For galvanizing of the vast majority of constructional steelwork (inspection zones 1 and 2 in Annex I), where high levels of component strain are not experienced during dipping, it is recommended that, in addition to the requirements of EN ISO 1461, the combined levels of tin, bismuth and lead shall not exceed 1.0%.”
- “For galvanizing of more susceptible structural steelwork (inspection zone 3 in Annex I) where other parameters may create a susceptibility to LMAC, it is prudent to operate the galvanizing bath with tighter controls on certain alloying elements, as given in Table B-6.”
- “Industrial experience has demonstrated that other commonly-used alloy elements (e.g. Ni and Al), when used at levels in common industrial practice, do not influence LMAC occurrence”.

Table B-6: Maximum composition in galvanizing bath, adapted from (EGGA, 2014).

Maximum composition in galvanizing bath (wt%)	
Sn	≤ 0.1%
Pb + 10Bi	≤ 1.5%

Residual Stresses

Many researchers have considered residual stress to be one of the most important factors causing cracks during galvanizing (Poag and Zervoudis, 2003; Beldyk, 2004; Elboujdaini, et al., 2004; Katzung and Wolf-Dieter, 2005; Kinstler, 2005; Mraz and Lesay, 2009; Feldmann, et al. 2006; Vermeersch, et al. 2011; Beal, et al. 2012; Kuklik, 2012; Cristol, et al. 2012; Dzupon, et al. 2013; EGGA, 2014). However, there is also general consensus that residual stress does not by itself produce LMAC during galvanizing; it is problematic in combination with other factors in the formation of cracks. Residual stress is not only a contributing aggravator of LMAC, but also can induce cracking brought about by distortion under high thermal gradients during galvanizing (James, 2008 and BS, 2009b).

The largest body of work researching the effects of residual stress is the FAMEGA project (Rudd et al., 2008), which argued that residual stress was the dominant cause behind cracking during the galvanizing process. The FAMEGA project used a systematic program to measure residual stress. First, they measured residual stresses from welding and finishing operations such as flame cutting and drilling, which introduced tensile residual stresses. Then they applied some methods to reduce the level of residual stress. As would be expected, they found that the residual stresses observed in welded sections were higher than the ones observed at other stages such as as-rolled and straightened state. The maximum residual stresses generated by straightening, lifting, and cooling were approximately 120 MPa; while the maximum amounts generated by welding were approximately 200 MPa.

Importantly, residual stress was shown to have a detrimental effect on cracking occurring during galvanizing. Two similar sets of full-scale half-depth end plate beam specimens were tested to investigate the influence of residual stress. Most of the specimens did experience cracking during galvanizing. However, when full-scale specimens were tested after a stress-relieving heat treatment was applied, they performed very positively.

The study performed by the Tomoe Corporation (2001) makes reference to “zinc assisted cracking” first being discovered during the 1970s in Japan, in large steel-pipe electrical tower structures. Because the cracks were observed primarily in the Heat Affected Zones (HAZ) of welded connections within the tower structures, it was concluded in the report that one of the requirements to develop zinc-assisted cracks is the presence of tensile stress, be it due to thermal stress or residual stress.

To determine the strain demand that would lead to cracking in liquid zinc, an experimental program was performed to test the tensile strength of steel coupons from EWR steel pipes with thicknesses ranging from 3.5 to 12 mm, as shown in Figure B-11. Specimens were treated to reproduce the conditions of a HAZ by placing specimens in a furnace that heated them to temperatures between 1200 °C and 1400 °C and subsequently being cooled to room temperature. The tensile tests were performed at a temperature of 419 °C or above.

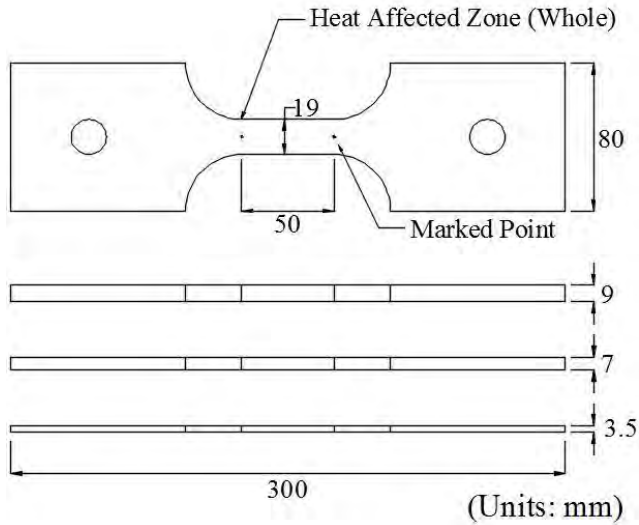


Figure B-11: Tensile steel coupons, adapted from (Tomoe Corporation, 2001).

The critical strain corresponding with cracking in liquid zinc, ϵ_{ZC} , was defined on the basis of strain measured over the 50 mm gage length ϵ_{ZP} , as presented in Equation B-7:

$$\epsilon_{ZC} = \epsilon_{ZP} + 0.2 \quad \text{Equation B-7}$$

Measured values of ϵ_{ZP} from STKT590 steel pipes produced in four different steel mills (Nippon Steel, NKK, Sumitomo Metals, and Kawasaki Steel) ranged between 1.5% and 8.5%. Steels with lower tensile strengths had higher strains at failure. For 55 ksi steels, measured values of ϵ_{ZP} ranged between approximately 1% and 5%, while for steels with a tensile strength of 50 ksi the ϵ_{ZP} values ranged between approximately 4% and 8.5%, as presented in Figure B-12.

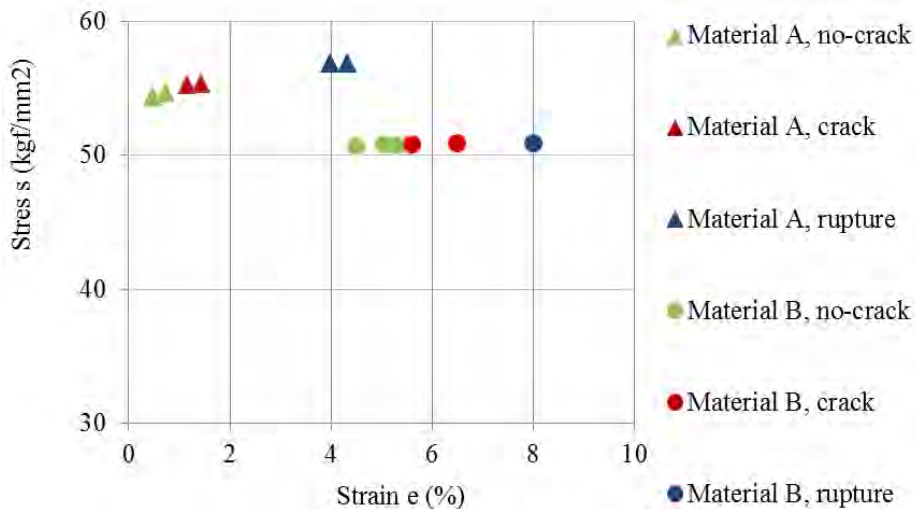


Figure B-12: Stress/Strain of tested specimens, adapted from (Tomoe Corporation, 2001).

A rearrangement of test results in terms of hardness showed that the tensile strain ϵ_{ZP} was inversely proportional to the hardness, although there was significant variability in the results. The variability in the strain ϵ_{ZP} decreased as the value of Vickers hardness increased, shown in Figure B-13. For steels with a Vickers hardness of approximately 200, the strain ϵ_{ZP} ranged approximately between 2.5 and 5.5%, and for specimens with a Vickers hardness of 300 the strain ϵ_{ZP} was approximately 0.5%.

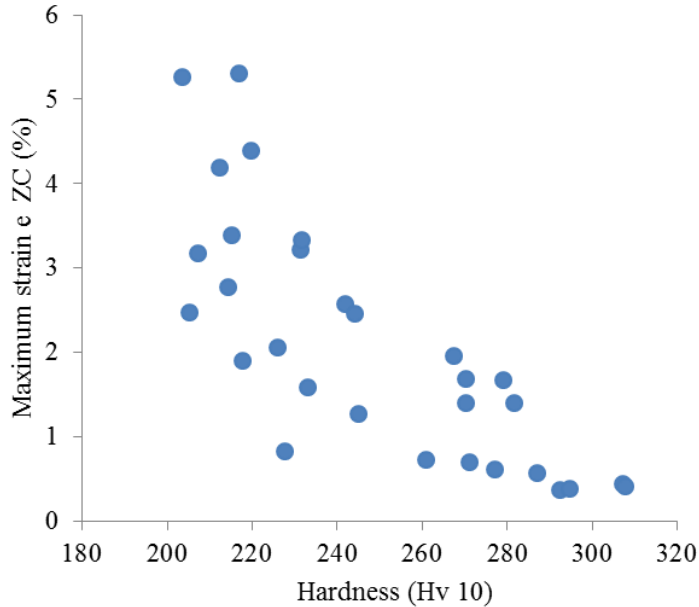


Figure B-13: Hardness vs. strain, adapted from (Tomoe Corporation, 2001).

After it was found that the presence of boron in the steel had a strong detrimental effect on LMAC, a new evaluation was performed with steels having improved chemistry. A total of 64 types of steel samples were tested to evaluate both the fracture stress ratio S_{LM} and the strain at crack occurrence in liquid zinc, ϵ_{ZC} . All evaluations were conducted in liquid zinc with a temperature ranging between 450 °C and 470 °C. The test results showed a similar relationship between ϵ_{ZC} and Vickers hardness, with the strain at failure decreasing with increasing hardness, as shown in Figure B-14.

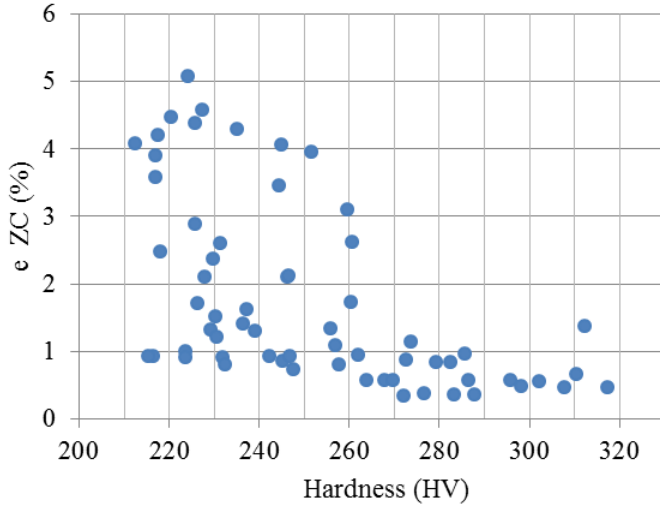


Figure B-14: Hardness vs. strain of steels having improved chemistry, adapted from (Tomoe Corporation, 2001).

Another significant finding from this experimental study was that there was a strong correlation between the strain at crack occurrence in liquid zinc ϵ_{ZC} and the fracture stress ratio S_{LM-400} , as shown in Figure B-15, so the Japanese researchers concluded that these two methods would coincide.

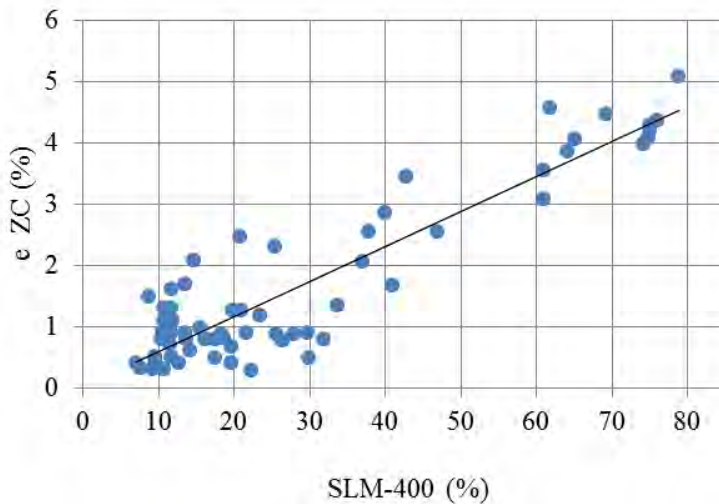


Figure B-15: Correlation between strain and SLM-400, adapted from (Tomoe Corporation, 2001).

Cold-working

Cold-working is a process of plastically deforming a metal at ambient temperature, which results in a strengthening and hardening effect. The yield strength of the cold-worked metal is increased, whereas ductility is decreased. When material is cold-worked, the hardness is increased and residual stresses may be introduced. Therefore, the effect of cold-working on the susceptibility of steel to LMAC is primarily through altering ductility and hardness, through the introduction of residual stresses. The formation of initial cracks and surface roughness due to cold-working is an important factor which may contribute to the occurrence of LMAC. Cold-working is one of the major facilitators of cracking during the galvanizing

process, as commonly agreed in the literature and specifications (Kinstler, 2005; James, 2008; Vervisch, 2009).

Severe cold work has been known to cause embrittlement of steel, which may be referred to as cold-working embrittlement or as strain-aging embrittlement. When steel is hot-dip galvanized, such embrittlement is accelerated due to the elevated temperature. Therefore, if cold-working cannot be avoided, it is recommended that steels which are insensitive to aging should be used if hot-dip galvanizing is planned (Katzung and Wolf-Dieter, 2005).

Sandelin (1954) studied the effect of cold-working on steel, quantified by bending radius. He concluded that cold-working is the most important single factor for cracking of galvanized steel. As a countermeasure, a bending radius of three times the section thickness ($3t$) was proposed to ensure that the induced strain level is not enough to reach the accelerated embrittlement condition. Various standards and codes also specify minimum bending radii to eliminate immediate crack formation during fabrication, although conflicts exist between these different specifications (Kinstler, 2005).

Dzupon et al. (2013) investigated the failures of yoke connectors of overhead power lines fabricated by cold-bending of steel plates and subsequent hot-dip galvanizing. It was concluded that the cracking failures were caused by the initial small surface cracks due to poor bending process which led to liquid metal assisted cracking during the galvanizing process.

Poag and Zervoudis (2003) studied the susceptibility of cold-formed Hollow Structural Steel (HSS) tubing to cracking during galvanizing under various zinc bath compositions. The effect of the degree of cold-working was investigated by considering different corner radii of the tube sections, including 0.28 in., 0.35 in., and 0.5 in. It was found that the tubes with roughest inside corners from folds related to heavy deformation exhibited higher susceptibility to cracking during galvanizing. It was also found that the unusual roughness due to wrinkles and folds during the heavy deformation of cold-forming made the steel tubing more susceptible to cracking; rough grinding the inside corners was very effective in improving crack resistance. Stress-relieving heat treatment prior to galvanizing was also effective in mitigating cracking incidences.

Kleineck (2011) performed an experimental study that considered the effect of bend radius on cracking susceptibility of high mast illumination poles (HMIP) during galvanizing. Both HMIP and mast arm specimens were tested; the bend radius to shaft thickness ratio at the base plate was compared against the recommended bend radius of three times the shaft thickness ($3t$). It was found that the poles that cracked from the galvanizing process all satisfied the recommended bend radius to shaft thickness ratio, while some other poles with smaller ratio than the code specification did not experience cracks. The results indicated that bend radius may play a role in initial crack formation, but is not likely the only triggering factor. Inside bend radii from $1.3t$ - $12.8t$ were considered in the study.

Clegg and Jones (1998) investigated LMAC of brass induced by gallium (Ga) through tensile testing and fracture toughness testing using cold rolled, leaded brass specimens. The tensile specimens were annealed at 900°C for two hours and then water quenched. These specimens were also pre-strained to levels of 4%, 5%, 6.5%, and 9.5% before testing. Three sets of fracture toughness specimens were used, each with different amount of cold-work (as received, 13% cold work, and 24% cold work). All fracture toughness specimens were stress relieved by heating to ensure stable crack propagation. The tensile tests all showed reduced ductility as a result of LMAC induced by the presence of gallium. It was observed that surface flaws induced by cold-work contributed to the initiation of LMAC cracks. For specimens with greater pre-strain levels, the plastic strain required to cause LMAC failure decreased and surface flaws needed to be less developed to initiate LMAC than for those with lower levels of pre-strain. Clegg and Jones (1998) concluded that stress and degree of cold-work are not sufficient to determine the propensity of LMAC crack. Rather, the surface texture plays a more important role. They also concluded that cold-work has little effect on the characteristics of LMAC crack propagation.

Geometry

The effect of member geometry on LMAC is closely related to the effect of thermally-induced stresses. When a member expands due to changes in temperature, the rate of expansion of the individual elements is dependent upon their thermal mass. Consequently, the expansion is not uniform throughout, with stiff sub-elements expanding more slowly and restraining deformations of thin sub-elements. This was confirmed in the study by the Tomoe Corporation (2001), in which it was found that stress demands in bridge plate girders during galvanizing were greatest when the temperature difference between thick and thin sub-elements was the greatest. Another important effect of abrupt changes in geometry is that they induce areas of highly localized stress, which are more sensitive to LMAC. There is a significant amount of experimental and analytical evidence that points to the fact that zinc-assisted cracks occur in locations with abrupt changes in geometry, often at the root of fillet welds.

As a result of differences in geometric shape, the prevention of LMAC is treated differently in the study for power transmission towers (which are manufactured primarily using welded steel pipes) than it was for steel bridge plate girders. The Tomoe study demonstrated that the deformation behavior during galvanizing was significantly different for these two types of members due to differences in geometry, and that the preventive measures taken to inhibit LMAC would be significantly different as a result.

For the case of galvanized steel pipes used in transmission towers, the measures to prevent LMAC focused primarily on the chemical composition of the steel, particularly on limiting the content of alloy elements. Detailing of steel pipes to prevent LMAC becomes more challenging when thick ring plates or gusset plates are welded to the pipes due to the uneven expansion during galvanizing. This problem was addressed by estimating the strain demand in liquid zinc ϵ_{ZA} , which is a function of the thickness of the plates.

Through multiple regression analysis, an equation was calibrated to estimate ϵ_{ZA} as a function of the thickness ratio and length ratio of the plate to the pipe, radius of curvature of the pipe, and pipe length. The resulting equation developed for grade STKT590 steel is as follows:

$$\epsilon_{ZA} = -0.383 + 0.247 TR - 0.087 L + 0.382 * \log\left(\frac{1}{\phi}\right) \quad \text{Equation B-8}$$

Where $TR = t_{pl}/t_p$ is the thickness ratio, t_{pl} is the thickness of the plate, t_p is the thickness of the pipe, L is the length of the pipe, and ϕ is the radius of curvature of the pipe. This equation was developed for cases in which the thickness of ring and gusset plates was the same. When the two thicknesses are different, the following expression was suggested for an equivalent thickness ratio:

$$TR_{eq} = \frac{t_R}{t_p} - 2.0 + 2.0 \frac{t_G}{t_R} \quad \text{Equation B-9}$$

where TR_{eq} is the equivalent thickness ratio, t_R is the thickness of the ring plate, t_p is the thickness of the pipe, and t_G is the thickness of the gusset plate.

While the previous research was performed for STKT590 steel, TEPCO Corporation had interest in extending the design provisions to lower strength steels (STK400 and STK540). The research carried out by TEPCO resulted in the following recommendation for lower strength steels. For STK400 steel:

$$\epsilon_{ZA} = 0.442 TR_{eq} - 0.442 \quad \text{Equation B-10}$$

For STK540 steel:

$$\epsilon_{ZA} = 0.350 TR_{eq} - 0.284 \quad \text{Equation B-11}$$

Based on these expressions, the study by TEPCO developed limits for plate thickness ratios to prevent cracking in Table B-7.

Table B-7: Limits for plate thickness ratio to prevent cracking, adapted from (Tomoe Corporation, 2001).

Steel grade	Critical plate thickness ratio for crack generation
STK400	Approximately 4.0
STK540	Approximately 2.7
STK590	Approximately 3.1 (without boron restriction) Approximately 5.0 (with boron restriction)

The recommendations made by TEPCO to prevent LMAC included applying welds with a smoother configuration, using two-pass welding, and performing more stringent inspections after galvanizing when the thickness ratio surpassed the critical values in Table B-7.

In the case of steel plate girders, it was concluded that the most important cause of LMAC was out-of-plane buckling of the girder web due to the restraint imposed by stiffeners and flanges as the thin girder web expands much more rapidly during the bath. The elastic buckling strength ratio was identified in the report as a key parameter for preventing LMAC, and it was suggested that this ratio be kept below a limit of 1.

The geometry of components determines whether tensile force or compressive force exist on the surface of steel structures when they are in the heating or cooling process. In addition, geometry also affects the drainage on a steel surface. In the FAMEGA project, Rudd et al. (2008) tested several geometries believed to be highly sensitive to LMAC, such as a half-depth end plate detail, drilled holes, and copes. For the case of the beam with a half-depth end plate, cracking occurred in the web 10-15 mm below the bottom of the end plate weld, near mid-depth of the beam. Drilled holes showed stress concentration effects, but rarely cracked in full scale tests.

James (2008) presented a case in which a joint of dissimilar thickness was studied; the connection geometry led to high local strain concentrations. This geometry difference at the joint, combined with other factors like high local hardness differences and weld defects, detrimentally initiated cracking during galvanizing.

Overall, the diversity of geometries of steel structures regularly used in practice makes it difficult to design typical full-scale test specimens. However, based on these studies, it is appropriate to conclude that geometry is an important factor with respect to the susceptibility of steel sections to cracking during galvanizing.

Thermal Stresses

The effect of thermal stresses on LMAC is a complex problem because it is dependent on many parameters, including: the geometric shape of the member being galvanized, the thermal mass of the various sub-elements that make up the member, the relative stiffness of the various sub-elements that make up the member, the angle at which the member is immersed in the galvanizing bath, the rate of speed at which it is immersed in the galvanizing bath, and the amount of time the member is immersed in the galvanizing bath.

The primary concern regarding thermally-induced stresses is that they contribute to the development of LMAC during the galvanizing process, which may be related to fatigue cracks that form in the steel during the service life of the structure.

The study performed by the Tomoe Corporation (2001) concluded that one of the requirements for developing LMAC is the presence of tensile stress due to thermal or residual stresses. In the Tomoe study,

a plate girder with welded vertical and horizontal stiffeners was examined. Cracking was studied both during the deformation increase period corresponding to when the girder is being submerged in the molten zinc, and then again during the deformation decrease period, after the totality of the girder had made contact with the molten zinc. The plate girder had horizontal and vertical stiffener plates as dictated by Japanese bridge design practice, as shown in Figure B-16. Horizontal stiffeners were placed only on one side of the girder, with 35-mm clearance gaps to allow smooth flow and dripping of the molten zinc at the intersections between the horizontal and vertical stiffeners.

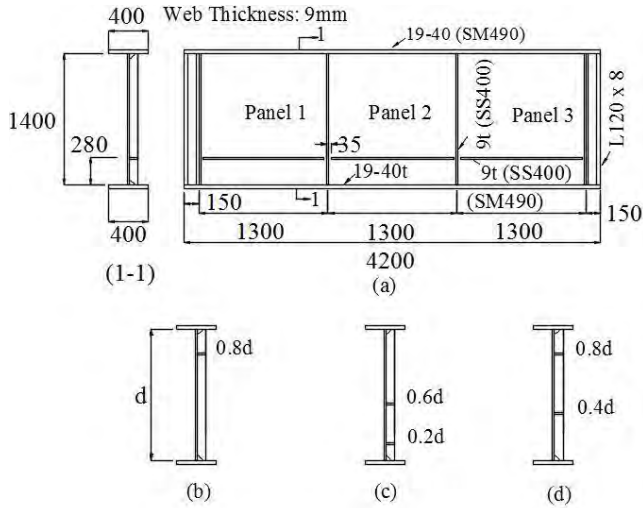


Figure B-16: Steel plate girder, adapted from (Tomoe Corporation, 2001).

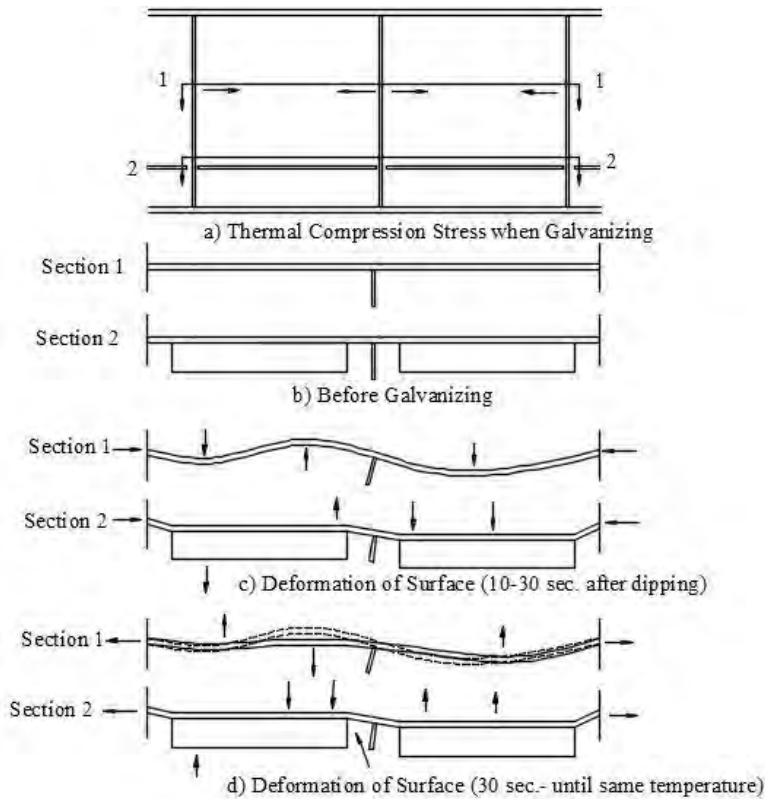


Figure B-17: Deformation of steel plate girder, adapted from (Tomoe Corporation, 2001).

In the portion of the study examining the deformation increase period, in all instances the cracks were observed at the fillet weld, at locations where the horizontal stiffener had been interrupted. (Horizontal stiffeners were placed either at the top or at the bottom of the plate girder.) In some instances, cracks were observed as occurring at the stiffener at the top of the girder, *prior to any contact with the molten zinc*, which clearly showed that the primary driving force was due to the thermally-induced deformations acting in combination with the interruption of the stiffener. Some observed deflection modes are shown in Figure B-17.

The Tomoe study included both finite element simulations and actual measurements of steel pipes and a segment of plate girder immersed in a galvanizing bath at two different rates of speed (0.2 m/min and 5.5 m/min). The plate girder was found to experience significant out-of-plane distortions of the web during galvanizing, caused by larger thermal deformations in areas of the girder that were unrestrained. The measurements presented in Figure B-18 showed that out-of-plane deformations were larger for the faster dipping speed of 5.5 m/min, and that those deformations led to very large stress demands in the clearance gaps of the horizontal stiffeners. LMAC appeared for both dipping speeds at both ends of the horizontal stiffener in the central panel.

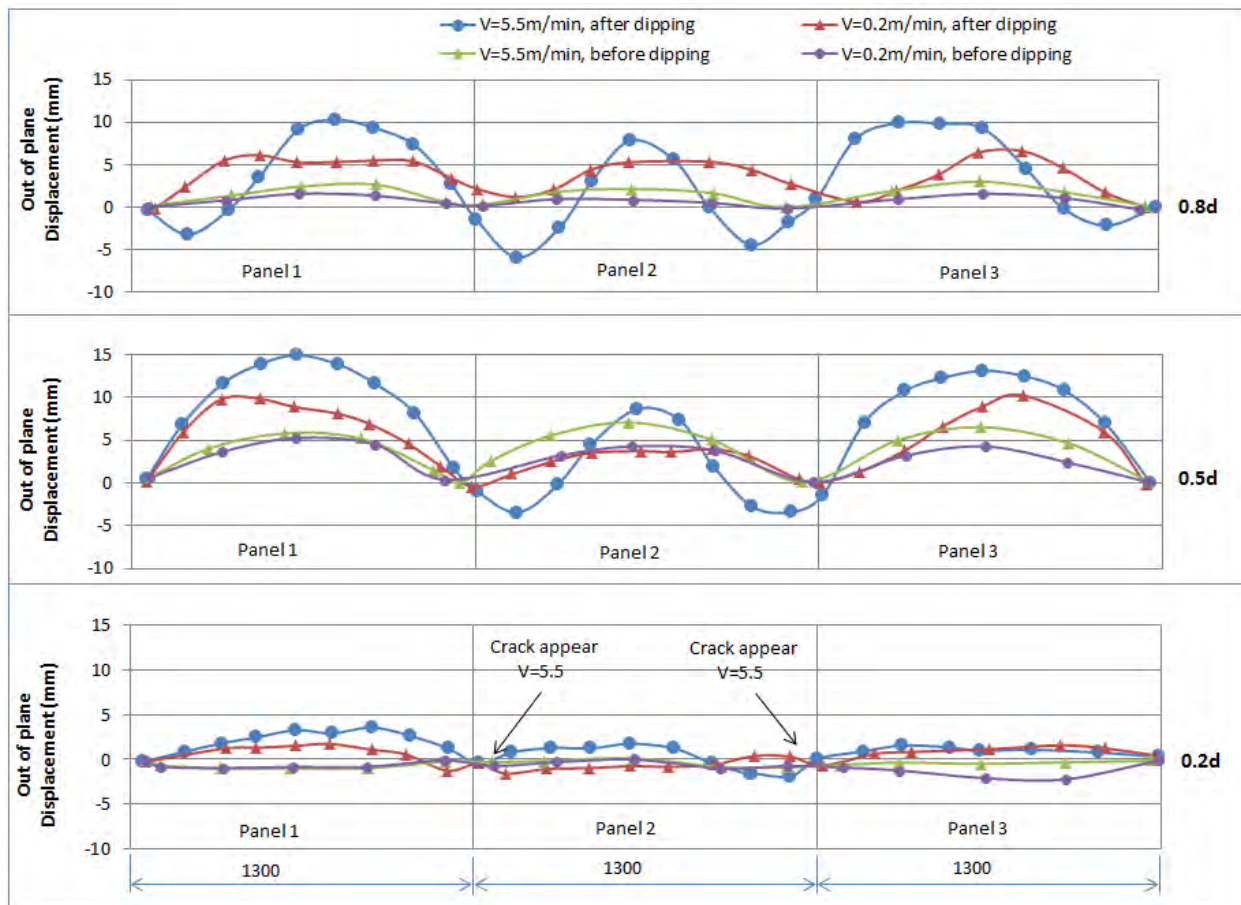


Figure B-18: Out of plane deformation vs. dipping rate, adapted from (Tomoe Corporation, 2001).

It was also demonstrated that dipping speed had a critical effect on thermal stresses. The computer simulations and test measurements showed that in steel pipes the thermal stress demands were significantly

lower for the faster dipping speeds. In the case of the slower dipping speed, the maximum stress generated in tension was approximately 25 kgf/mm², while for the faster dipping speed the maximum tensile stress was below 5 kgf/mm². These results are shown in Figure B-19 and Figure B-20. The greatest stress demands were calculated in the portion of the pipe near the surface of the zinc bath, which is consistent with the higher stress demands calculated for lower dipping speeds. One of the most significant conclusions of the study was that this behavior was different for members with gusset plates, in which there was a significant difference between the thickness of the gusset plate and the thickness of the steel pipe. It was concluded that for gusseted members, thermally-induced stresses may be quite large regardless of immersion speed.

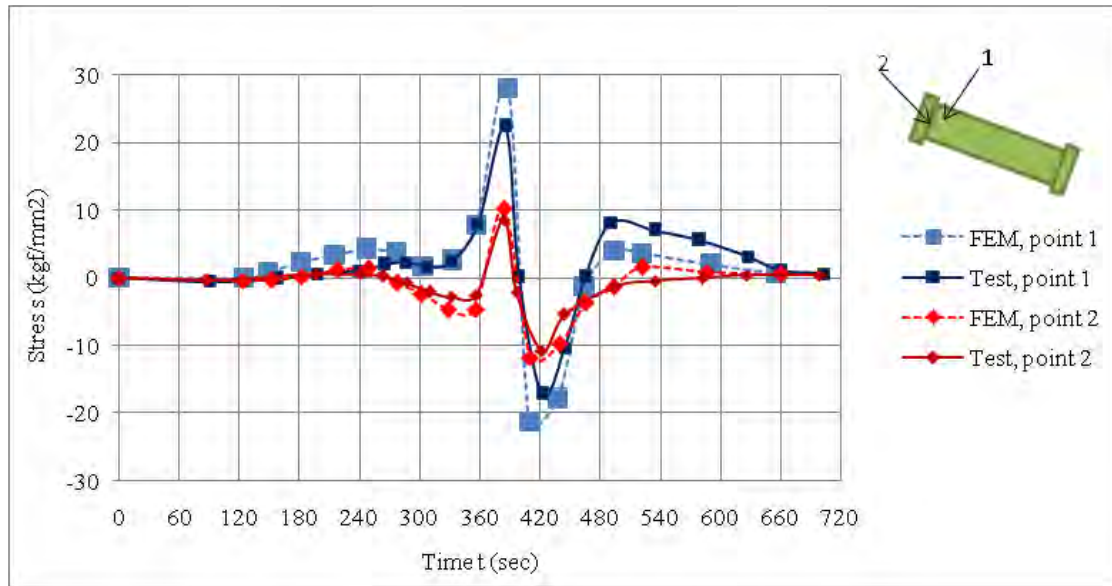


Figure B-19: FEM results vs. Test results (V=0.2m/min.), adapted from (Tomoe Corporation, 2001).

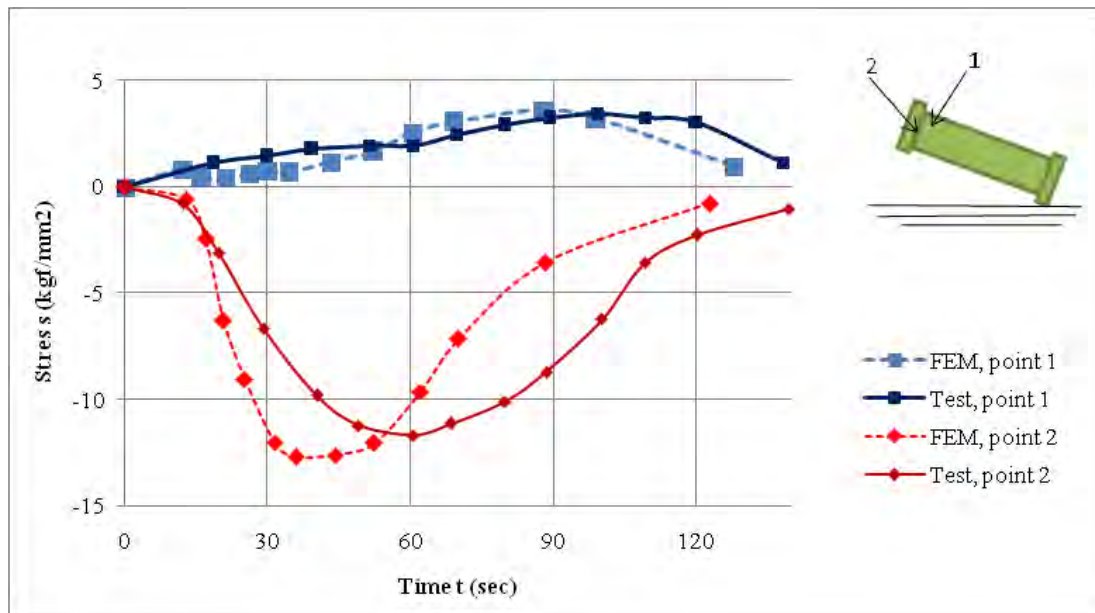


Figure B-20: FEM results vs. Test results (V=5.5m/min.), adapted from (Tomoe Corporation, 2001).

A presentation made by Higgins (2014) introduced a research study conducted by Southwest Research Institute in the 1970s, which found a significant thermal gradient between an HMIP shaft and welded base plate. Thermocouples were used to measure temperature in the pole shaft and base plate elements throughout the galvanizing process. The temperature difference was found to be as much as 360 F between the shaft and the base plate, occurring approximately three minutes after the HMIP structure was submerged in the galvanizing bath.

The University of Texas at Austin performed a succession of studies focused on galvanized High Mast Illumination Poles (HMIPs), (Kleineck, 2011). The work performed by UT was initially focused on optimizing HMIP geometry for fatigue resistance (Pool, 2010). When they observed the performance of a non-galvanized HMIP (black steel) against a galvanized HMIP of the same design and material, they discovered that the galvanized specimen had small cracks at the toe of the full penetration baseplate-to-shaft connection at every location of a cold bend.

At this point, the UT work shifted to examine factors such as bend radius, chemistry, and diameter-to-pole thickness on the fatigue performance of galvanized HMIP structures. Interestingly, they found that these factors played a minor role when compared against thermal effects. They measured the thermal gradient of eight HMIPs put through the galvanizing process at two different galvanizing plants over three dates (January 2010, June 2010, and February 2011), finding significant differences in the thermal response between different locations of measurement on the HMIP.

While the locations and patterns of cracks were found to be different from specimen to specimen, the UT researchers found that the ratio of pole shaft diameter to shaft thickness could be a strong indicator of the probability of crack occurrence. To verify the influence of that ratio, they developed a finite element method to study three HMIP models having different shaft thicknesses. After surveying the effect of dipping rate and dipping angle, the effects of which they found to be small, they concluded that decreasing the ratio of pole shaft diameter to shaft thickness was the best way to reduce the likelihood of formation of cracks during galvanizing.

Hardness

Extensive research performed in Japan and US has identified a correlation between hardness of the heat affected zone (HAZ) due to welding, thermal cutting, oxy-fuel cutting, and flame cutting and propensity of steel to cracking during and even after galvanizing.

Kinstler (2005) examined steel beam copes cut with alternate cope cutting sequences. Cracking found after galvanizing at the copes all seemed to have initiated from a surface irregularity, notch, or stress concentration. Thermal cutting had increased the hardness of the cut surface relative to the base metal, and the radius of the cope also exhibited slightly higher hardness than the straight portions of the cope.

McDonald (1975) studied the effect of galvanizing on welded metal samples with high strength, which were subjected to quenching and tempering to simulate Heat Affected Zones (HAZ) from welding. It was hypothesized that high hardness would facilitate hydrogen embrittlement, since the specimens were also hydrogen-charged electrolytically or through acid pickling. However, he found that the high temperature associated with typical galvanizing process softened the high hardness in the HAZ of the welds, and therefore eliminated the potential for hydrogen embrittlement induced cracking when the hardness was below $R_C = 36$ (which is approximately 345 HV). Increasing galvanizing time led to a greater reduction in hardness values. Kikuta, et al. (1986) also showed similar effect on Y-groove welding. Aoyama (1994) also found a lessening of the residual welding stress after galvanizing by studying full-scale effects in highway bridges.

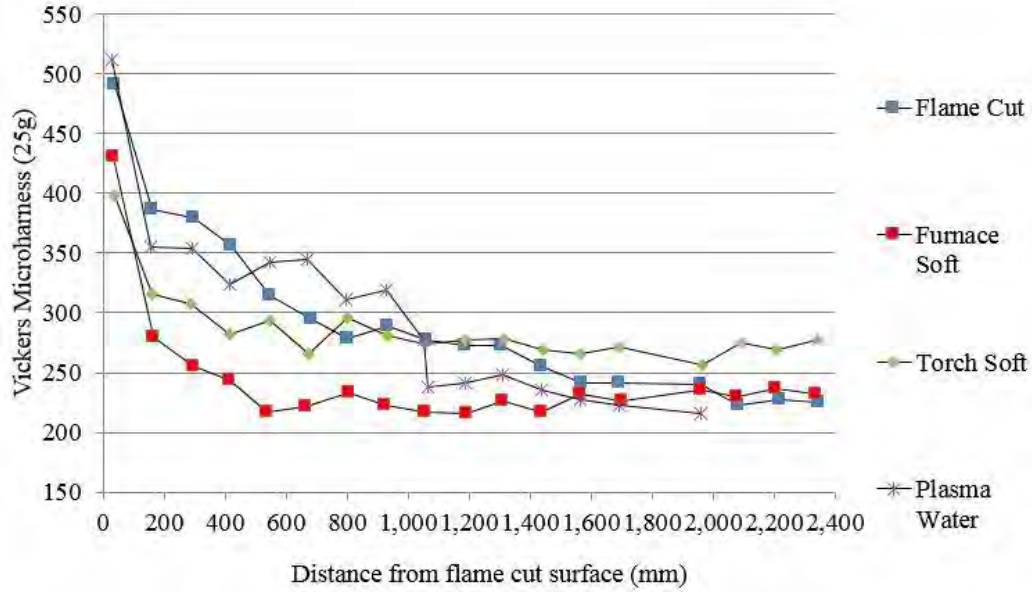


Figure B-21: Micro-hardness (Vickers 25g load) near the cut surface of HY-80, adapted from (Elboudjaini, et al., 2004).

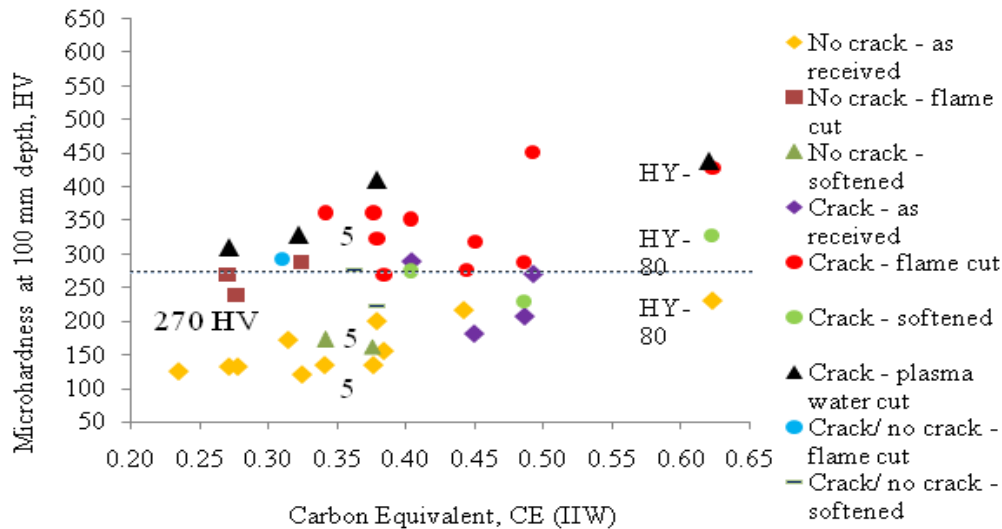


Figure B-22: Cracking susceptibility as a function of micro-hardness for fifteen steels of a range of carbon equivalents, adapted from (Elboudjaini, et al., 2004).

Elboudjaini, et al. (2004) investigated the effect of the surface hardness (Figure B-21) of steel on crack susceptibility. The trend of increasing susceptibility with higher hardness was confirmed based on experiments with fifteen steels with different chemical composition, as presented in Figure B-22. It was also found that cracking was more likely to occur when the hardness level was greater than 270 HV, but this conclusion was not intended to imply that steels with hardness below 270 HV are immune to cracking. In fact, a threshold hardness was identified between 250 and 300 HV, depending on the thickness of the steel and other variables (Kinstler, 2005). Consistent with the findings of Poag and

Zervoudis (2003), thermal treatment used to soften the surface prior to galvanizing was found to be an effective strategy in reducing the propensity to cracking. It was also concluded that steel composition cannot be used solely to determine hardness, because other processes applied during fabrication such as cold working, flame cutting, and welding, among other sources of stress concentration, will affect hardness.

Kominami et al. (1985) investigated the effect of welding factors on the critical stress of steel in molten zinc. An inverse linear relationship was established between the critical stress and the maximum Vickers hardness in the heat affected zone (HAZ), as shown in Figure B-23.

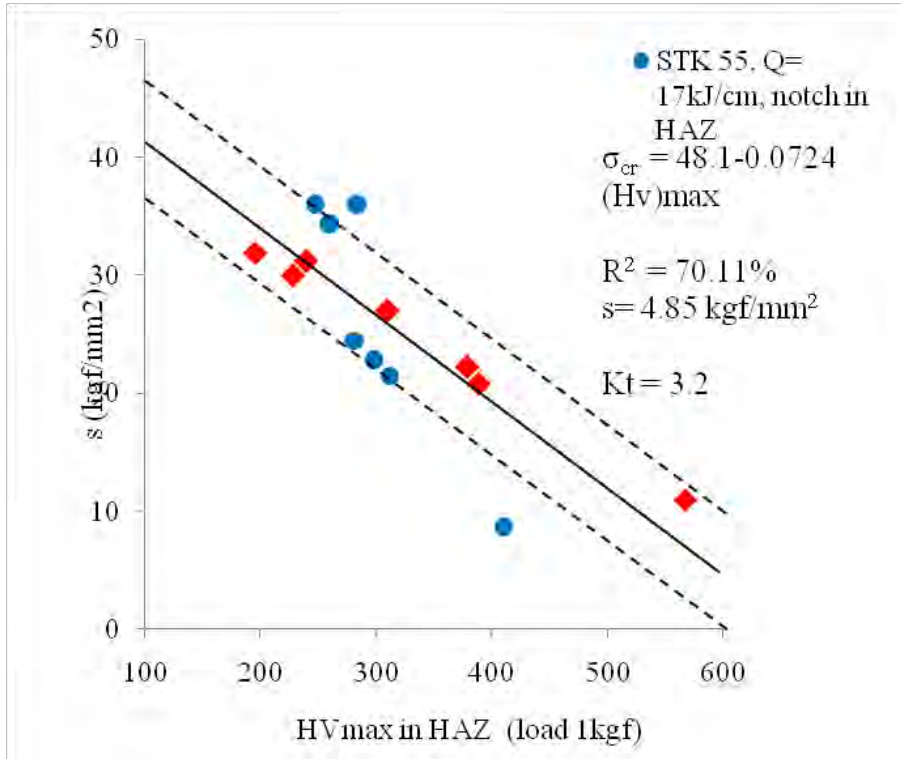


Figure B-23: Relationship between critical stress and max. Vickers hardness, adapted from (Kominami, et al., 1985).

Kikuta, et al. (1986) studied Y- Groove Cracking tests in materials with yield strengths in the range of 270MPa (40 ksi) to 800MPa (116 ksi), as shown in Figure B-24. They concluded that the critical condition for LMAC was determined by a relationship between the level of constraint (related to plate thickness) and the maximum hardness in HAZ (Hv_{max}), as shown in

Figure B-25 and Figure B-26.

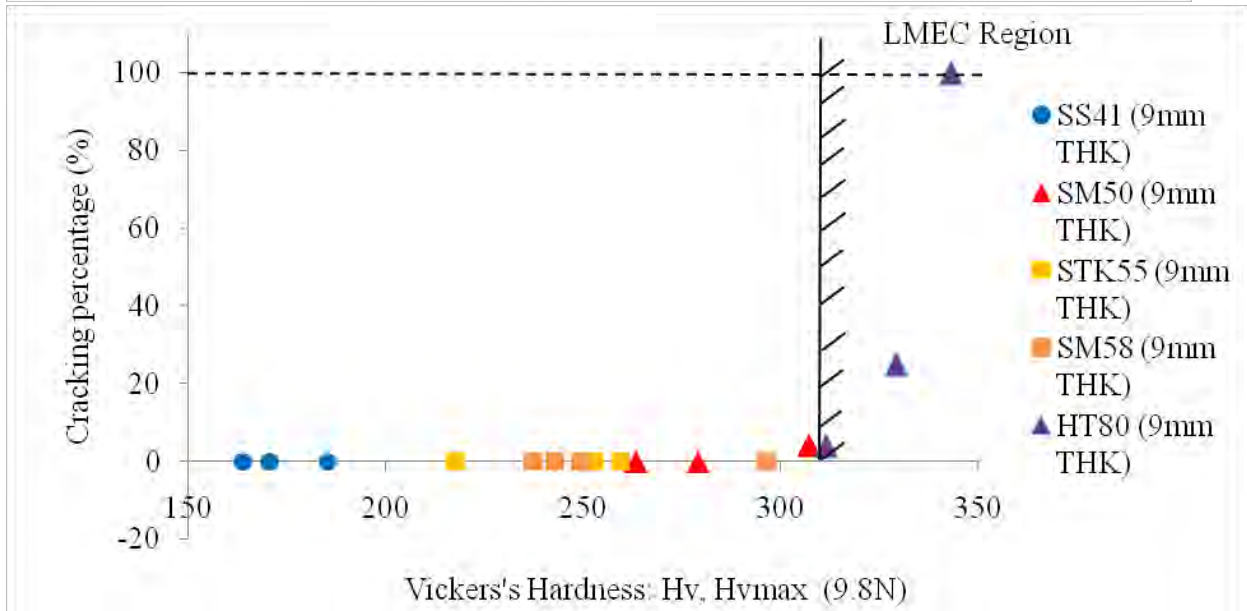
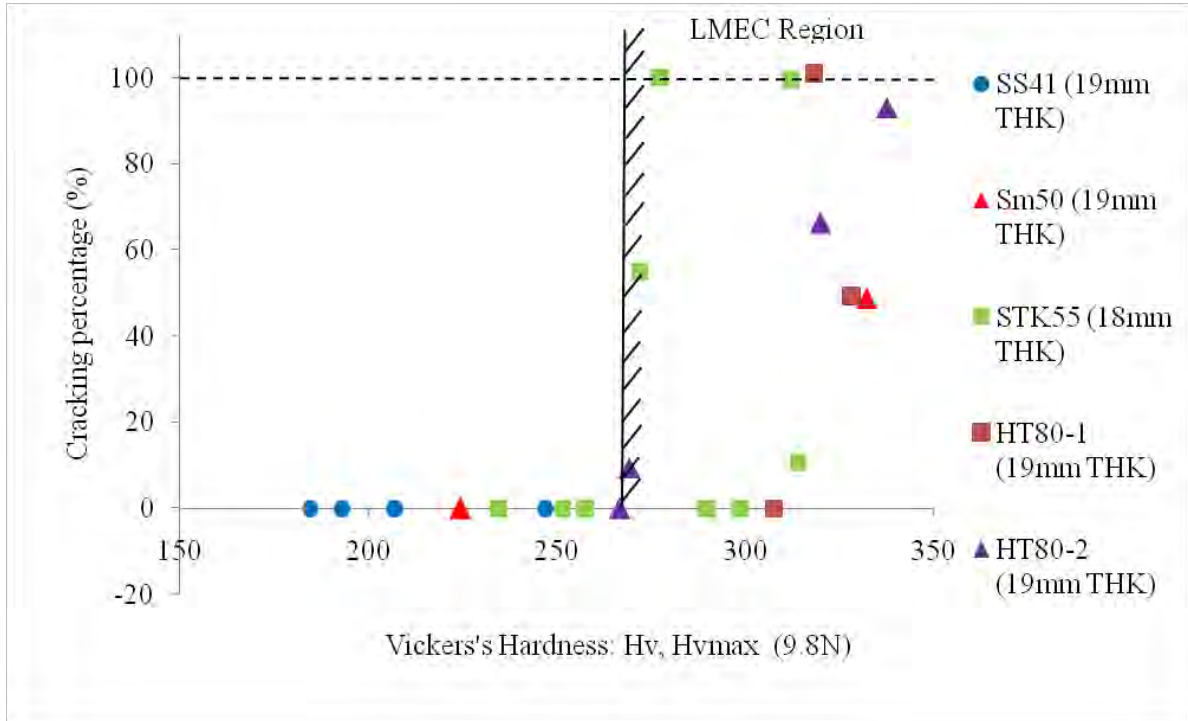


Figure B-24: Effect of Hv max. on cracking percentage in Y-Groove Cracking Test specimen, adapted from Kikuta, et al. (1986).

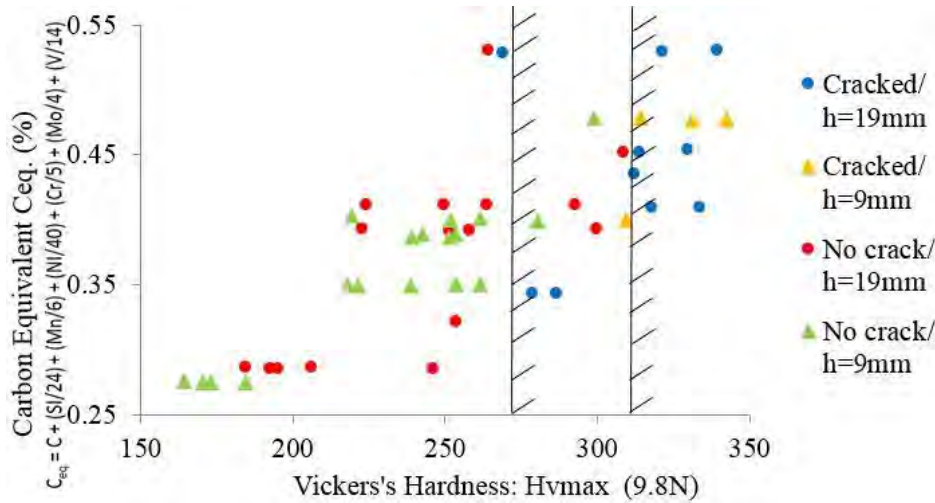


Figure B-25: Estimation of LMACC occurrence region from the relation between Ceq. and Hv max., adapted from Kikuta, et al. (1986).

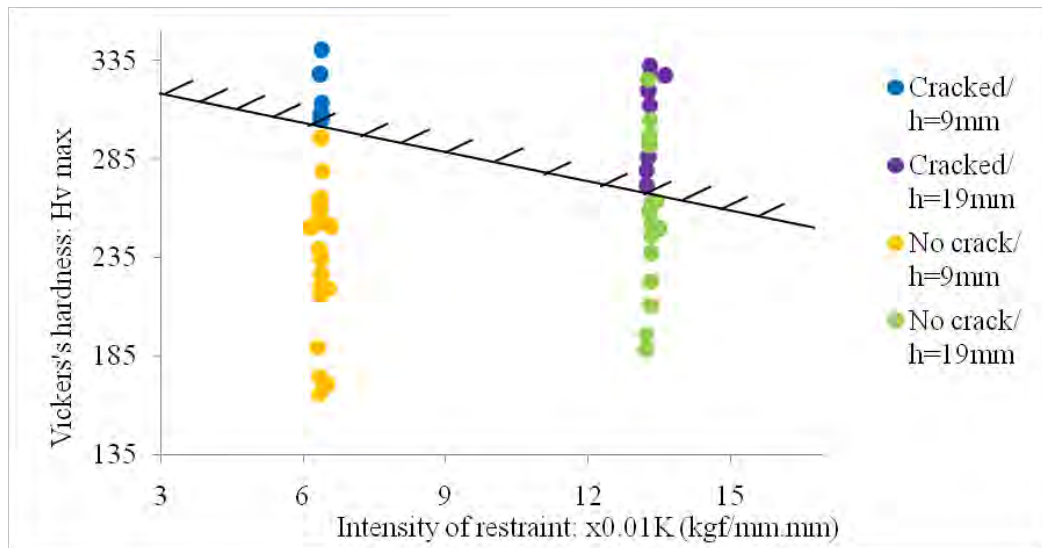


Figure B-26: Estimation of LMACC occurrence critical condition obtained by the relation between intensity of restraint and Hv max., adapted from Kikuta, et al. (1986).

Mraz and Lesay (2009) investigated several failure cases of hot-dip galvanized welded structures. Large cracks were found in the vicinity of welds. Hardness measurements showed levels of 274 HV5 hardness in a tube-to-plate weldment and 360 HV5 hardness in the HAZ. They concluded that crack initiation was due to a combination of hydrogen embrittlement and high-hardness microstructure and residual external stress. LMAC was considered to be the primary mechanism for crack propagation.

Dzupon et al. (2013) investigated failures of yoke connectors in overhead power lines that were fabricated by cold-bending of steel plates and subsequently hot-dip galvanized. High hardness values (from 325-364 Vickers) were measured in the vicinity of cracks.

Welding Process and Effects

Welding processes generate heat affected zones (HAZ) with high hardness, induce residual stresses, and may introduce discontinuities or initial cracks. All of these effects may contribute to cracking of welded steel structures subjected to hot-dip galvanizing. The effects of hardness and residual stresses have been discussed in other sections in this report.

Heat affected zone cracks, also called toe cracks in the case of fillet welds, are believed to occur due to the combination of three factors, including a sufficient level of hydrogen, sufficiently sensitive materials (hardenability), and sufficiently high level of stress. Therefore, HAZ cracks may also be referred to as hydrogen-assisted cracking. However, as previously discussed, McDonald (1975) found that the galvanizing process can eliminate the potential for hydrogen-induced cracking when the hardness is below $R_C=36$ (345 HV) because the high temperature environment softens the high hardness in the HAZ. Therefore, except for high strength steels, high residual/applied stress and the presence of stress concentrations may be more primary drivers of cracking for weldments subject to hot-dip galvanizing.

In the FAMEGA study, Rudd et al. (2008) showed that weld residual stress has a detrimental effect on cracking during galvanization. A full-scale test specimen was constructed by welding a half-depth end plate to the end of a hot-rolled I section beam. The area around the weldment was observed to have increased stresses, which when combined with other environmental stresses, were of a magnitude capable of exceeding the yield stress. In addition, the temperature gradient experienced during the galvanizing process further exacerbated stresses at the weldment.

Welding profiles and welding process can also result in discontinuities which serve as stress concentrations. Aichinger & Higgins (2006) performed a Six-Sigma study to better identify the causes and variables to minimize the occurrences of weld toe cracks. This study revealed that weld profile, especially at bend-lines, may act as a stress-riser/concentrator, and the welding process can produce discontinuities. They also suspected that weld toe cracking is initiated by LMAC, but that the propagation is led by stress. Kuklik (2012) pointed out that every weld is a notch where stress can concentrate.

Beldyk (2004) discussed conditions leading to the occurrence of galvanized-induced cracks. Silicon was believed to play a role in delayed post-galvanization welding cracks, because silicon may induce excess and delayed transport of weld filler alloying elements. During galvanizing, the high temperature of the molten zinc may weaken the weld by causing a redistribution of the alloying elements. Moreover, excessive silicon in the weld filler metal can introduce a large and undesirable buildup of zinc on the weld surface and change the stress profile in the weld.

Masayoshi et al. (2007) performed an experimental study examining the effect of hot-dip galvanizing on fatigue strength of steel welded joints. They concluded that the fatigue strength of welded joints decreased significantly due to hot-dip galvanizing. The reason was believed to be due to the decrease of surface hardness and compressive residual stress, in addition to other factors associated with hot-dip galvanizing.

Hydrogen Embrittlement

Hydrogen embrittlement is one of the suspected causes to weldment cracking during galvanizing. Three factors contributing to hydrogen embrittlement associated with galvanized steels are:

- Atomic hydrogen (from manufacturing of the steel, the acid pickling reaction, and fluxing and galvanizing conditions).
- Stress (from cold-working, welding, heat treatment, and applied loads).
- Material susceptibility to cracking (type of steel).

Carpio, et al. (2010) performed hydrogen concentration tests on prismatic specimens with dimensions 6 x 6 x 10 mm (0.24 in. x 0.24 in. x 0.39 in.), which underwent pre-galvanizing and galvanizing processes. They determined that hydrogen content was mainly increased through the processes of fluxing and immersing in zinc kettle. Pickling created only a small amount of the final hydrogen absorption due to the

inhibitor presence, which did not allow for reactions to occur between acids and steel. The Zn-Sn galvanizing bath introduced more hydrogen (H) than the Zn-Pb galvanizing bath did, which supported the statement that tin (Sn) was more severe when compared to lead (Pb) in terms of introducing the hydrogen atom to specimens.

A test machine (ELTRA ONH-2000) was used to determine hydrogen concentration at three different through-thickness locations where hydrogen could accumulate from fluxing: the steel base metal, the Fe-Zn phases, and the pure Zn layer. They found that hydrogen concentrations were 50.3ppm, 74.4ppm, and 0.4ppm in the Zn-Fe intermetallic layer, the pure zinc layer, and the steel base, respectively. Hydrogen concentrated predominantly in the Zn-Fe intermetallic layers and exterior zinc layer, but not in the steel base metal. The amount of hydrogen in the steel base metal was considered too small to cause hydrogen embrittlement. However, the negative sign here raised a question on the precision of the test results. Furthermore, the final hydrogen concentration depended on steel grade. For steel with strength greater than 500MPa (73 ksi), the hydrogen in the steel base metal was residual and did not have enough quantity to produce embrittlement. However, with the addition of certain conditions that steel may experience, such as quenching, tempering, welding, flame cutting or severe cold working, hydrogen embrittlement could become a concern.

In general, there is broad agreement in the literature that the greater the steel strength (or hardness), the greater the probability of hydrogen embrittlement occurring. Many documents state that hydrogen embrittlement can become a problem in steels with tensile strengths greater than 800MPa (116 ksi), including Rudd et al. (2008) and Vermeersch, et al. (2011). In accordance with this behavior characterization, ASTM (2007) states that “In practice hydrogen embrittlement of galvanized steel is usually of concern only if the steel exceeds 150 ksi [1100 MPa] in ultimate tensile strength, or if it has been severely cold worked prior to pickling.” It should be noted that martensite steels are more susceptible to hydrogen embrittlement than ferrite-pearlite steels.

Brahimi, et al. (2009) performed tests on galvanized ASTM A490 fasteners (minimum tensile strength 150MPa) using incremental step loading in accordance with test method ASTM F1940. For one group of specimens, they found that hydrogen embrittlement played an important role in decreasing fracture strength by 40%, accompanied by a drop of specimen hardness to 45HRC from an initial value of 51HRC. The time dependence of embrittlement suggested that hydrogen was blocked by the intermetallic coating layer, although a portion was released under thermal cycle of galvanizing. For another group of specimens with surface hardness 36.5HRC, there was no change in fracture strength.

Mraz and Lesay (2009) studied steel structures that failed after hot dip galvanizing. These welded structures were constructed with a steel grade of 355MPa (52 ksi). Mraz and Lesay reasoned that the presence of transgranular fracture in the HAZ suggested that HE was responsible for the crack initiation, while the presence of intergranular fracture showed that LMAC was responsible for the crack propagation.

Work performed by Padhy and Komizo (2013) included a broad literature review of hydrogen in steel weldment. They state: “Reducing hydrogen is the best way to reduce the risk of hydrogen assisted cracking (HAC). This can be achieved by using some heat treatment to the steel and the weld. Hydrogen content in steel weldments exists as diffusible and residual hydrogen. While the residual hydrogen is permanently trapped in the welds and plays no role in HAC, the diffusible hydrogen is able to diffuse within or out of the weldment and is responsible for HAC.”

Some recommendations have been developed, such as those found in BCSA (2005), BS (2009b), and ASTM (2007) that can be used to minimize hydrogen induced cracking. The BCSA (2005) states that: “To minimize the hydrogen cracking: inhibited acid should be used to chemically clean the steelwork. The time the steelwork spends in the acid pickling path should be minimum necessary to allow chemical cleaning of the steelwork. Extended pickling times may result in excessive absorption of hydrogen, especially in susceptible areas such as the HAZ adjacent to the weld”. The ASTM (2007) standard suggests heating the steel to 300°F [150°C] after pickling and before galvanizing. In another statement of the ASTM (2007): “Abrasive blast cleaning followed by flash pickling may also be employed when over-pickling is of concern

or when very high strength steel, ultimate tensile strength higher than 150 ksi [1100 MPa], must be galvanized. The abrasive blast cleaning does not generate hydrogen while it is cleaning the surface of the steel. The flash pickling after abrasive blast cleaning is used to remove any final traces of blast media before hot-dip galvanizing.”

In summary, hydrogen embrittlement is not considered as a main cause of cracking during galvanization of typical steel highway structural components, which are generally not constructed of high-strength steels. Hydrogen embrittlement may be an accompanying aggravator to LMAC, which can combine with other causes in helping to initiate and propagate cracking. Reducing hydrogen, which is one of the three factors contributing to hydrogen embrittlement, below critical levels seems to be the best way to decrease the risk of hydrogen embrittlement. Many documents suggest how to reduce hydrogen and have been used practically and successfully in industry, including BCSA (2005), BS (2009b), and ASTM (2007).

Strain Age Embrittlement

Strain age embrittlement is another phenomenon that can be related to cracking during galvanizing. As stated in ASTM (2007), “Strain-aging refers to the delayed increase in hardness and strength, and loss of ductility and impact resistance which occur in susceptible steels as a result of the strains induced by cold working.”

The severity of strain age embrittlement depends on the time of aging, the amount of strain, and the steel composition (carbon and nitrogen content). Strain aging occurs very slowly at room temperature, but rapidly at elevated temperatures, such as those present in the galvanizing process. For example, the strain aging effect produced in a period of six months at a temperature of 21°C was the same as that reached in only 10 minutes when a specimen was exposed to a temperature of 150°C (Kinstler, 2005).

For heavily cold-worked material, heat treatment should be used to relieve stresses prior to galvanizing. For hollow steel sections with ratio of bend radii to the thickness of shaft section less than three, ASTM (2007) recommends hot bending to minimize strain age embrittlement. Some elements may also be added to the steel chemistry to form nitrides in order to limit the effects of strain aging such as: aluminum, vanadium, titanium, niobium and boron. The most commonly-used element is aluminum, and most modern steels are aluminum-killed steels (Goyal, 2012).

Strain age embrittlement has been a known phenomenon for more than 100 years, and many recommendations have been successfully applied. Therefore, strain age embrittlement is no longer a primary concern in structural steelwork in general, nor is it believed to be particularly problematic in the galvanizing process, as stated in BCSA (2005), James (2008), BS (2009a) and Dzupon et al. (2013).

Effect of Galvanizing on Fatigue Strength of Steel Structures

The appearance of cracks resulting from the galvanizing process has raised concerns regarding the fatigue life of galvanized steel structures. Koenigs (2003) discovered that galvanization had a detrimental effect on the fatigue life of HMIPs. While all non-galvanized specimens had fatigue life of Category E' (AASHTO fatigue categories A, B, C, D, E, E') or better, the galvanized specimens showed fatigue lives less than Category E'. The studies performed by Richman (2009), Pool (2010), and Stam (2011) also indicated that the fatigue life of traffic structures was reduced under the influence of galvanizing.

Work performed by Vogt et al. (2001) presents a compelling case as to the source of the fatigue strength disparity between galvanized steel and otherwise-identical black steel. Vogt et al. (2001) tested a 1.42-mm thick, cold-rolled steel sheet specimen. The steel was galvanized at 450°C in a zinc bath. First, the fatigue strength values at 10^6 cycles to failure of the galvanized steel were predicted according to Bastenair's model, (Lieurade, 1982). It was clear that fatigue strength decreased as coating thickness increased.

Then, testing was performed at a stress level 10% higher than the fatigue limit, and the specimen was observed to examine the distribution of fatigue cracks. Characteristics of the galvanized coating were found

to affect the crack distribution. A correlation was identified between micro-cracking in the coating (which occurred during galvanizing) and cracking in the steel substrate (due to fatigue). Cracks in the galvanizing coating were believed to propagate in the substrate once the total thickness of the galvanizing coating was cracked. Therefore, this work showed that microscopic flaws in the galvanized coating may act as initial flaws for fatigue cracks in the base metal to initiate from under fatigue loading.

APPENDIX C

Stress-Strain Curves

Subtask 6.1: Steel Composition and Galvanizing Composition

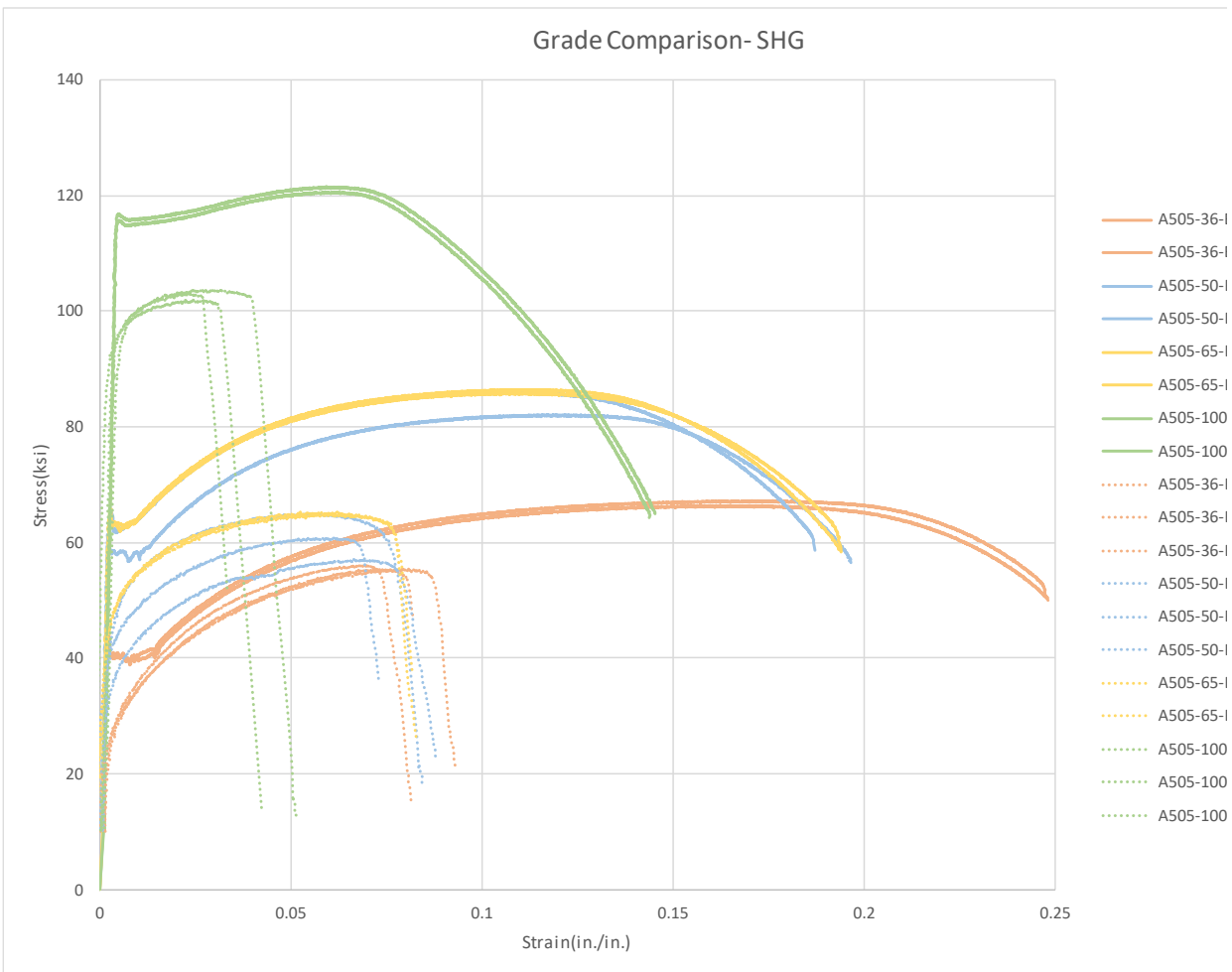


Figure C-1. Effect of SHG zinc on all steel grades.

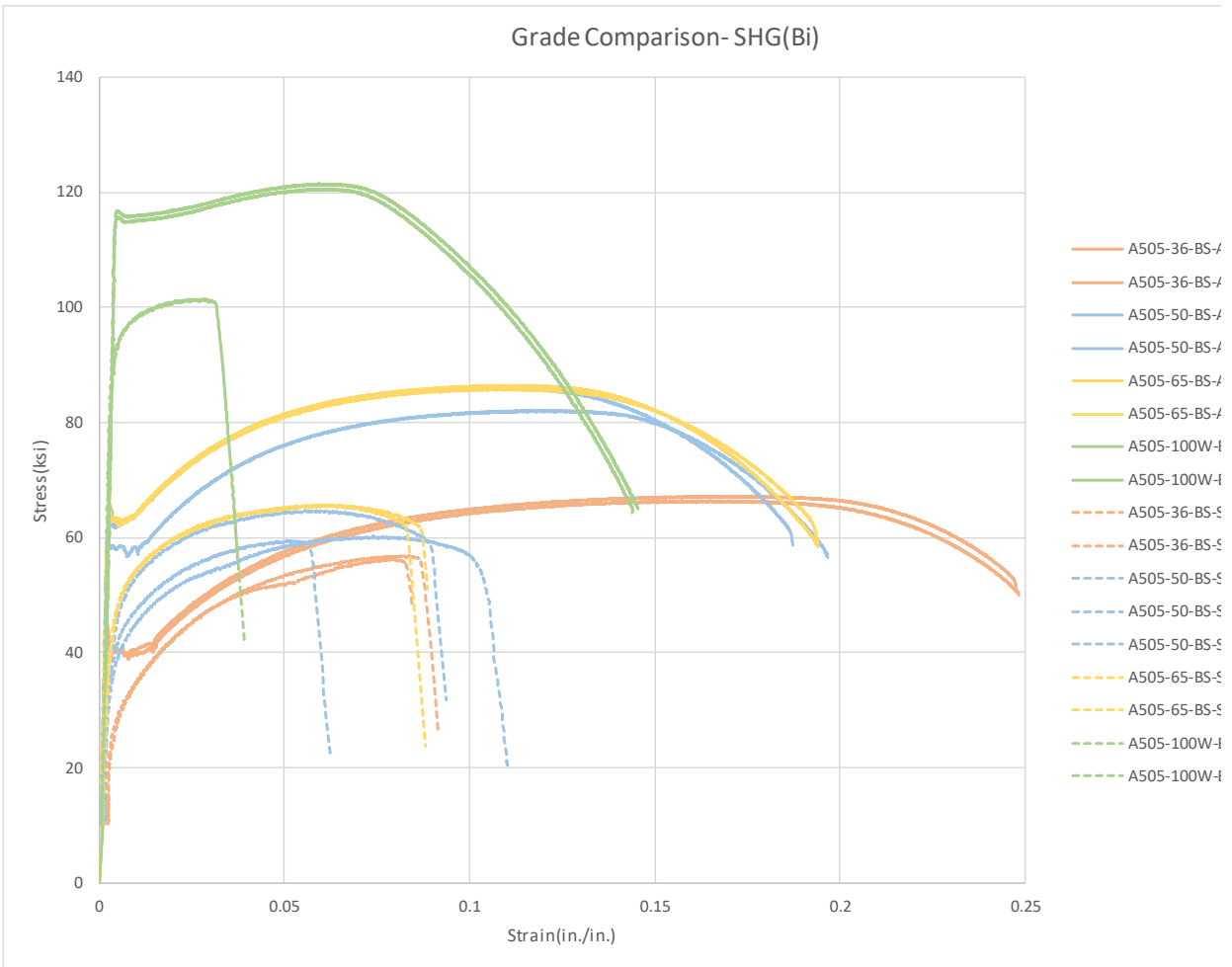


Figure C-2. Effect of SHG zinc + 0.1% Bi on all steel grades.

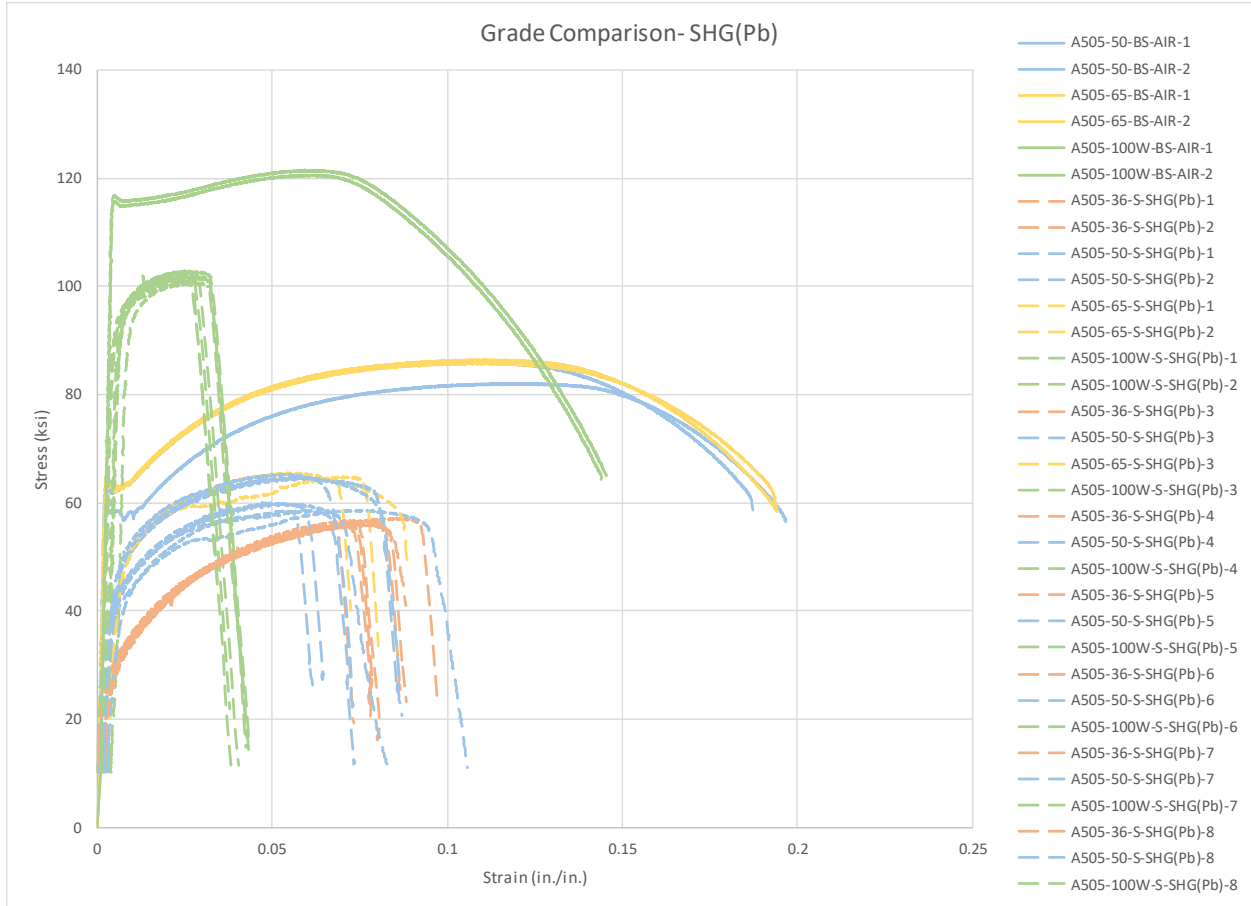


Figure C-3. Effect of SHG zinc + 1% Pb on all steel grades.

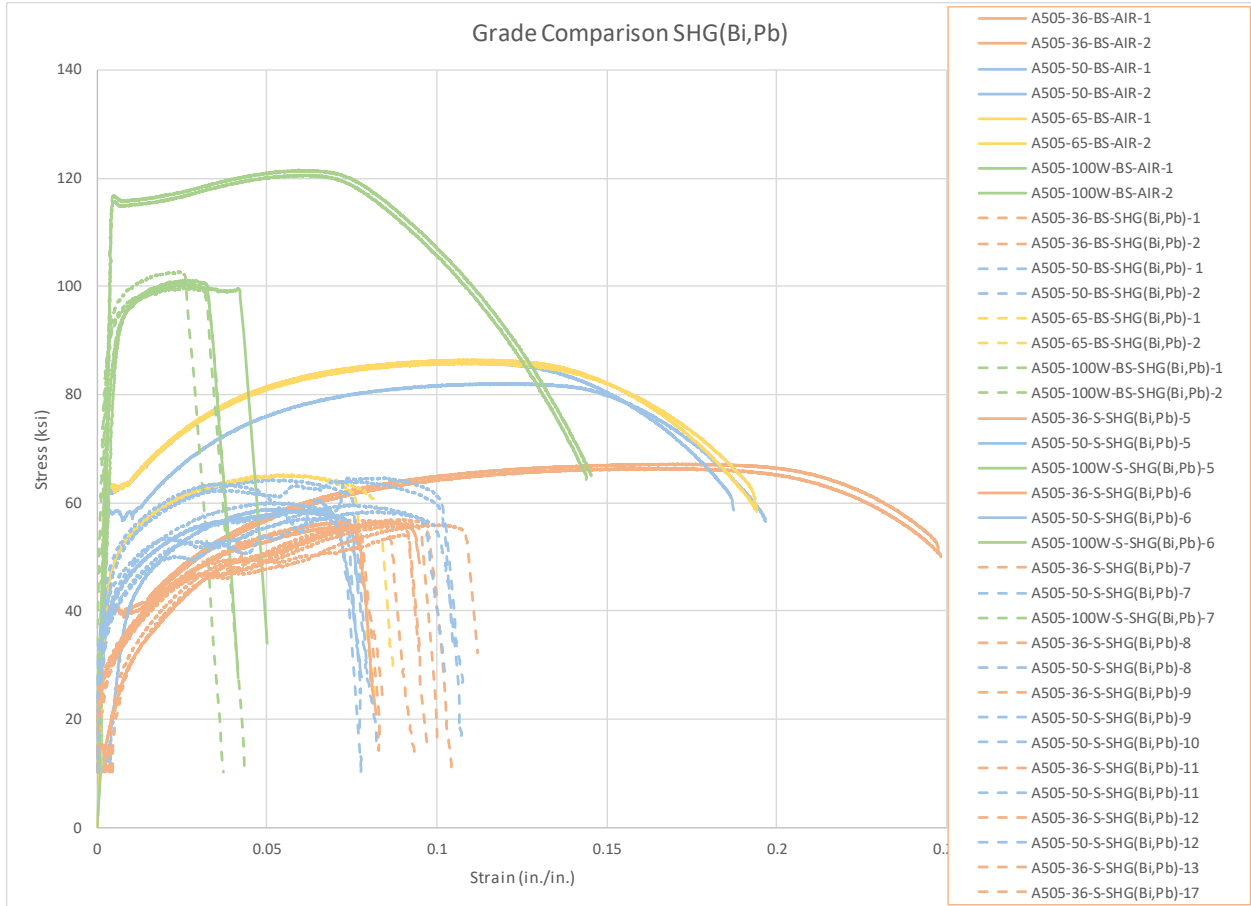


Figure C-4. Effect of SHG zinc + 0.1% Bi+1% Pb on all steel grades.

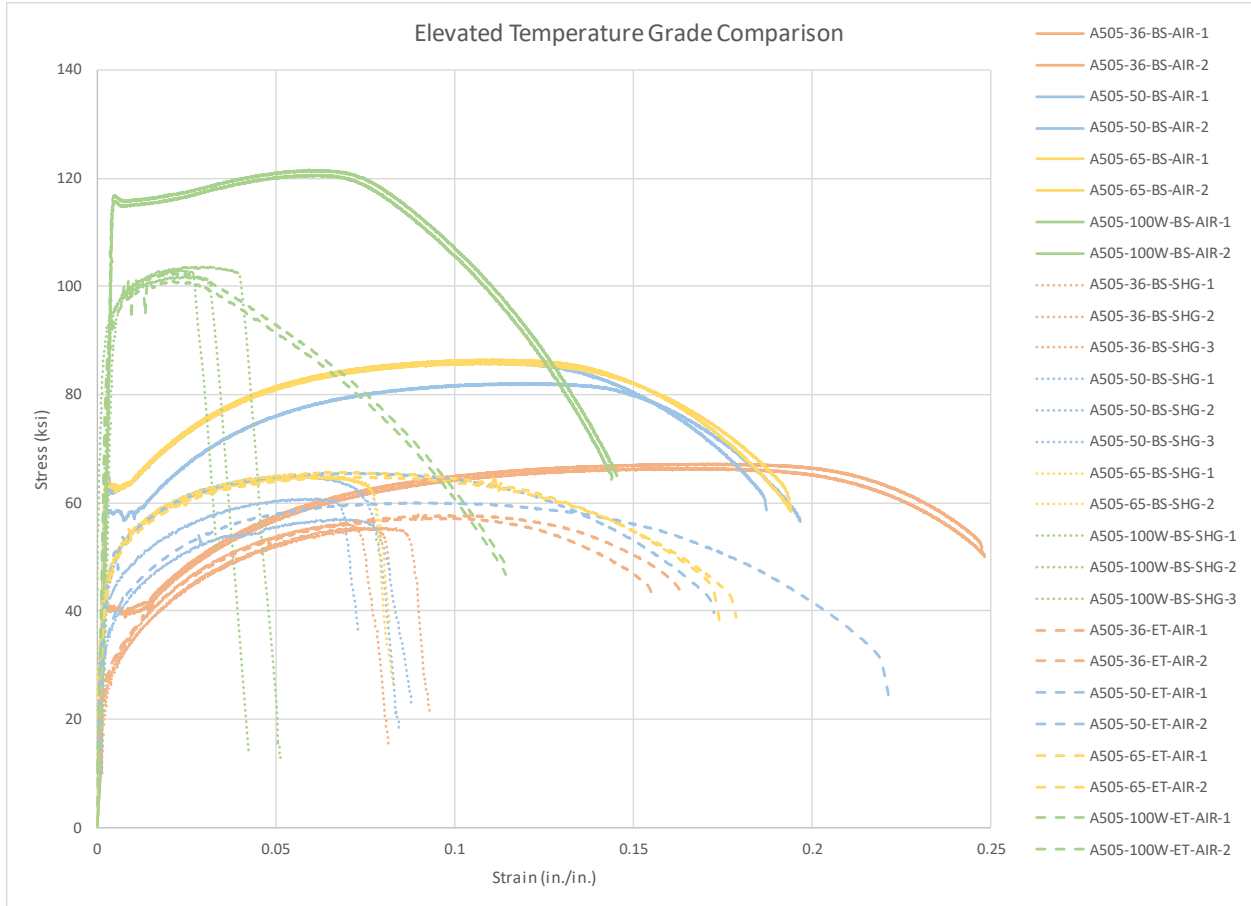


Figure C-5. Effect of elevated temperature on all steel grades.

Subtask 6.2: Stress Concentration

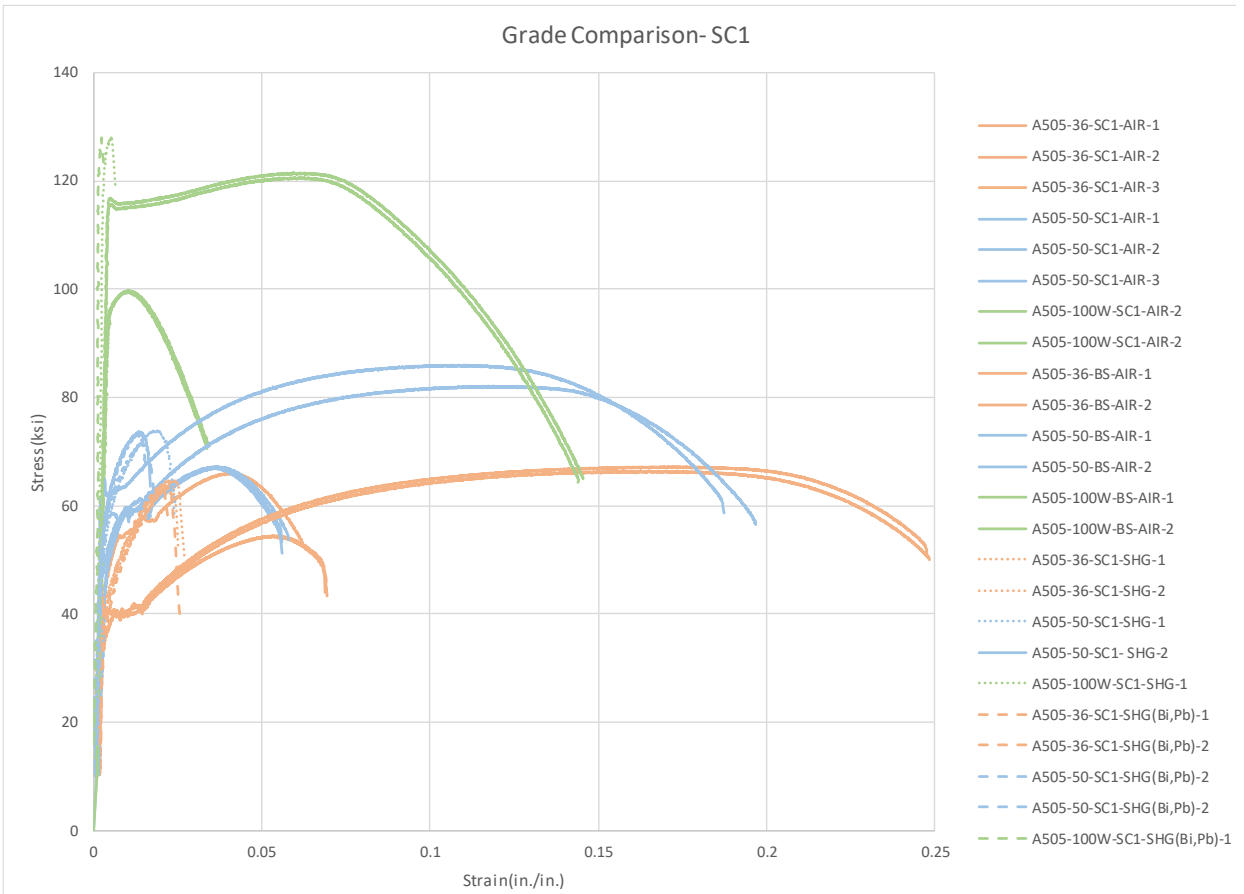


Figure C-6. Effect of Stress Concentration (SCF=1.5) for different steel grades and different zinc chemistries

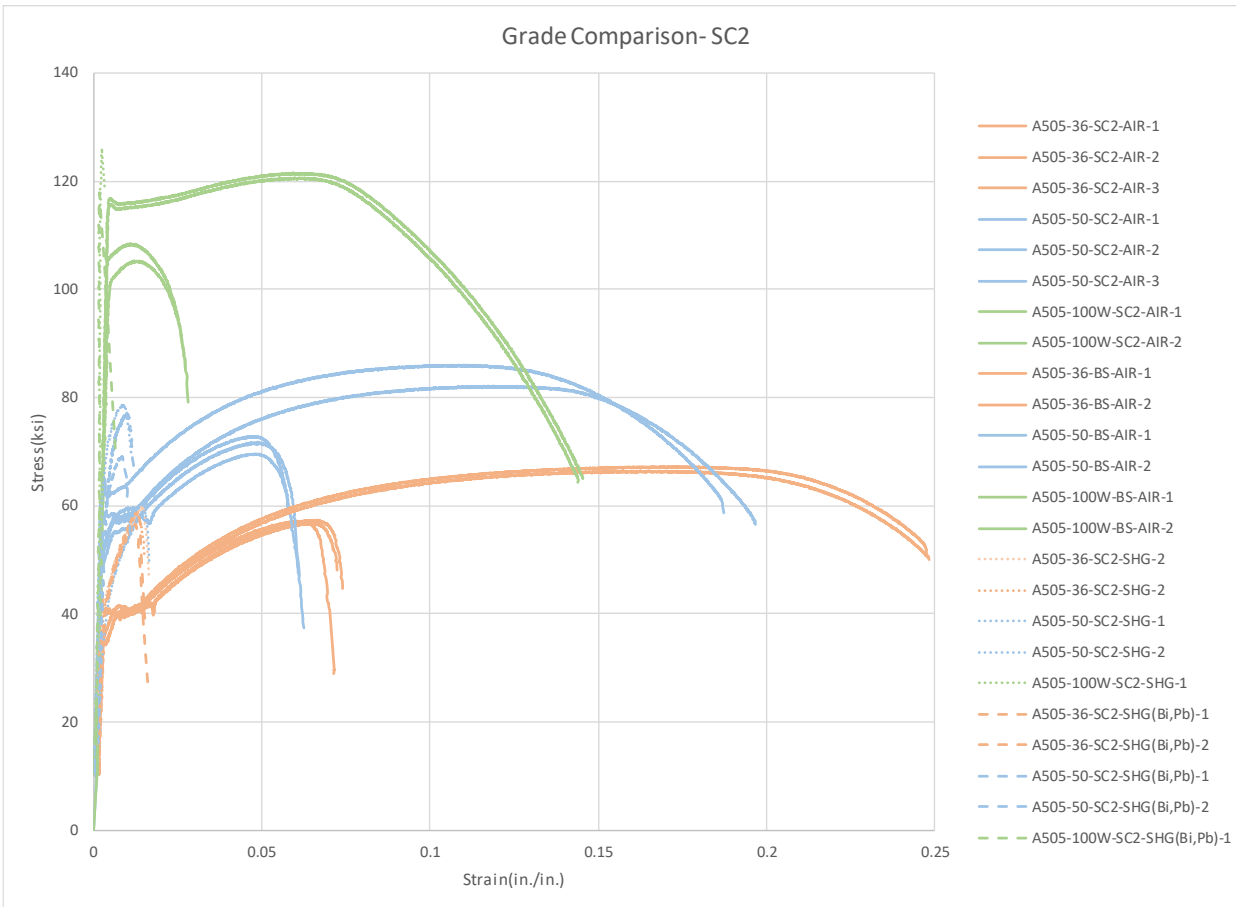


Figure C-7. Effect of Stress Concentration (SCF=2.5) for different steel grades and different zinc chemistries

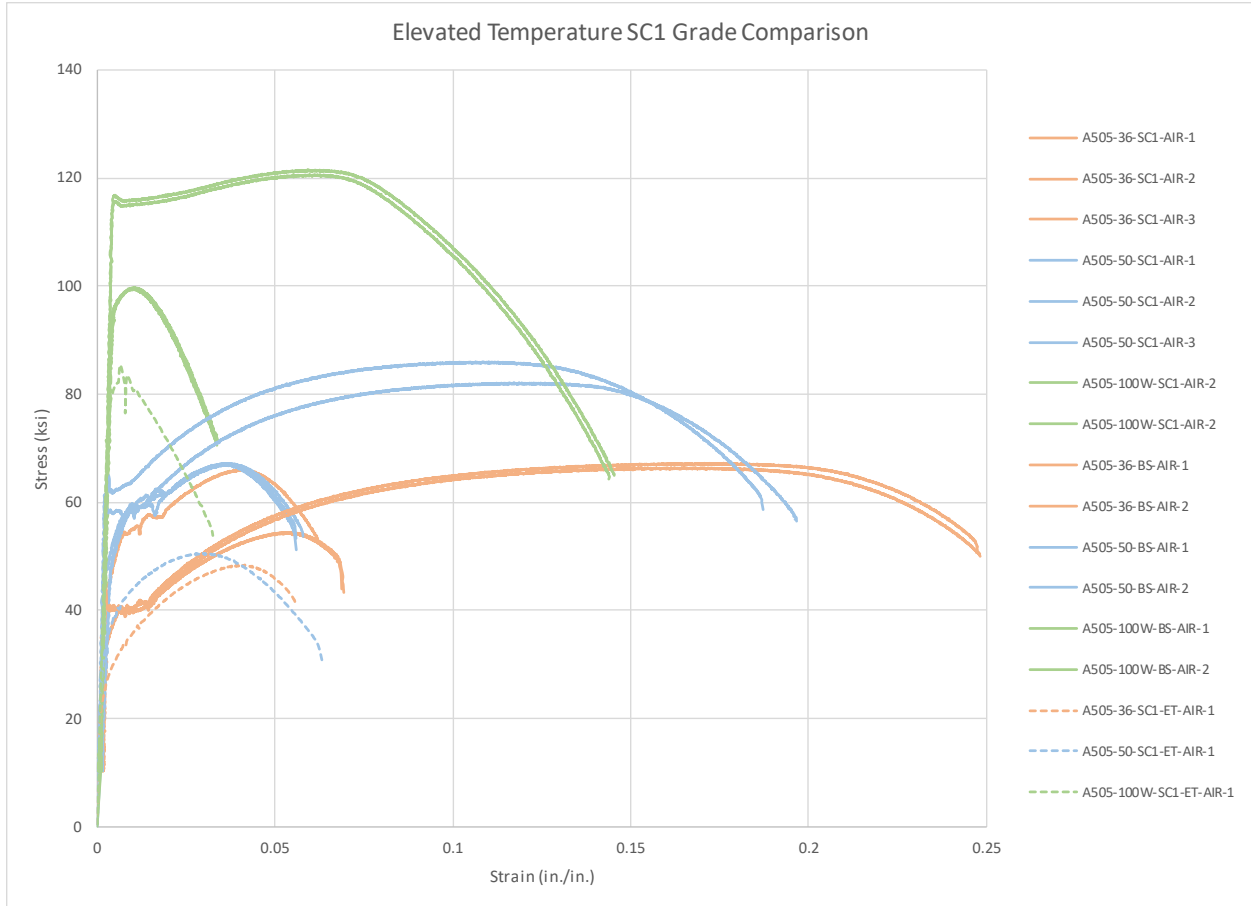


Figure C-8. Effect of Stress Concentration (SCF=1.5) for different steel grades in air at room temperature and at elevated temperature

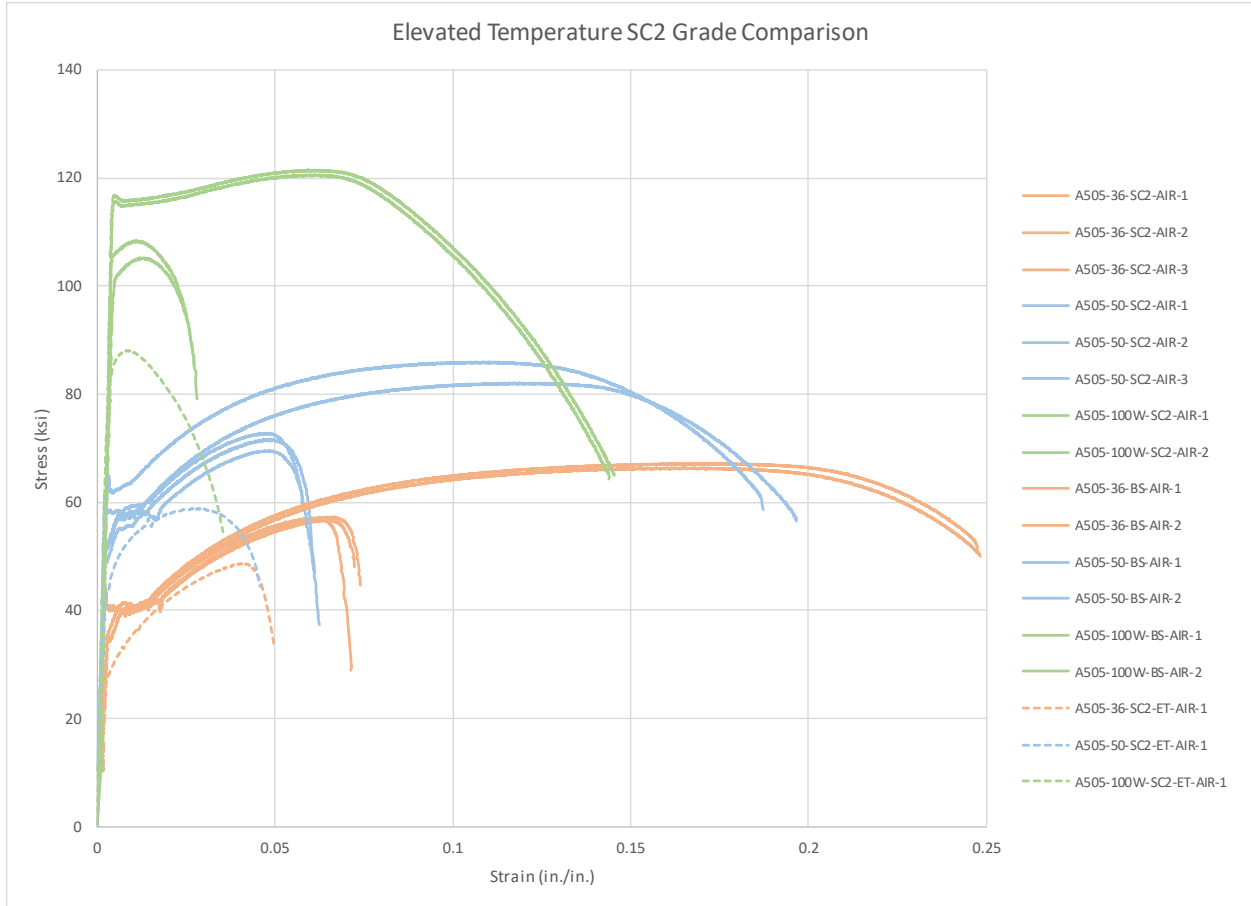


Figure C-9. Effect of Stress Concentration (SCF=2.5) for different steel grades in air at room temperature and at elevated temperature

Subtask 6.3: HAZ Properties

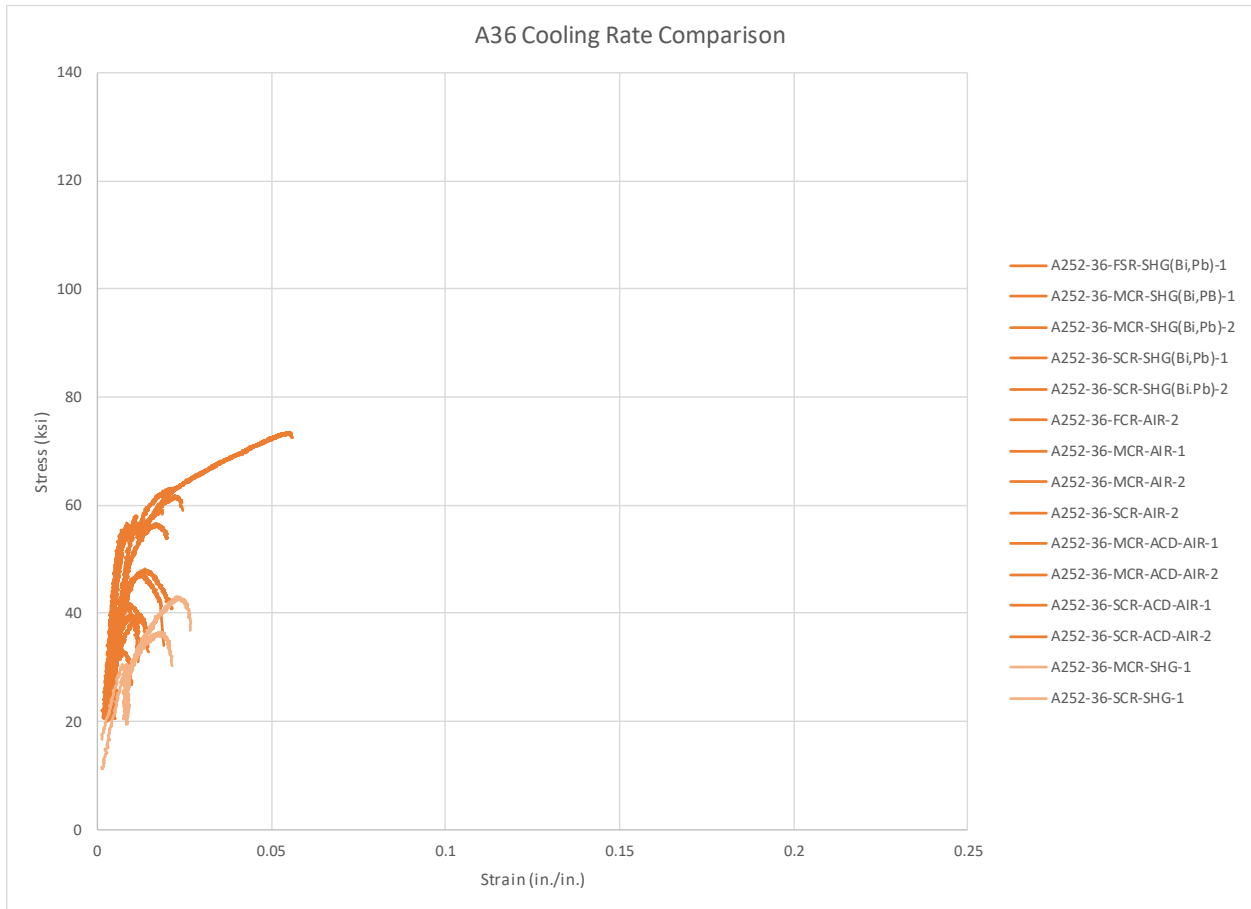


Figure C-10. Effect of cooling rate for A36 steel

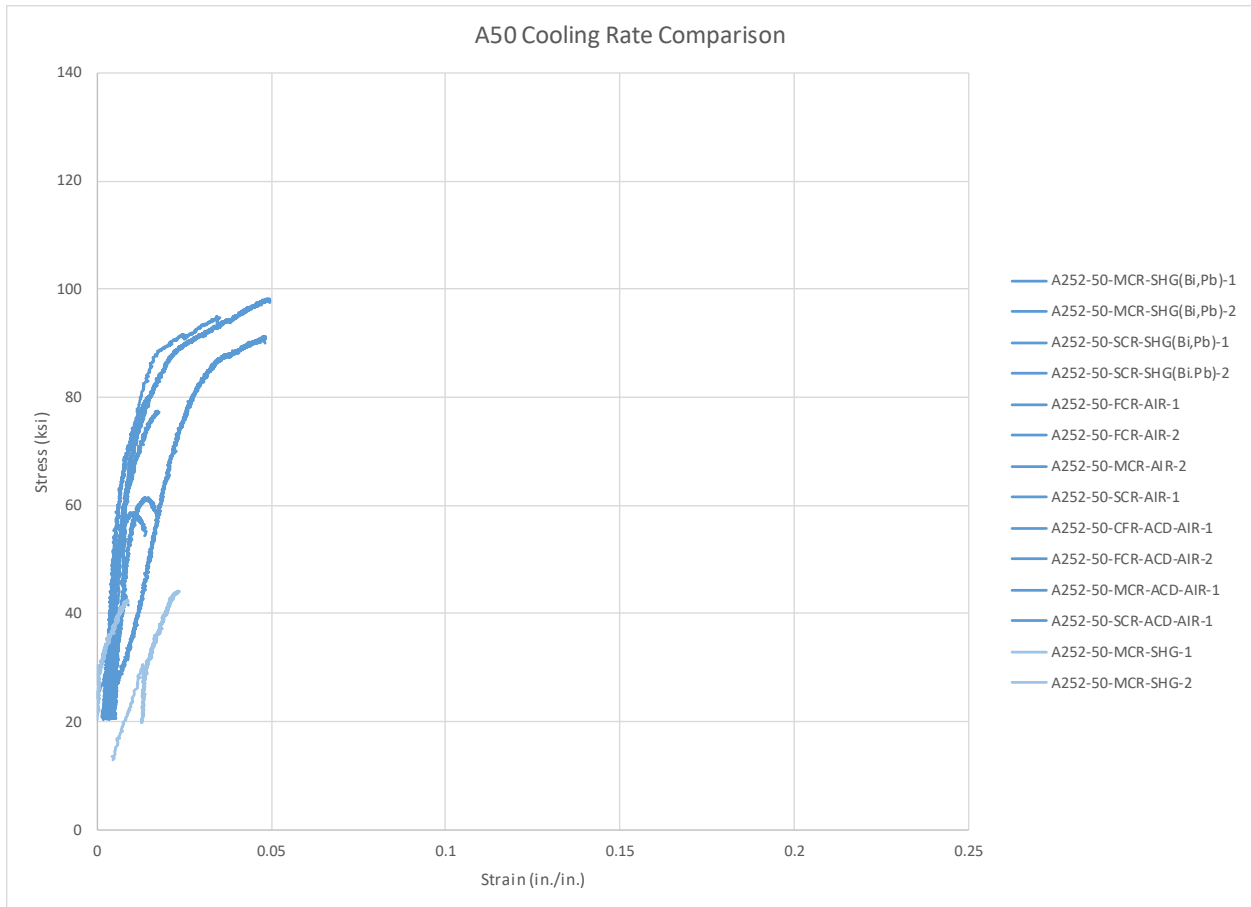


Figure C-11. Effect of cooling rate for A575-50 steel

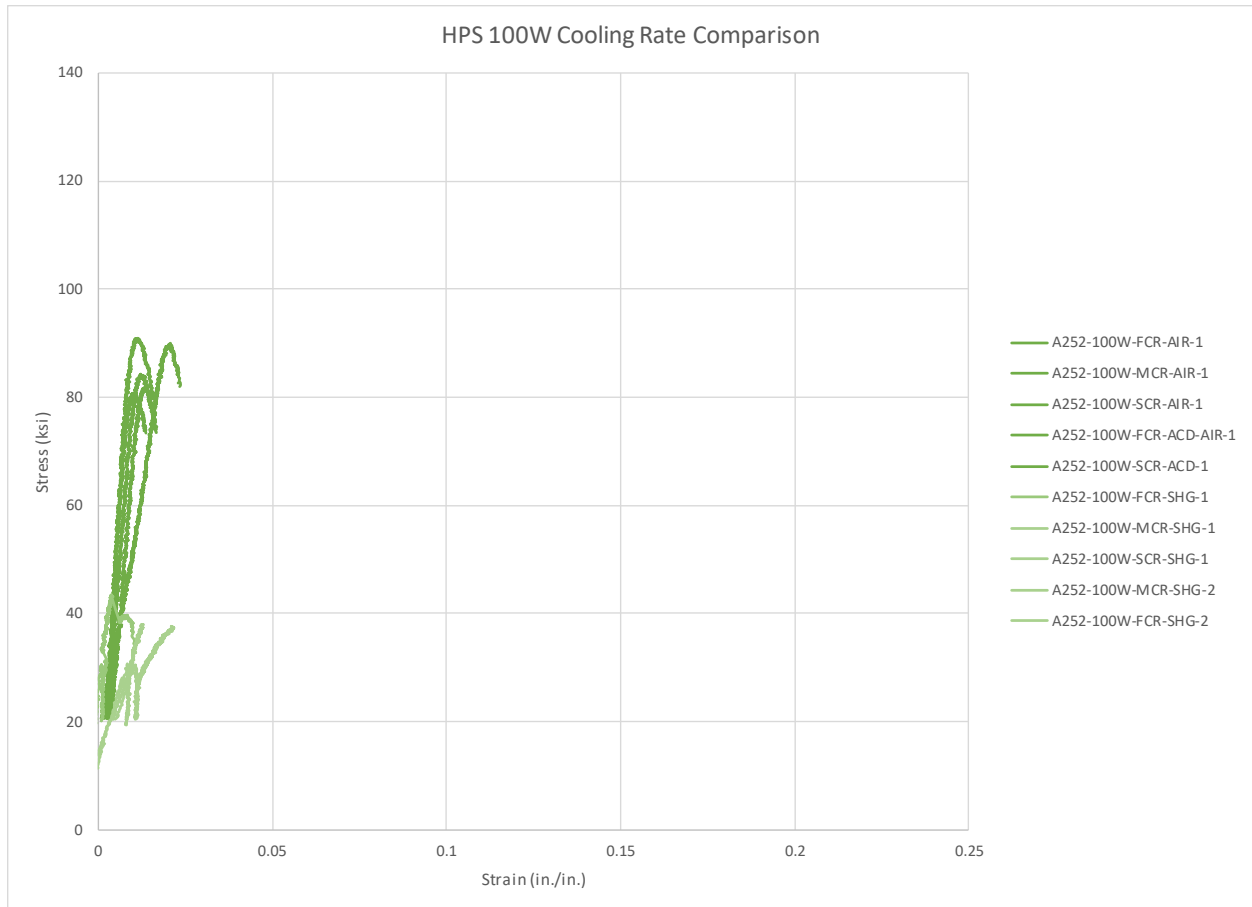


Figure C-12. Effect of cooling rate for HPS100W steel

Subtask 6.4: Cold-Working

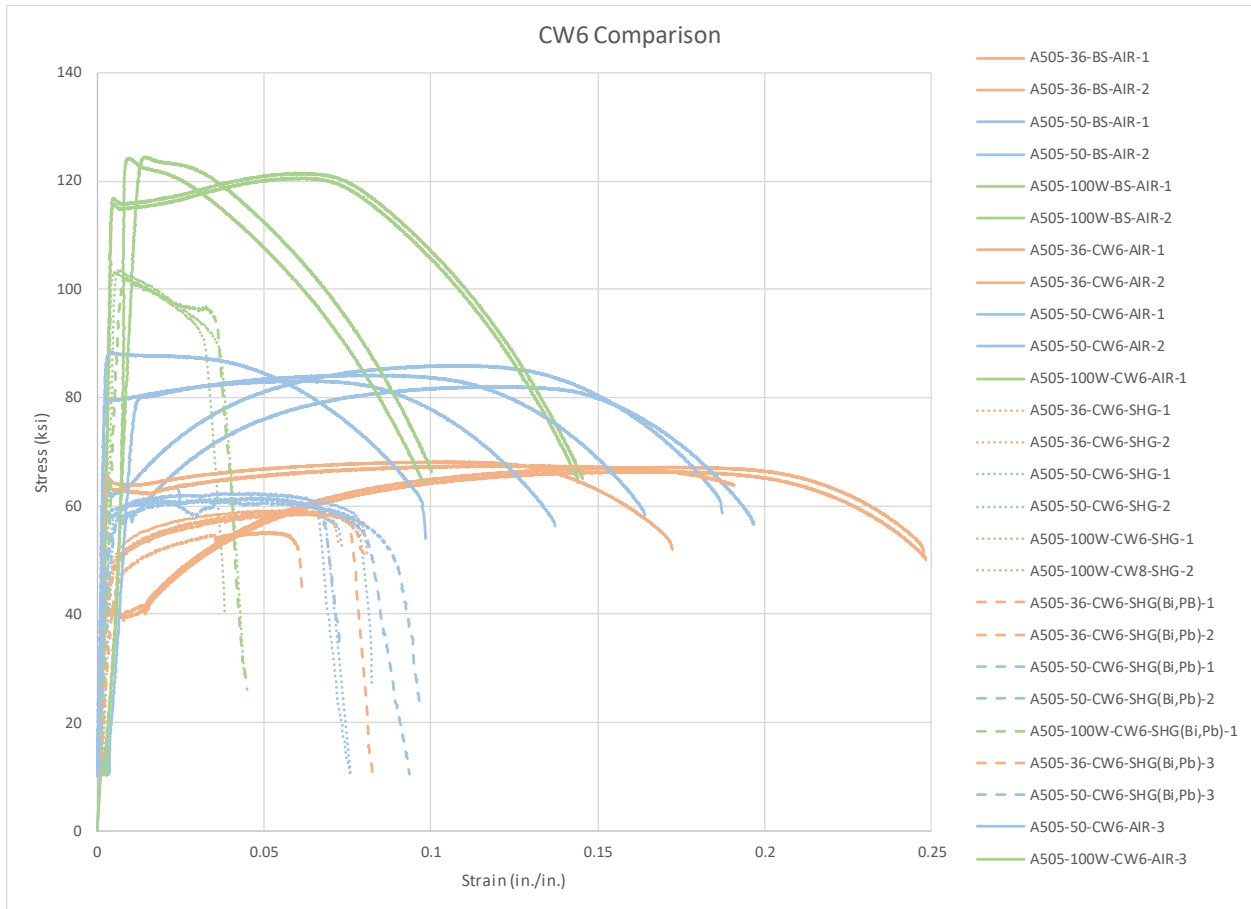


Figure C-13. Effect of cold work (6%) for different steel grades and different zinc chemistries

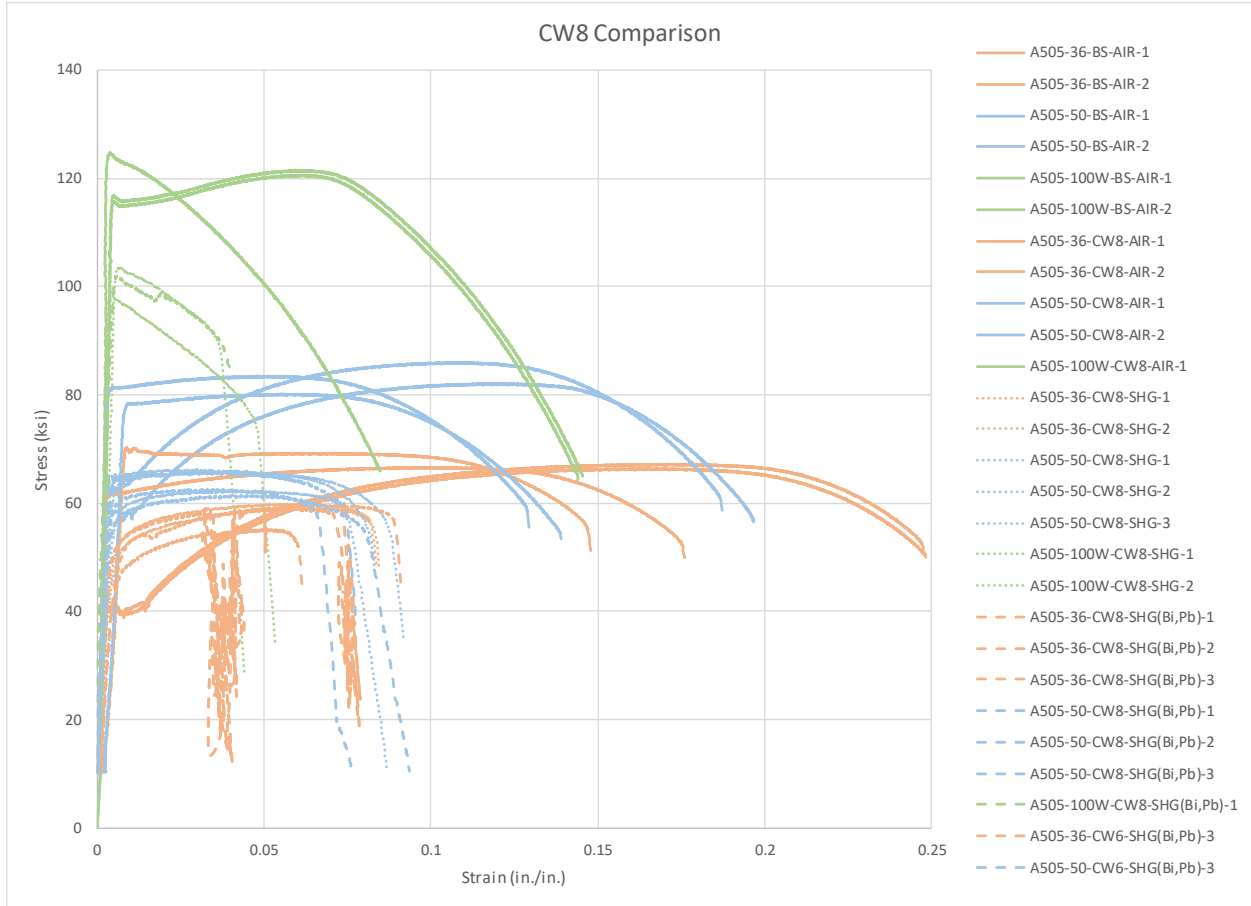


Figure C-14. Effect of cold work (8%) for different steel grades and different zinc chemistries

APPENDIX D

Supporting Results for Computational Simulations

Nonlinear Material Properties

Figure D-1 and Figure D-2 present the nonlinear thermal and nonlinear mechanical material properties used in the computational simulations.

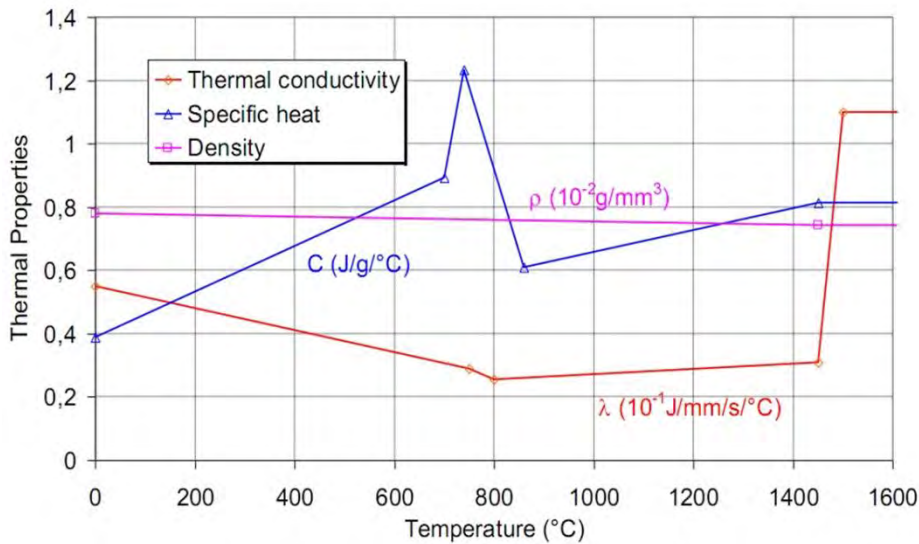


Figure D-1. Thermal material properties used in FE analyses (Peric, 2014).

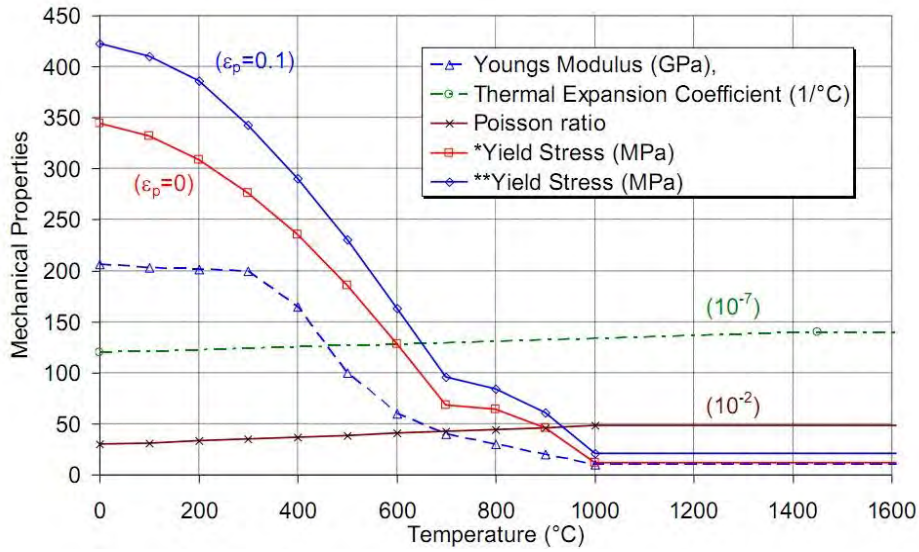


Figure D-2. Mechanical material properties used in FE analyses (Peric, 2014).

Model Calibration

A comparison between measured and calculated temperatures at the base plate of the calibration model is shown in Figure D-3. Solid lines represent model-derived values while dashed lines represent measured values (Kleineck, 2011). Curves with the designation *S* correspond to values at thermocouple locations in the pole shaft, while curves with the designation *BP* correspond to values at thermocouple locations in the base plate. Figure D-3 shows that the combination of parameters used in this study closely replicated temperatures measured by Kleineck (2011), indicating a well-calibrated model.

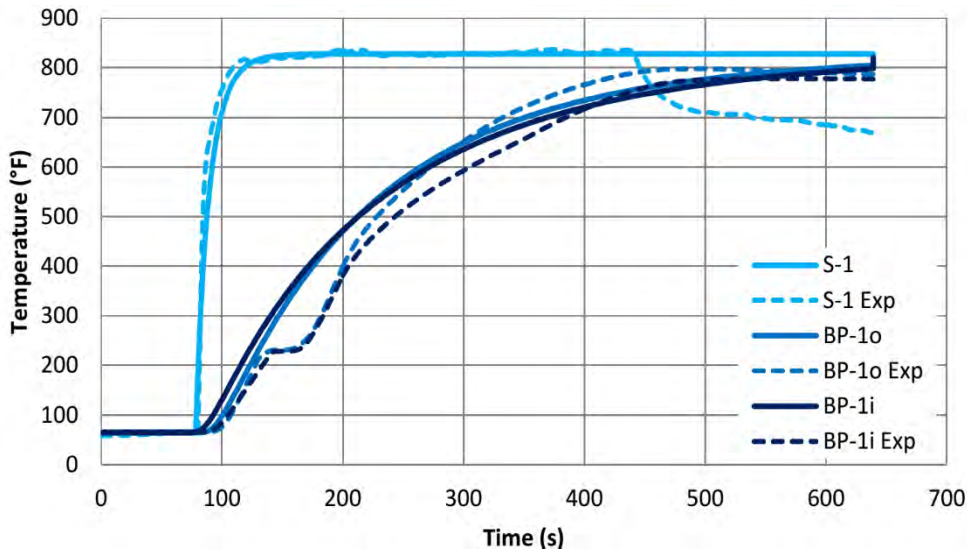


Figure D-3. Comparison between HMIP FE and temperature measurements by Kleineck (2011)

General Behavior of HMIPs During Galvanization

Deformed shapes for a pole assembly at different stages of the galvanizing cycle are presented in Figure D-4 and Figure D-5. The figures show the overall deformation and temperature fields, where red represents the temperature of the galvanizing bath and blue represents ambient temperature. The figures also show deformations at a cross-section at the base of the pole assembly for round, eight-sided, and 12-sided cross sections. In the cross-sections, the colors represent von Mises stresses, where red represents a stress value near yield and blue represents a stress value near zero.

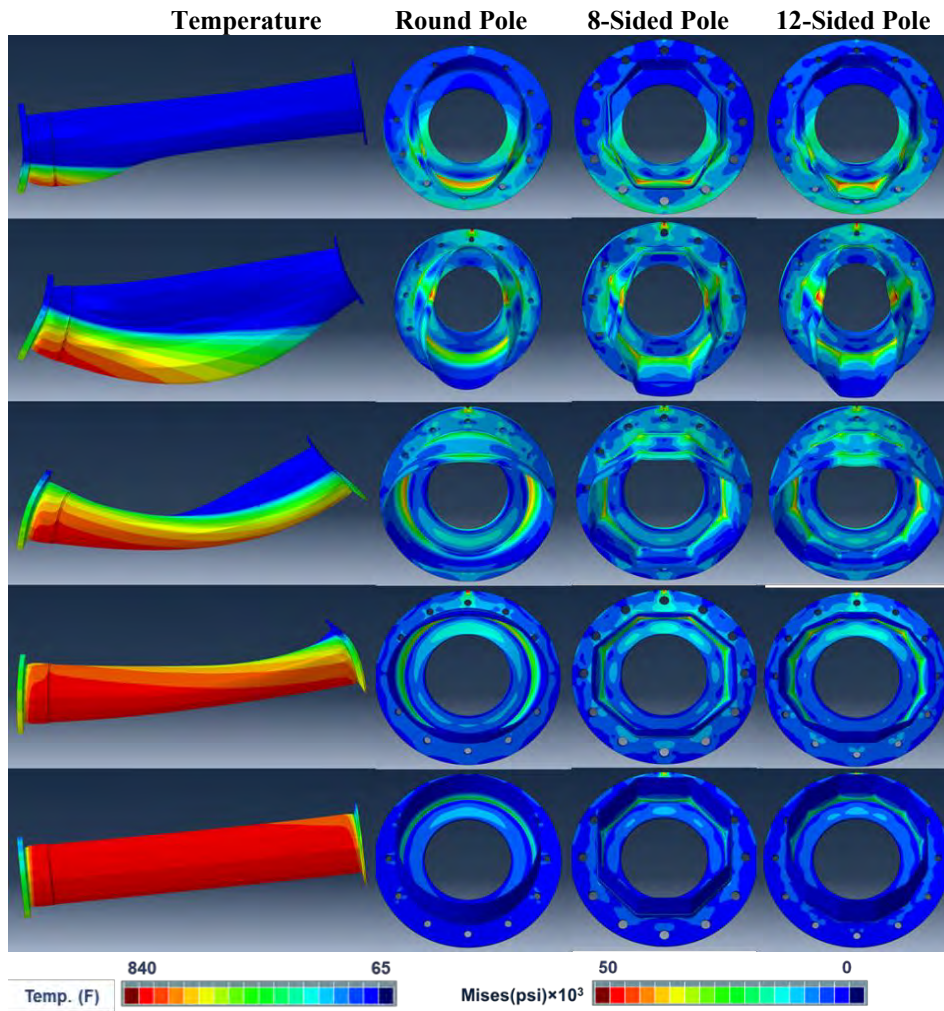


Figure D-4. Deformed shapes, temperatures, and stress demands during immersion.

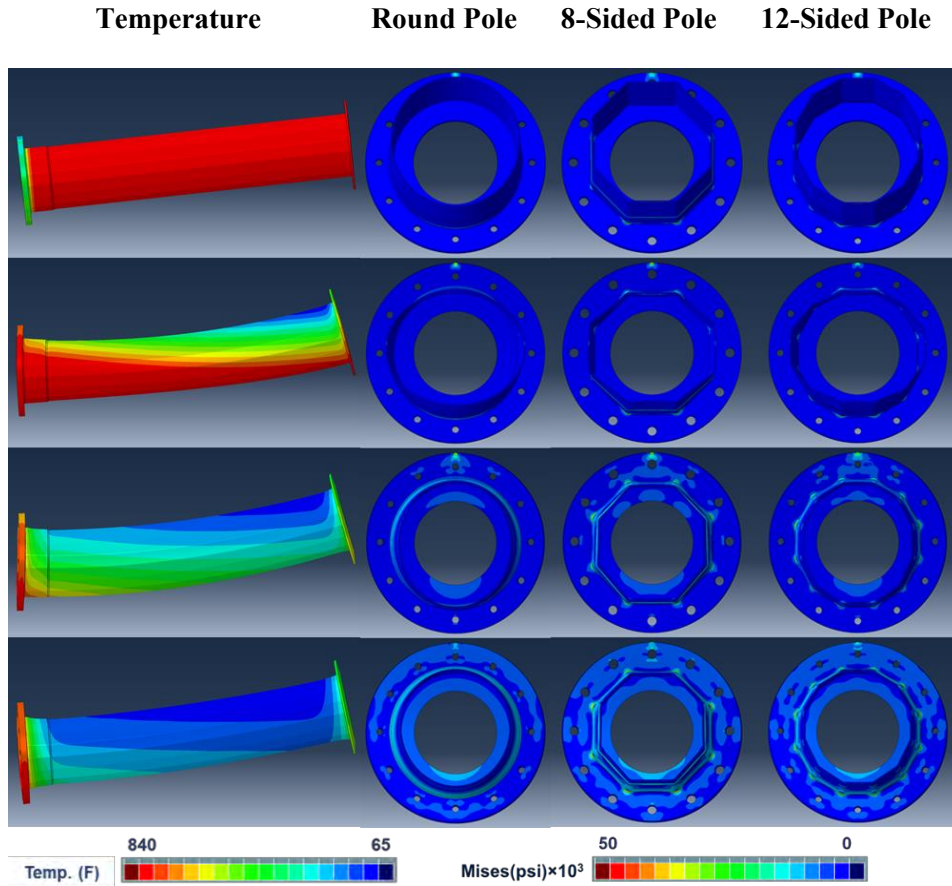


Figure D-5. Deformed shapes, temperature, and stress demands during dueling and extraction.

Data Extraction and Analysis

A sample path used for data extraction in one of the 12-sided models is shown in Figure D-6. A sample plot showing the temperature at each node along that path is shown in Figure D-7. Curves in Figure D-7 were plotted using a color map associated with time, where green lines depict the temperature along the path at the start of the simulation and dark lines show the temperature at the end of the simulation. Data sets like this enabled identification of the time and location in which peak responses occurred, which were different for different poles. Multiple paths were analyzed over the height of the pole, starting near the weld, to ensure that any changes in the location of the peak over the height of the assembly were considered in the comparisons between response quantities for different poles.

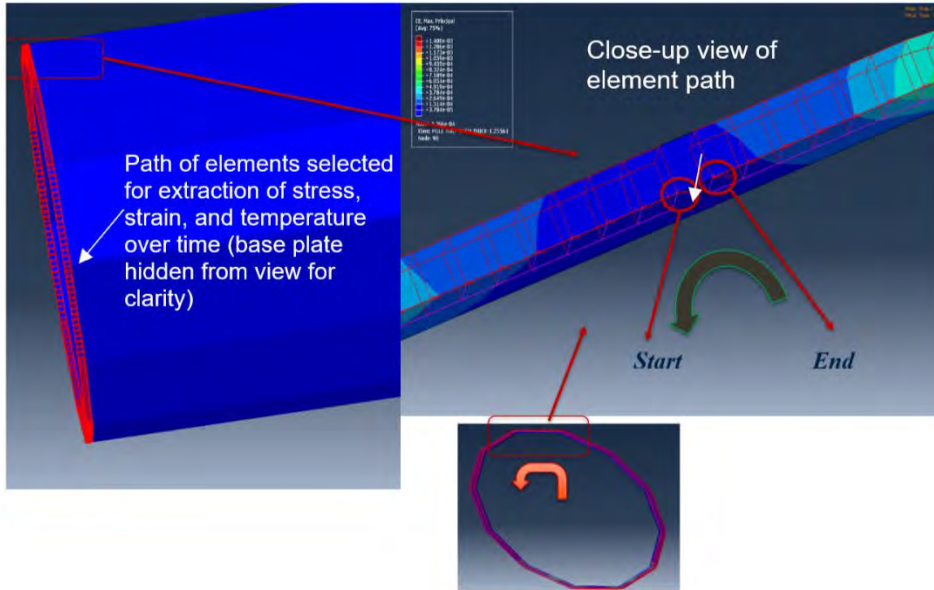


Figure D-6. Path along which data were extracted along the perimeter of the pole, near the baseplate

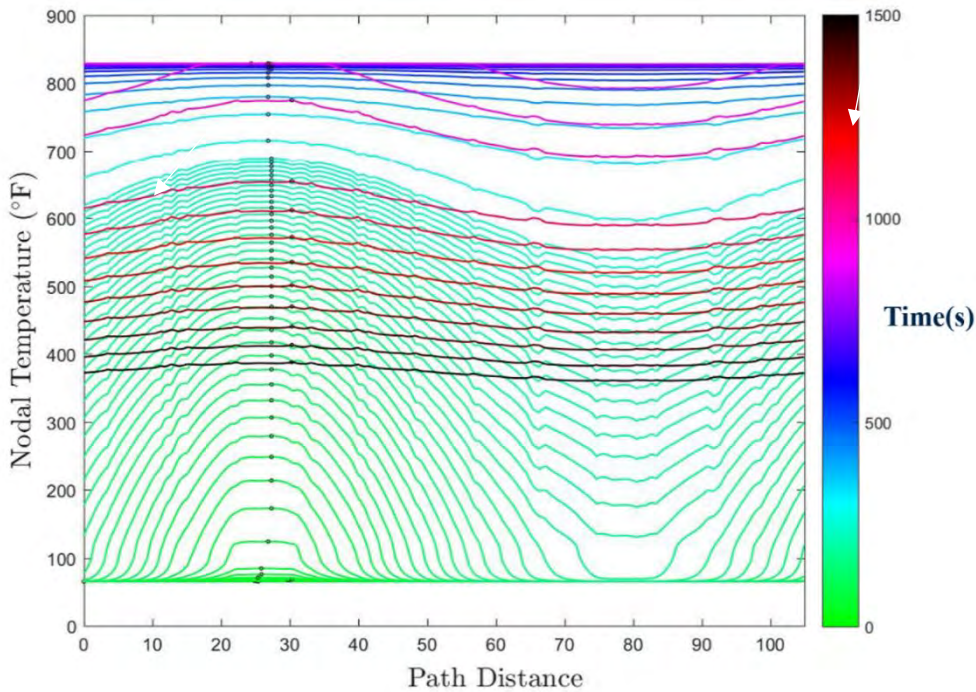


Figure D-7. Plot showing the variation of temperature along the path shown in , as a function of time.

Stress Demands at the Pole-to-Base Plate Connection

To illustrate the pattern of stress demands at the pole-to-base plate connection of multi-sided poles, maximum principal stresses for a 5/16 in. thick pole shaft with a 2 in. thick base plate are shown in Figure D-8 and Figure D-9. Figure D-8 shows stress demands during immersion in the zinc bath, which ended at $t=180$ sec, and dwelling, which ended at $t=480$ sec. Figure D-9 shows stress demands during cooling, which

started at $t=840$ sec. Similar results for a 5/16 in. thick pole shaft with a 3 in. thick base plate are shown in Figure D-10 and Figure D-11. Each of these figures shows clearly the influence of the stress concentrations at the bends of multisided poles. During the immersion stage, stress demands were greatest at the bends near the surface of the zinc bath. As the pole is continually immersed, temperature at the pole shaft and base plate equilibrates in the regions of the assembly that are most deeply immersed. The last row of images in Figure D-8 corresponds to the end plate being completely submerged during the dwelling stage. Figure D-8 also shows that high stresses remained at pole bends, and that those stresses progressively subsided as the base plate slowly reached the temperature of the bath.

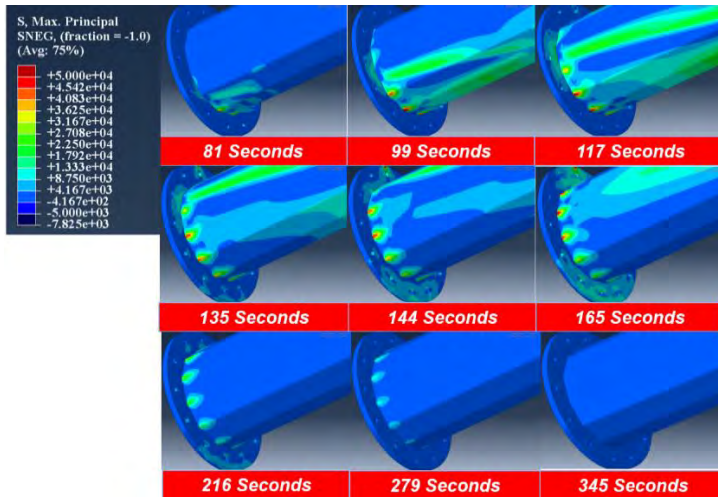


Figure D-8. Stress demands during immersion and dwelling stages for model with 2 in. base plate and 5/16 in. thick pole

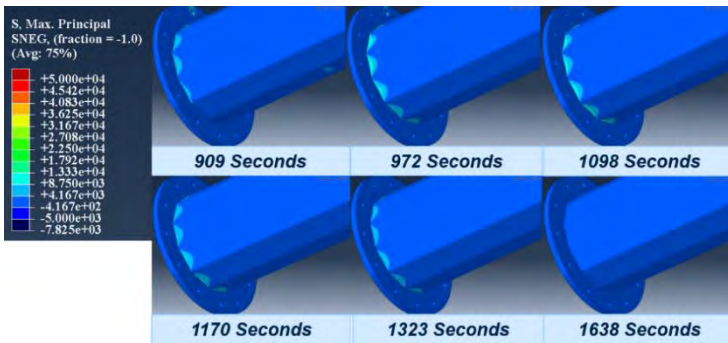


Figure D-9. Stress demands cooling stage for model with 2 in. base plate and 5/16 in. thick pole

Stress demands during the cooling stage were greatest soon after the pole was completely extracted from the bath, and slowly decreased as the temperature of the base plate asymptotically tended towards ambient temperature. During the cooling stage large stress demands were observed only at pole bends, near the connection with the base plate (Figure D-9).

Figure D-10 and Figure D-11 show that computed stresses exhibited a similar trend for all multi-sided pole configurations, and that for assemblies with the same pole thickness, stress demands increased with base plate thickness.

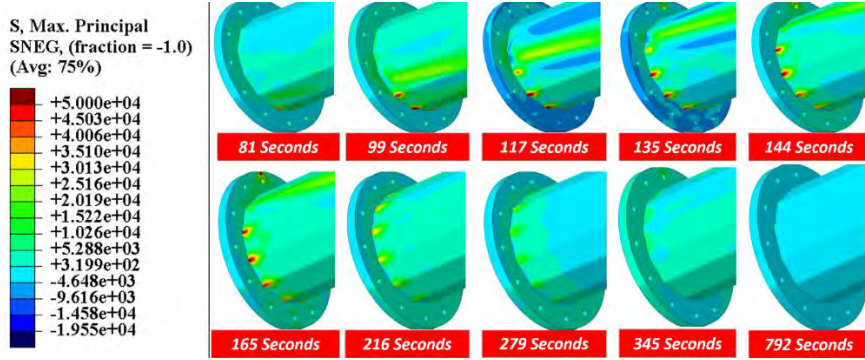


Figure D-10. Stress demands during immersion, dwelling, and cooling stages for model with 3 in. base plate and 5/16 in. thick pole.

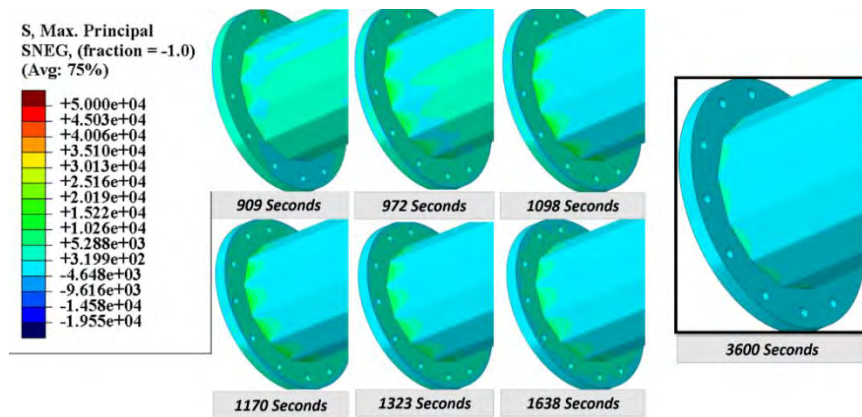


Figure D-11. Stress demands during cooling stage for model with 3 in. base plate and 5/16 in. thick pole.

Variation of Stress and Strain Demands with Respect to Time and Location

The type of data analysis described in the previous section was performed to determine maximum stress and strain demands in each of the 18 models of the parametric study, to establish an objective basis of comparison between poles with different configurations. Detailed results showing demand variations at specific pole locations with respect to time and location are explored in detail here, for a set of 12-sided poles with Wyoming DOT pole-to-base plate connection and a shaft thickness of 5/16 in. The only parameter that was varied in this particular set was base plate thickness, which ranged between 1.5-3.5 in. in increments of 0.5 in. Figure D-12 shows model configurations included in the set, and Figure D-13 shows the numbering scheme used to designate the pole bends throughout the study. Numbering started at the bend nearest the top middle of the pole (12 o'clock position) and increased in the clockwise direction. In this comparison, demands were extracted from a circumferential path around the pole at a distance one element from the weld toe. Given the symmetry of the HMIP, results are presented for Bend 7 and Bend 10, where calculated demands were the largest.

The temporal variations of stress during galvanizing at elements located near bends 7 and 10 are shown in Figure D-14 and Figure D-15. Figure D-14 shows time histories for von Mises stress at an element near Bend 7, at the bottom of the pole, for the five HMIP models in the set. Peak values before $t=100$ (dipping stage ended at $t=180$ sec) corresponded to the time when the surface of the bath met the steel at bend 7. At this location, von Mises stress demands were highest during the dipping stage, although slightly lower than the yield stress for steel at room temperature. Because temperature changes very rapidly in the pole as it

meets the zinc bath, the increase in stress was almost instantaneous, followed by a rapid drop as the surrounding area reaches the bath temperature.

The rapid increase and decrease in stress showcase the complexity of the coupled thermal-mechanical simulation, which adjusts the yield stress of the steel due to changes in temperature. As a reference, values reported by Peric (2014) indicate that the yield stress of steel at the galvanizing bath temperature is on the order of 60% of the yield stress at room temperature (Peric, 2014). These rapid changes in yield point highlight the main limitation of stress metrics, which make it difficult to determine whether the material deformed inelastically because the scale saturates at the yield point, and because the yield point is sensitive to temperature variations within the range evaluated in this study. At peak response, stress demand in the pole for the model with a plate thickness of 1.5 in. was lower than all the other models, which had a peak demand of approximately 45 ksi. Stress demands during the dwelling and extraction stages, which ended at $t = 480$ sec and $t = 840$ sec respectively, were gradual in nature and increased with base plate thickness.

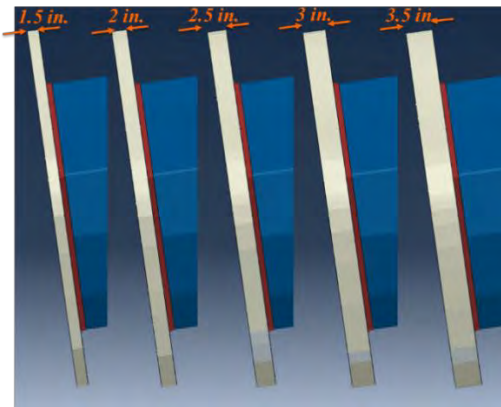


Figure D-12. HMIP models used in demand comparisons shown in Figures 5-17 to 5-24.

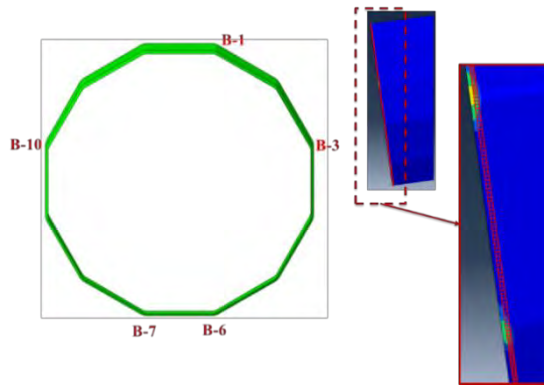


Figure D-13. Bend numbering of 12-sided poles and element paths for stress/strain extraction

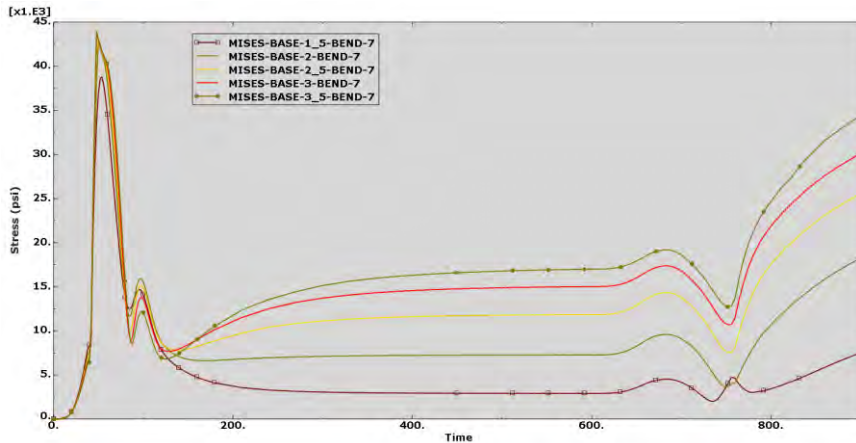


Figure D-14. Von Mises stress near Bend 7

Von Mises stress demands at Bend 10, near mid-height of the pole in the position it was galvanized, are shown in Figure D-15. Peak stress demands near Bend 10 were higher than those calculated near Bend 7, located near the bottom of the pole. This trend was consistent throughout the study, where bends near the mid-height position (Bends 3 and 10 for 12-sided poles) experienced the greatest demands. During the dipping stage all models experienced the same peak demand at Bend 10, approximately equal to the yield stress of the steel. This was different than at Bend 7, where the model with the 1.5 in. thick base plate had a lesser peak demand than all the others. During extraction, stress demands were proportional to base plate

thickness, following a similar trend to those in Bend 7, although peak demands at Bend 10 were lower than those calculated at Bend 7.

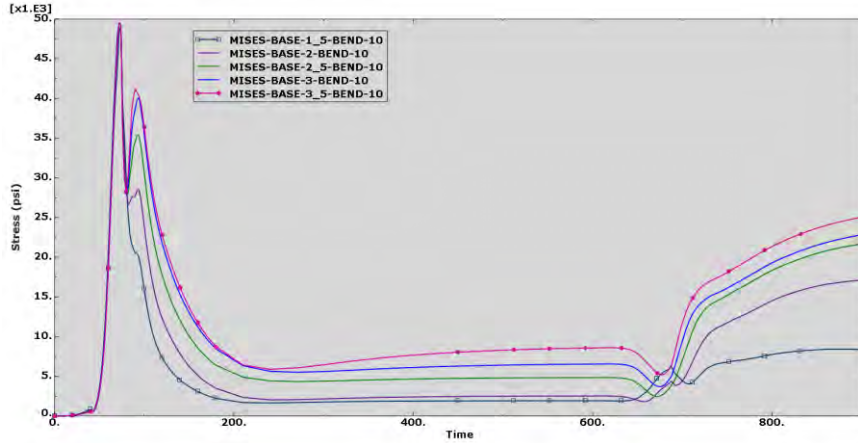


Figure D-15. Von Mises stress near Bend 10

Figure D-16 shows maximum principal stress demands at Bend 10. These values are reported to provide a comparison with von Mises stress demands because both can be used as indicators of damage potential. Maximum principal stress demands were higher than von Mises stress demands during the dipping stage, and had a single peak at approximately the same time as peak response was calculated for von Mises stress demands. Although the magnitude of maximum principal stresses were different than the von Mises stresses, demands consistently increased with plate thickness for both metrics during dwelling and extraction.

Figure D-17 shows the distribution of von Mises stress in the region of the pole-to-base plate connection for the five HMIP models in the set at $t=74$ seconds. This corresponded approximately to the time during the dipping stage when Bend 10 came into contact with the zinc bath, and the maximum stress demands were calculated at that location. The yellow band in Figure D-17 corresponds approximately to the surface of the zinc bath. These findings corroborate that stress demands increased with plate thickness, and shows that the region of the pole subjected to peak stresses extended further into the pole as base plate thickness increased.

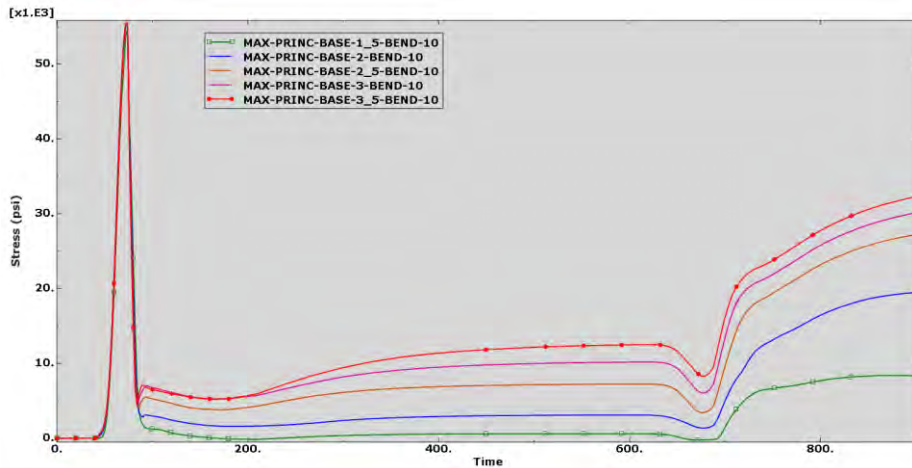


Figure D-16 Single element Maximum Principal Stress Results at Bend 10

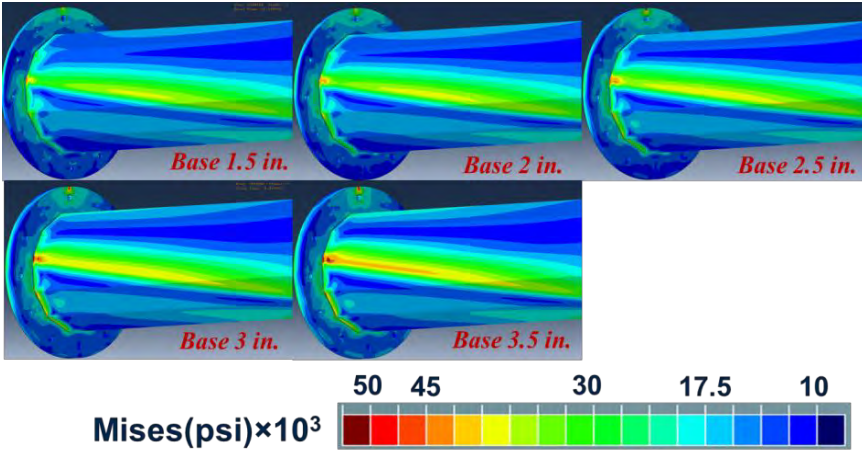


Figure D-17. von Mises Stresses at $t=74$ s during the dipping stage, when peak stresses occurred at Bend 10.

While stress metrics are useful because they are relatable from an engineering perspective, they are of limited use as damage indicators because their scales saturate at the yield point. This is not the case for strain metrics, which provide a measure of deformation in the nonlinear range of response which increases directly proportional to damage. In this report, strain results are presented in terms of equivalent plastic strain (PEEQ), also referred to as accumulated plastic strain, which is defined as:

$$\bar{\epsilon}^{pl} \Big|_0 + \int_0^t \dot{\bar{\epsilon}}^{pl} dt \tag{Equation D-1}$$

where $\bar{\epsilon}^{pl} \Big|_0$ is the initial equivalent plastic strain. The rate evolution component, $\dot{\bar{\epsilon}}^{pl}$, is calculated as

$$\dot{\bar{\epsilon}}^{pl} = \sqrt{\frac{2}{3} \dot{\epsilon}^{pl} \dot{\epsilon}^{pl}} \tag{Equation D-2}$$

The rate of change of plastic strain $\dot{\epsilon}^{pl}$ is squared when solved from Eq. D-2 so the sign is not relevant and both tensile and compressive plastic strains contribute to the total accumulated plastic strain. Because PEEQ accumulates over time, it can be used to show the sections of the HMIP that experience the most damage, which may lead to crack initiation. The strain energy density in an elastic-plastic material, W , is dependent on the von Mises stress and PEEQ as follows:

$$W = \frac{1 - 2\nu}{6E} \sigma_{kk} + \frac{1 + \nu}{3E} \sigma_{VM} + \sigma_{VM} \epsilon^{pl} \tag{Equation D-3}$$

where σ_{VM} is the von Mises effective stress, $\dot{\epsilon}^{pl}$ is the plastic strain rate, and ϵ^{pl} is the PEEQ. In fracture mechanics approaches, the strain energy density W is used in the J -integral to calculate the energy release rate G , and crack growth initiates when the energy release rate reaches a critical value G_c . Thus, von Mises and PEEQ are related to the energy release rate and likely good indicators of locations with the highest potential for crack initiation.

Figure D-18 and Figure D-19 show PEEQ values along the pre-defined path at the end of the simulation for the five HMIP models. Figure D-18 shows that PEEQ strains were highly concentrated at bend locations, and that nonlinear deformations were nearly zero between peaks. The location of the bends with the highest demands was not consistent. In the two models with the largest base plate thickness, $t = 3.0$ in. and $t = 3.5$ in., the largest inelastic strains occurred at Bends 6 and 7, at the bottom of the pole, followed by Bends 3 and 10, near the center of the pole. In models with base plate thickness $t = 2.5$ in. and thinner, the largest

inelastic strain demands occurred at Bends 3 and 10, near the center of the pole, and decreased with proximity to the bottom of the pole. In all models, peak strain demands at Bends 1 and 12, near the top of the pole, were the lowest of all.

Figure D-18 also shows that peak inelastic strain was directly proportional to base plate thickness, regardless of bend location of peak strain demand. For example, the HMIP model with the largest base plate thickness of the set ($t = 3.5$ in.) had the largest PEEQ demand of approximately $2200 \mu\epsilon$ at Bends 6 and 7. In contrast, the HMIP model with the smallest base plate thickness of the set ($t = 1.5$ in.) had the smallest PEEQ demand, less than $600 \mu\epsilon$ at Bends 3 and 10. This trend is evident in Figure D-19, which shows the PEEQ for the five models at the end of each analysis. Inelastic strains were localized near the bends, and the region affected by inelastic deformations increased with plate thickness.

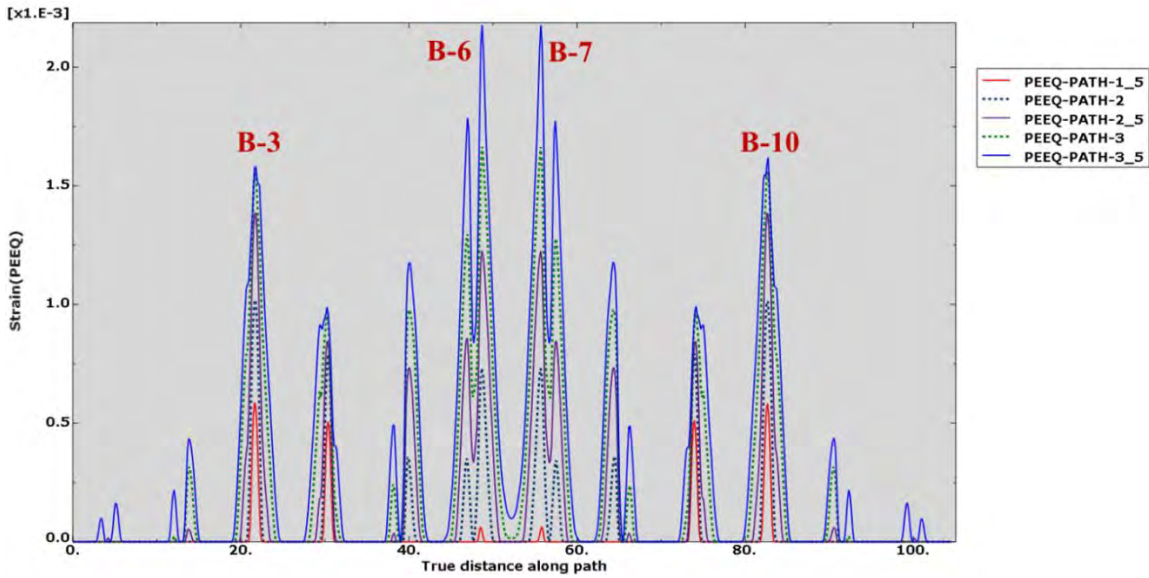


Figure D-18. PEEQ along the defined path for the five models

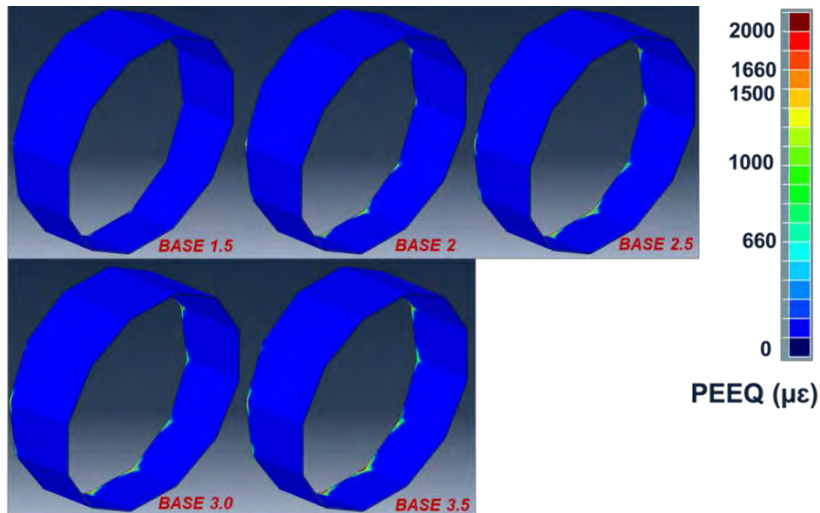


Figure D-19. Equivalent plastic strain (PEEQ) for the five models at the end of analysis (final condition)

Behavior of Round Poles

Figure D-20 and Figure D-21 show calculated stress demands during different stages of the galvanizing process for round pole Models 3 and 19, both with a 3 in. thick base plate and pole thicknesses of 5/16 in. and 1/2 in., respectively.

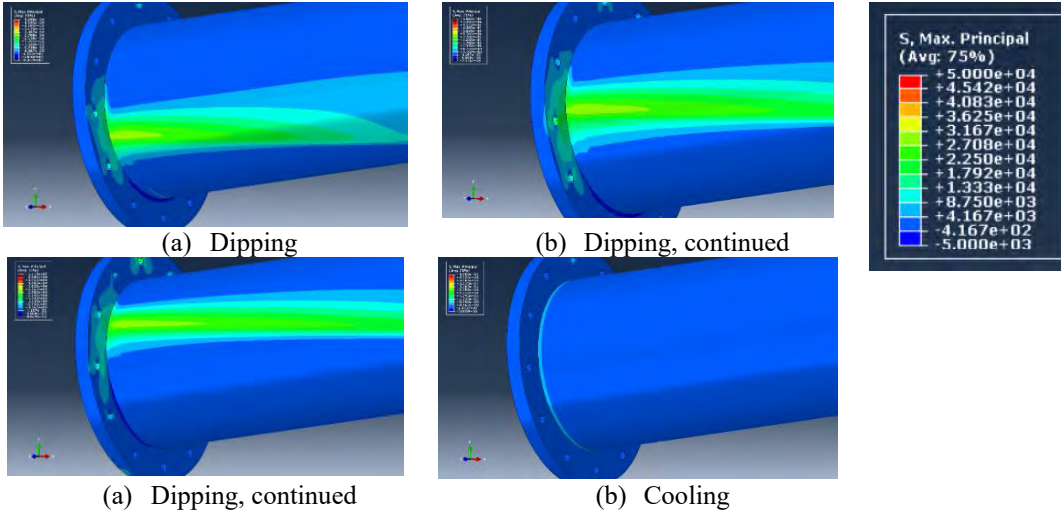


Figure D-20. Stress demands for Model 3, a round pole with $t = 5/16$ in., and 3 in. thick baseplate.

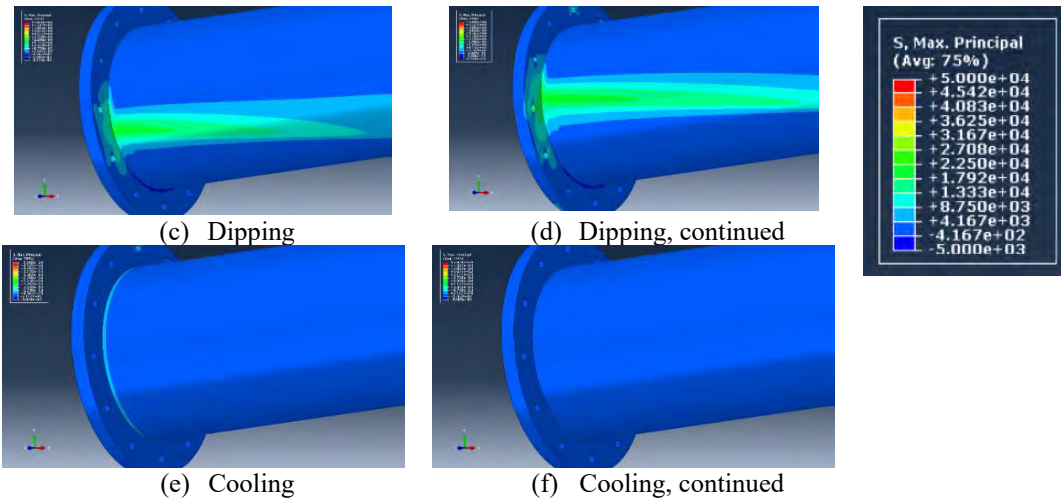


Figure D-21. Stress demands for Model 19, round pole with $t = 1/2$ in., and 3 in. thick baseplate.

Effect of Number of Sides, Poles Thickness, and Base Plate Thickness on Stress and Inelastic Strain Demands

Figure D-22 through Figure D-27 show the stress fields for models of eight-, 10-, and 12-sided poles with pole thicknesses of 5/16 in. and 1/2 in. All models represented in these figures had a base plate thickness of 3 in. A visual comparison shows that the stress demands were higher for 5/16 in. thick poles than they were for the corresponding 1/2 in. thick pole with the same number of sides.

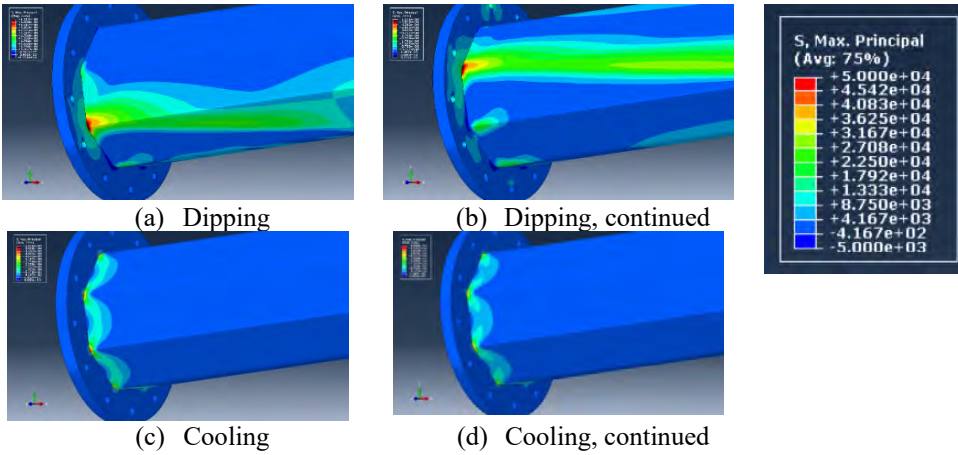


Figure D-22. Calculated stress demands for Model 4, 8-sided pole, 5/16 in. thick, and 3 in. thick baseplate.

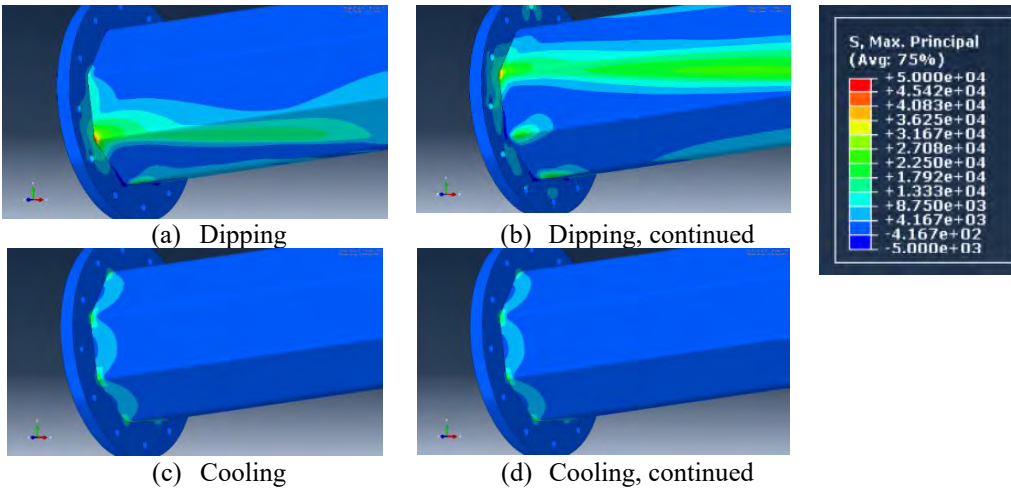


Figure D-23. Calculated stress demands for Model 7, 8-sided pole, 1/2 in. thick, and 3 in. thick baseplate.

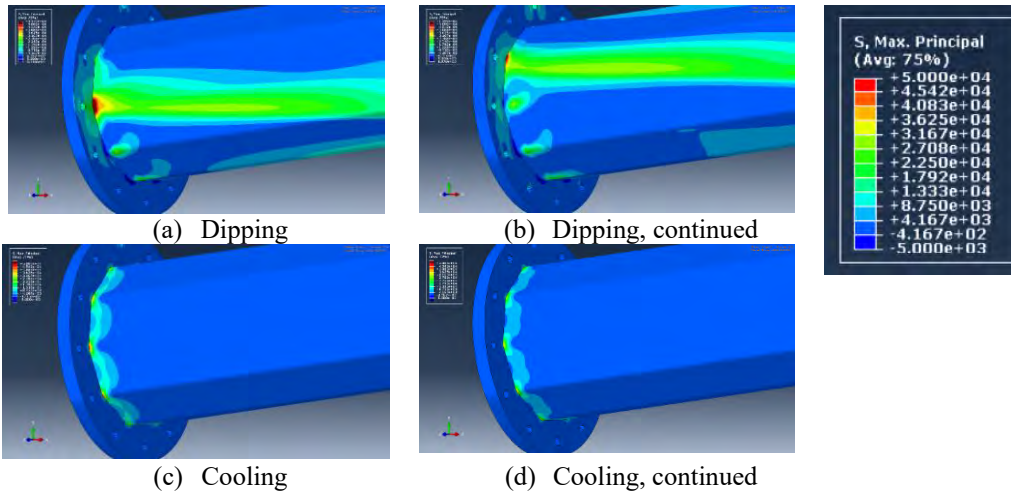


Figure D-24. Calculated stress demands for Model 5, 10-sided pole, 5/16 in. thick, and 3 in. thick baseplate.

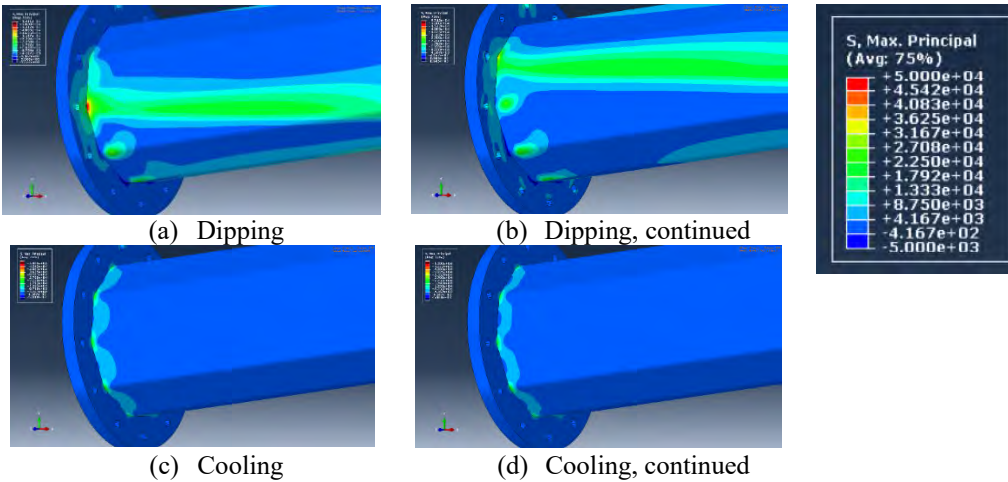


Figure D-25. Calculated stress demands for Model 8, 10-sided pole, 1/2 in. thick, and 3 in. thick baseplate.

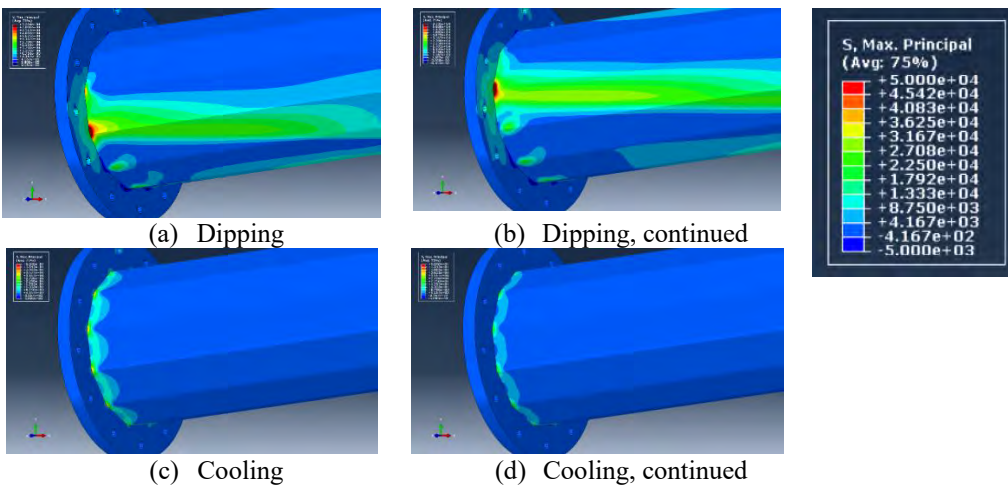


Figure D-26. Calculated stress demands for Model 2, 10-sided pole, 5/16 in. thick, and 3 in. thick baseplate.

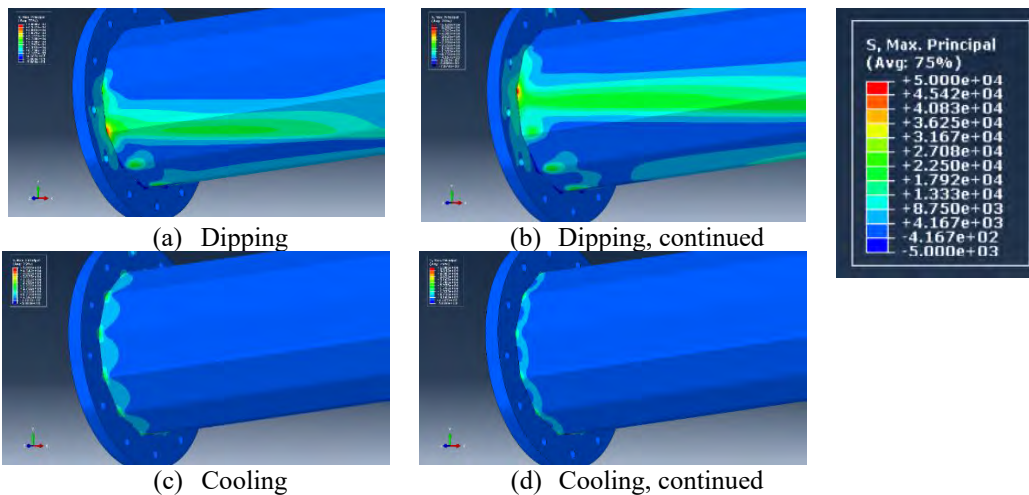


Figure D-27. Calculated stress demands for Model 1, 12-sided pole, 1/2 in. thick, and 3 in. thick baseplate.

Inelastic strain demands are presented in Figure D-28, Figure D-29, and Figure D-30 showing maximum PEEQ at the conclusion of each simulations. All multisided poles represented in Figure D-28 had a thickness of 5/16 in. and base plate thickness of 3 in.; multisided poles represented in Figure D-29 had a thickness of 1/2 in.; and models in Figure D-30 represented both pole thicknesses in a round geometry.



(a) Eight-sided

(b) 10-sided

(c) 12-sided

Figure D-28. Effect of number of sides on HMIP inelastic strain demands (PEEQ). Pole thickness=5/16 in. and base plate thickness=3 in.

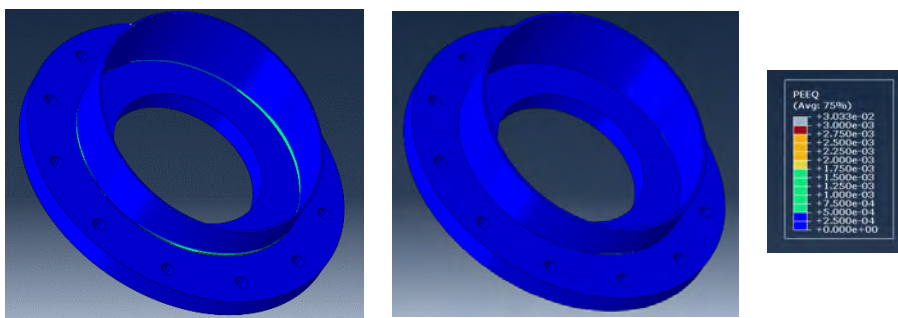


(a) Eight-sided

(b) 10-sided

(c) 12-sided

Figure D-29. Effect of number of sides on HMIP inelastic strain demands (PEEQ). Pole thickness=1/2 in. and base plate thickness=3 in.



(a) 5/16 in. thick pole

(b) 1/2 in. thick pole

Figure D-30. Inelastic strain demands (PEEQ) in round poles. Plate thickness of 3 in.

Figure D-31 through Figure D-35 show computed stress fields for models of 12-sided poles with a thickness of 5/16 in. and base plate thickness ranging between 1 and 3.5 in. These figures show that stress

demands increased with plate thickness, in particular at the time when the level of the zinc bath reached Bend 10. The effect of plate thickness was also noticeable during the cooling stage.

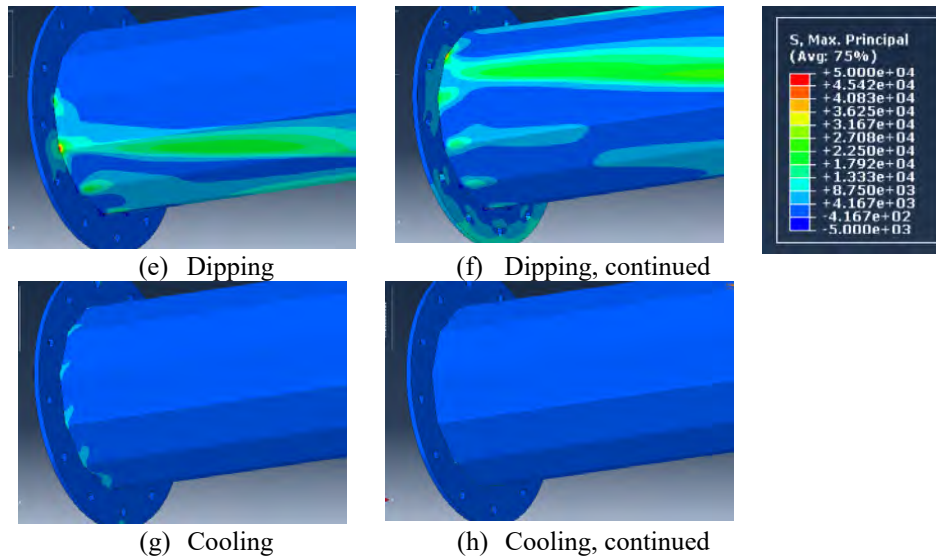


Figure D-31. Calculated stress demands for model 9, 12-sided pole, 5/16 in. thick, and 1 in. thick baseplate.

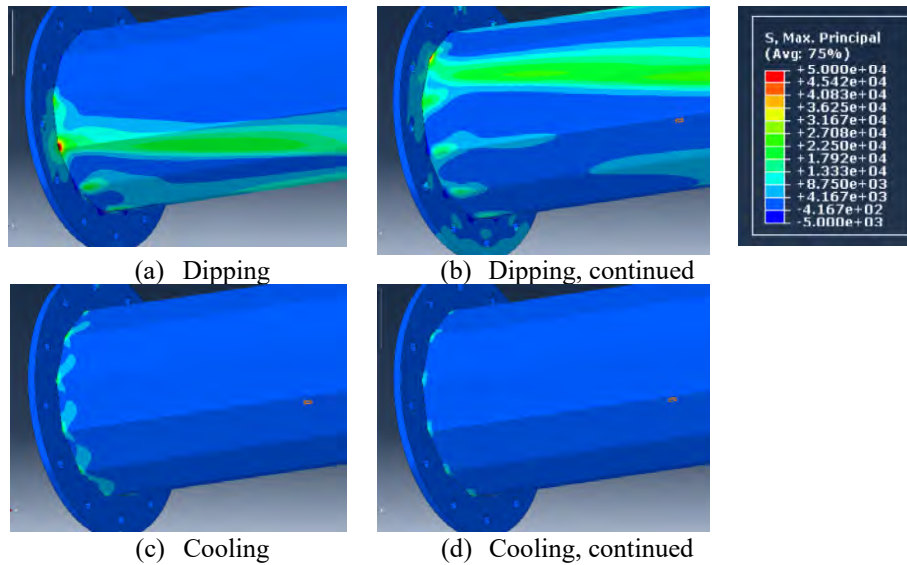


Figure D-32. Calculated stress demands for model 10, 12-sided pole, 5/16 in. thick, and 1.5 in. thick baseplate.

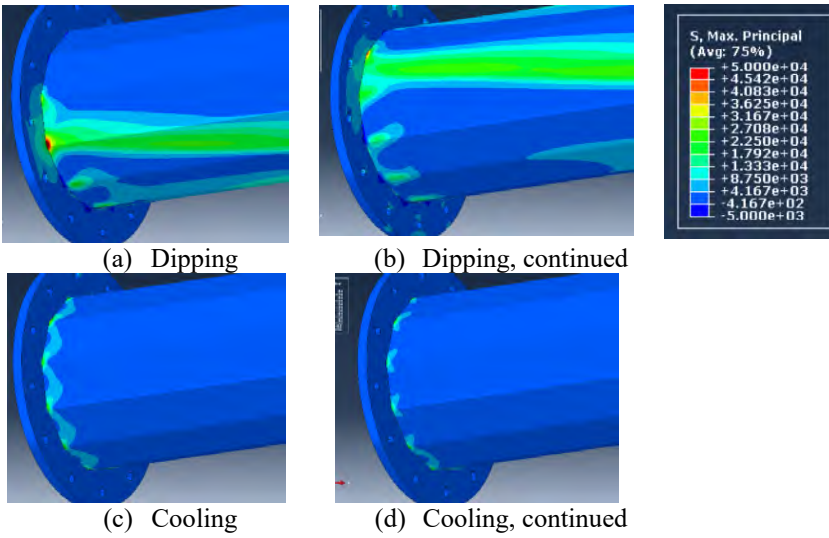


Figure D-33. Calculated stress demands for model 11, 12-sided pole, 5/16 in. thick, and 2 in. thick baseplate.

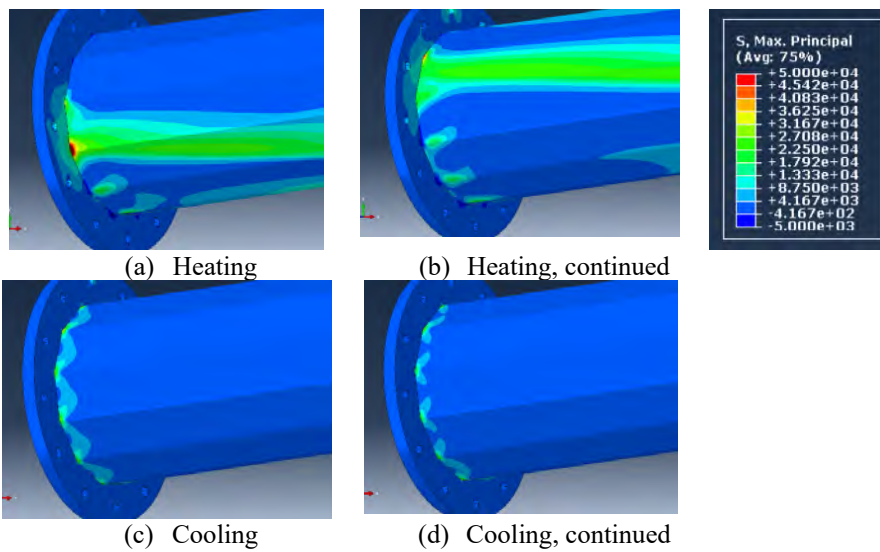
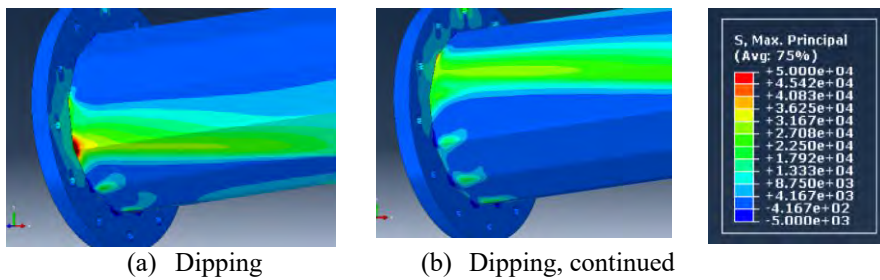


Figure D-34. Calculated stress demands for model 12, 12-sided pole, 5/16 in. thick, and 2.5 in. thick baseplate.



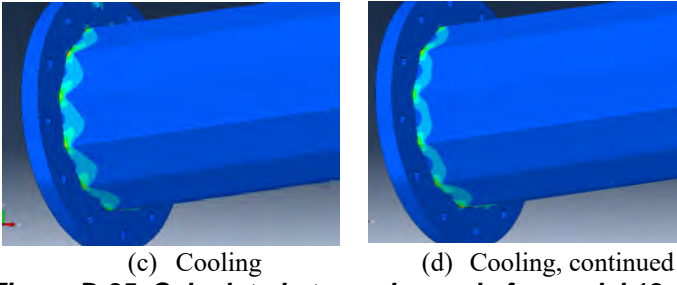


Figure D-35. Calculated stress demands for model 13, 12-sided pole, 5/16 in. thick, and 3.5 in. thick baseplate.

Inelastic strain demands for all models with 5/16 in. pole thickness are shown in Figure D-36, from paths on the inner and outer surfaces of the poles. Peak inelastic strain demands decreased with increasing plate thickness, a trend consistent with the stress fields shown.

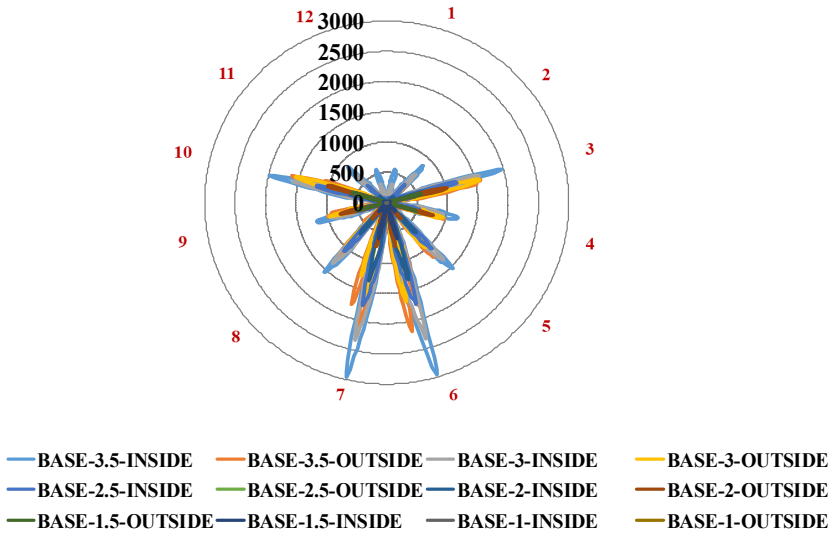
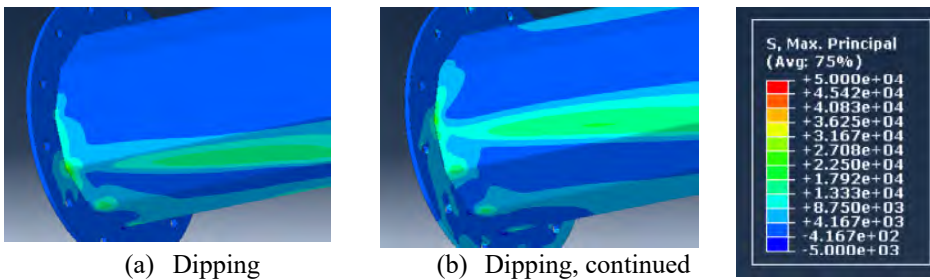


Figure D-36. Calculated inelastic strain demands for 12-sided poles, 5/16 in. thick.

Figure D-37 through Figure D-42 show calculated stress fields for models of 12-sided poles with a thickness of 1/2 in. and base plate thickness ranging between 1 and 3.5 in. These figures show that stress demands also increased with plate thickness at the time when the level of the zinc bath reached Bend 10. Stress demands in models with a pole thickness of 1/2 in. were significantly lower than those calculated in models with a pole thickness of 5/16 in.



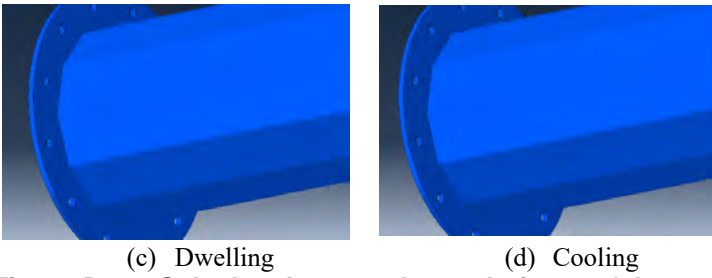


Figure D-37. Calculated stress demands for model 14, 12-sided pole, 1/2 in. thick, and 1 in. thick baseplate.

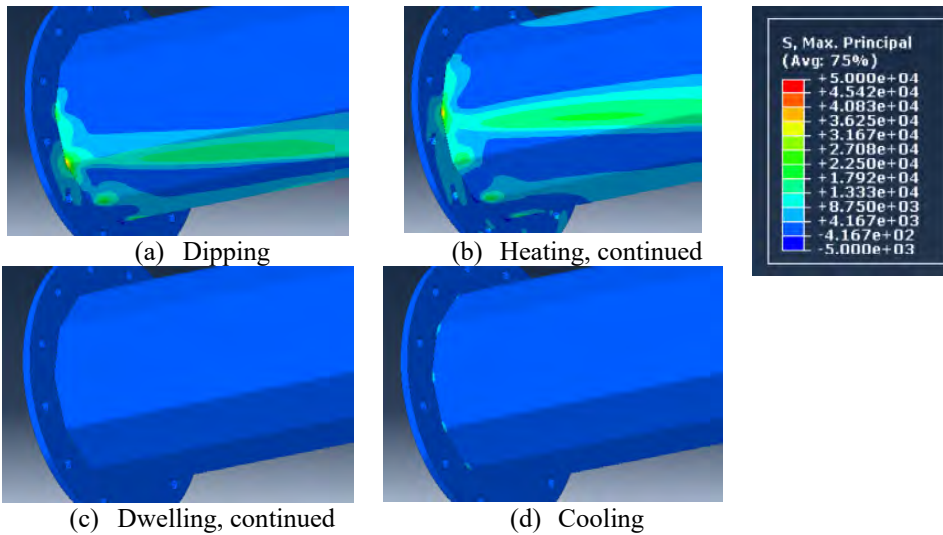


Figure D-38. Calculated stress demands for model 15, 12-sided pole, 1/2 in. thick, and 1.5 in. thick baseplate.

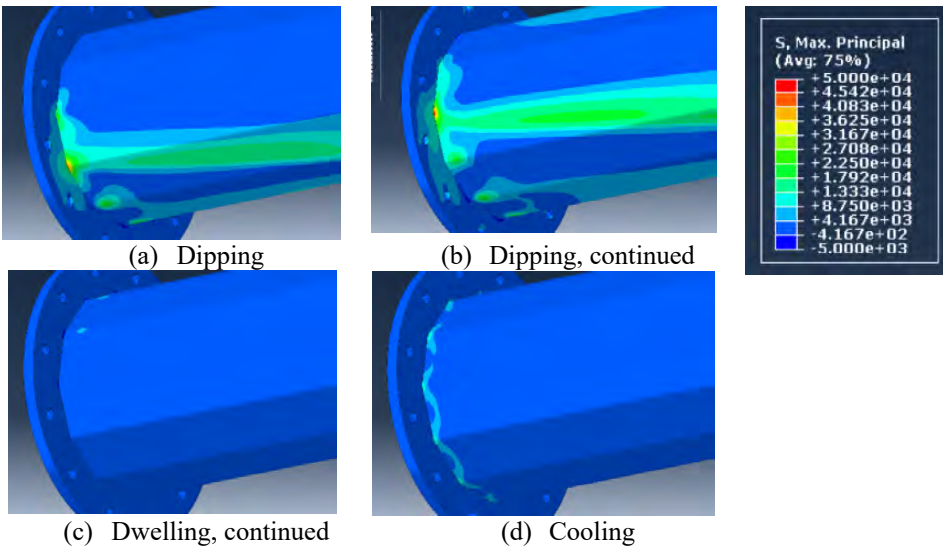


Figure D-39. Calculated stress demands for model 16, 12-sided pole, 1/2 in. thick, and 2 in. thick baseplate.

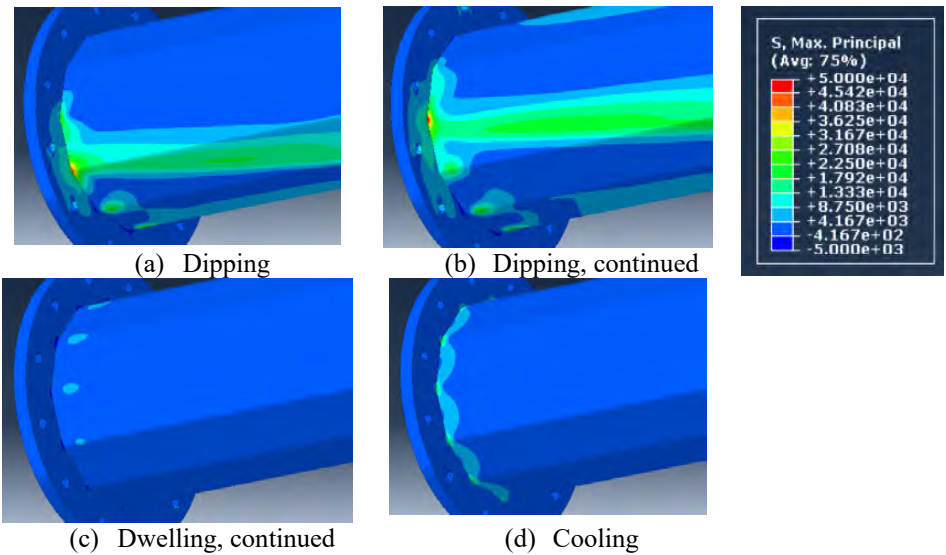


Figure D-40. Calculated stress demands for model 17, 12-sided pole, 1/2 in. thick, and 2.5 in. thick baseplate.

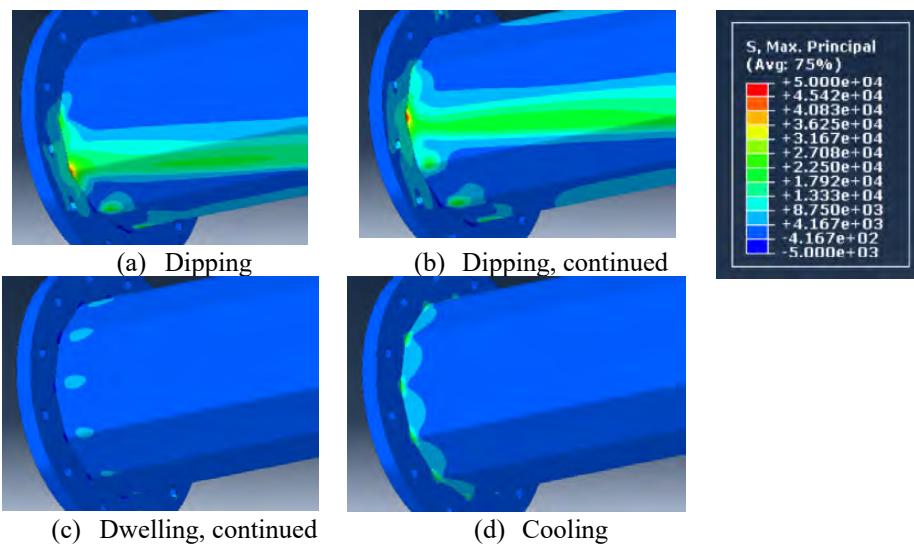
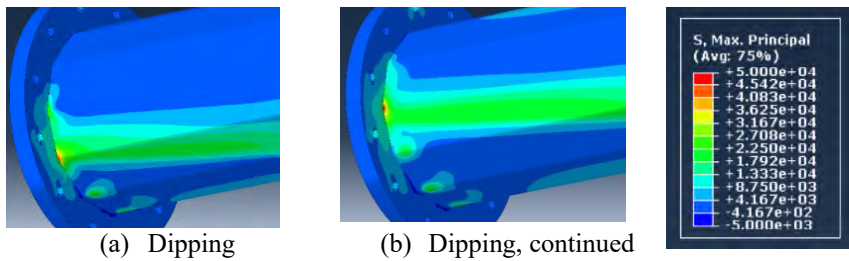
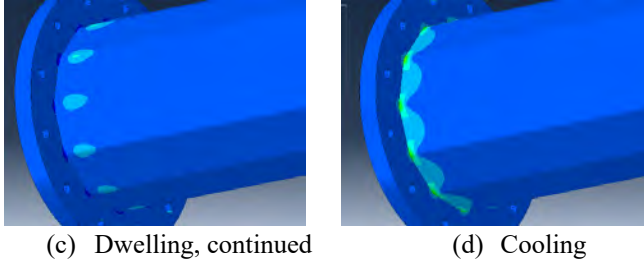


Figure D-41. Calculated stress demands for model 2, 12-sided pole, 1/2 in. thick, and 3 in. thick baseplate.





(c) Dwelling, continued (d) Cooling
Figure D-42. Calculated stress demands for model 18, 12-sided pole, 1/2 in. thick, and 3.5 in. thick baseplate.

Inelastic strain demands for all models with 1/2 in. pole thickness are shown in Figure D-43, extracted from paths on the inside and outside surfaces of the poles. Peak inelastic strain demands also decreased with increasing plate thickness, although they were significantly lower than inelastic strain demands calculated in poles with a thickness of 5/16 in.

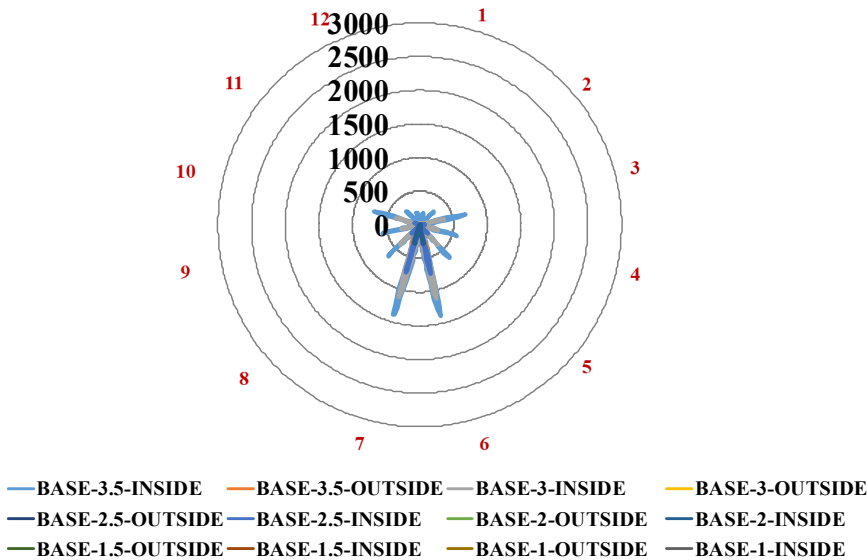


Figure D-43. Calculated inelastic strain demands for 12-sided poles, 1/2 in. thick.

Table D-1, Table D-2, and Table D-3 present the nonlinear analysis results for the models included in the study, in terms of PEEQ. Results are presented in terms of PEEQ at the end of each analysis, plotted radially around the critical section at the base plate. PEEQ strains were extracted from two different paths on the inner and outer surface of the pole (Figure D-44).

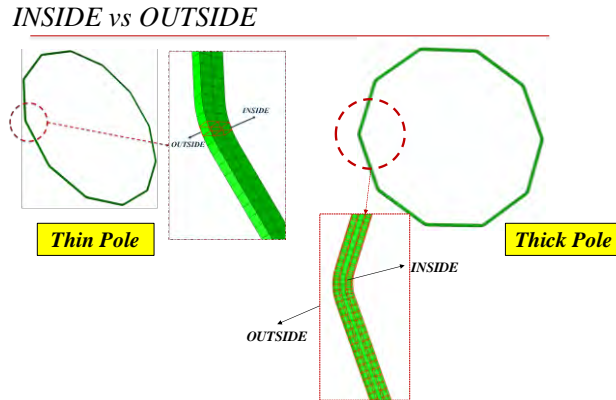
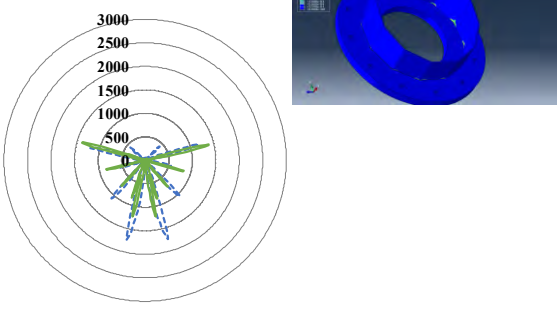
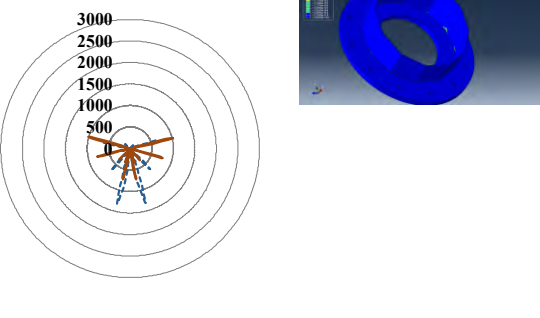
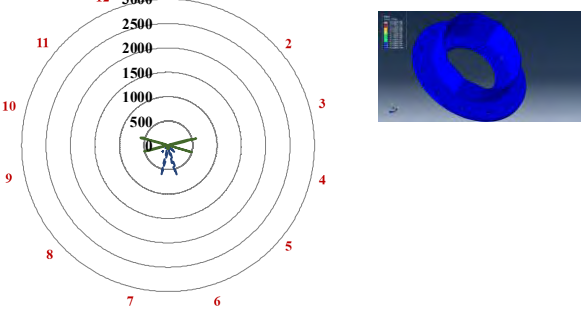
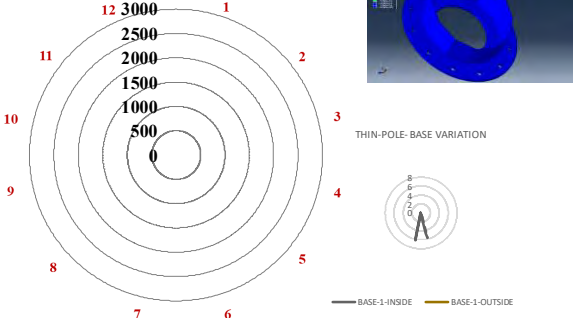


Figure D-44. Locations where PEEQ results were extracted

Table D-1: Analysis results of thin poles (5/16 in.) with varying base plate thickness

Radar charts of PEEQ (unit: $\mu\epsilon$)	Notes:
<p style="text-align: center;">BASE 3.5- THIN POLE (5/16 in.)</p> <p style="text-align: center;">--- BASE-3.5-INSIDE ——— BASE-3.5-OUTSIDE</p>	<p>Model # 13 Base plate thickness = 3.5 in. Pole thickness = 5/16 in. B P ratio = 11 Maximum calculated PEEQ = 3000 $\mu\epsilon$</p>
<p style="text-align: center;">BASE 3- THIN POLE (5/16 in.)</p> <p style="text-align: center;">--- BASE-3-INSIDE ——— BASE-3-OUTSIDE</p>	<p>Model # 1 Base plate thickness = 3 in. Pole thickness = 5/16 in. B P ratio = 9.6 Maximum calculated PEEQ = 2350 $\mu\epsilon$</p>

<p>BASE 2.5- THIN POLE (5/16 in.)</p>  <p>--- BASE-2.5-INSIDE ——— BASE-2.5-OUTSIDE</p>	<p>Model # 12 Base plate thickness = 2.5 in. Pole thickness = 5/16 in. B P = 8 Maximum recorded PEEQ = 1650 $\mu\epsilon$</p>
<p>BASE 2- THIN POLE (5/16 in.)</p>  <p>--- BASE-2-INSIDE ——— BASE-2-OUTSIDE</p>	<p>Model # 11 Base plate thickness = 2 in. Pole thickness = 5/16 in. B P ratio = 6.4 Maximum recorded PEEQ = 850 $\mu\epsilon$</p>
<p>BASE 1.5- THIN POLE (5/16 in.)</p>  <p>--- BASE-1.5-INSIDE ——— BASE-1.5-OUTSIDE</p>	<p>Model # 10 Base plate thickness = 1.5 in. Pole thickness = 5/16 in. B P ratio = 4.8 Maximum recorded PEEQ = 550 $\mu\epsilon$</p>
<p>BASE 1- THIN POLE (5/16 in.)</p>  <p>--- BASE-1-INSIDE ——— BASE-1-OUTSIDE</p> <p>THIN-POLE-BASE VARIATION</p>	<p>Model # 9 Base plate thickness = 1 in. Pole thickness = 5/16 in. B P ratio is 3.2 Maximum recorded PEEQ = 7 $\mu\epsilon$</p>

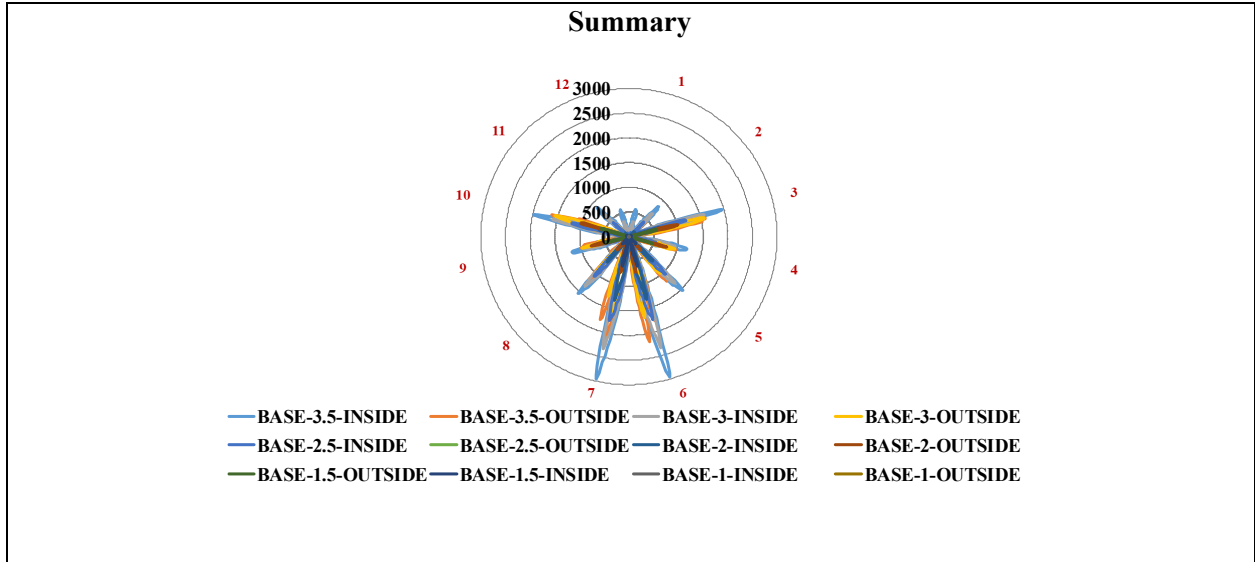
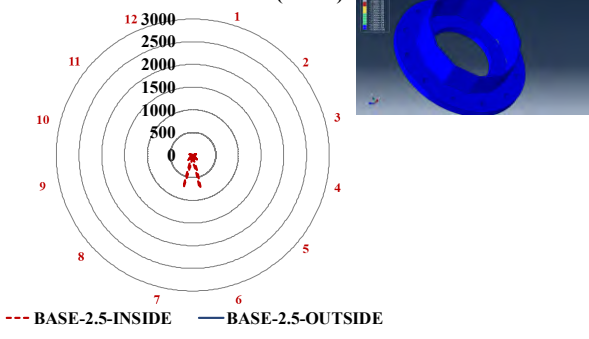
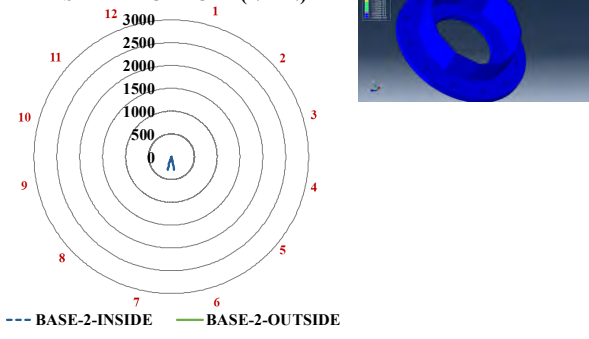
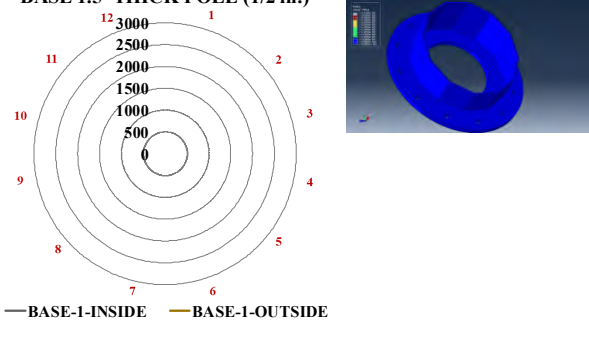
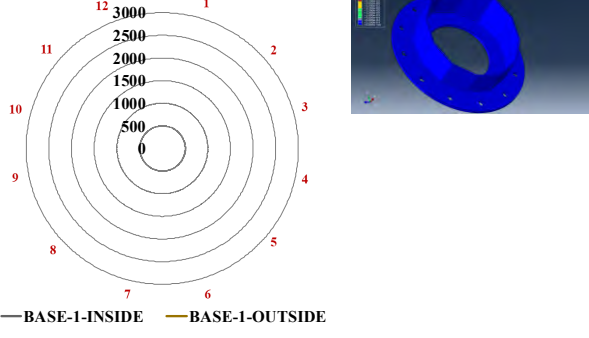


Table D-2: Analysis results of thick poles (1/2 in.) with varying base plate thickness

Radar charts of PEEQ (unit: $\mu\epsilon$)	Notes:
<p style="text-align: center;">BASE 3.5- THICK POLE (1/2 in.)</p> <p style="text-align: center;"> --- BASE-3.5-INSIDE — BASE-3.5-OUTSIDE </p>	<p>Model # 18 Base plate thickness = 3.5 in. Pole thickness = 1/2 in. B P ratio = 7 Maximum recorded PEEQ = 1450 $\mu\epsilon$</p>
<p style="text-align: center;">BASE 3- THICK POLE (1/2 in.)</p> <p style="text-align: center;"> --- BASE-3-INSIDE — BASE-3-OUTSIDE </p>	<p>Model # 2 Base plate thickness = 3 in. Pole thickness = 1/2 in. B P ratio is 6 Maximum recorded PEEQ = 1050 $\mu\epsilon$</p>

<p>BASE 2.5- THICK POLE (1/2 in.)</p>  <p>--- BASE-2.5-INSIDE — BASE-2.5-OUTSIDE</p>	<p>Model # 17 Base plate thickness = 2.5 in. Pole thickness = 1/2 in. B P ratio is 5 Maximum recorded PEEQ = 650 $\mu\epsilon$</p>
<p>BASE 2- THICK POLE (1/2 in.)</p>  <p>--- BASE-2-INSIDE — BASE-2-OUTSIDE</p>	<p>Model # 16 Base plate thickness = 2 in. Pole thickness = 1/2 in. B P ratio is 4 Maximum recorded PEEQ = 40 $\mu\epsilon$</p>
<p>BASE 1.5- THICK POLE (1/2 in.)</p>  <p>— BASE-1-INSIDE — BASE-1-OUTSIDE</p>	<p>Model # 15 Base plate thickness = 1.5 in. Pole thickness = 1/2 in. B P ratio is 3 Maximum recorded PEEQ= 0 $\mu\epsilon$</p>
<p>BASE 1- THICK POLE (1/2 in.)</p>  <p>— BASE-1-INSIDE — BASE-1-OUTSIDE</p>	<p>Model # 14 Base plate thickness = 3.5 in. Pole thickness = 1/2 in. B P ratio is 2 Maximum recorded PEEQ = 0 $\mu\epsilon$</p>

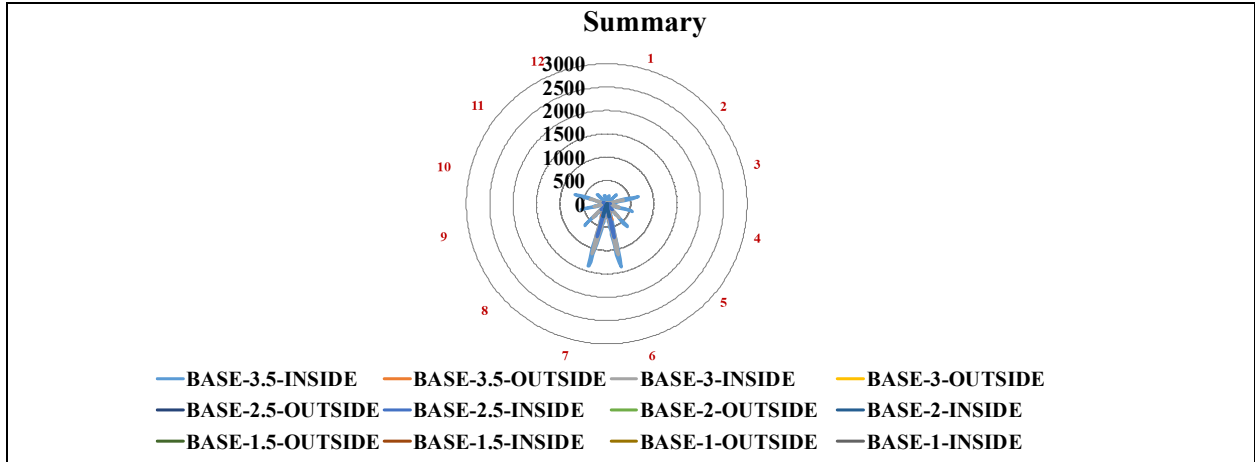
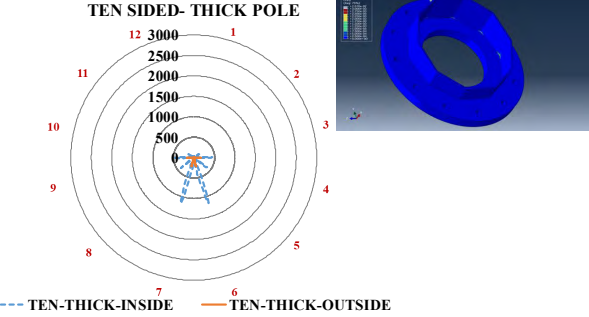
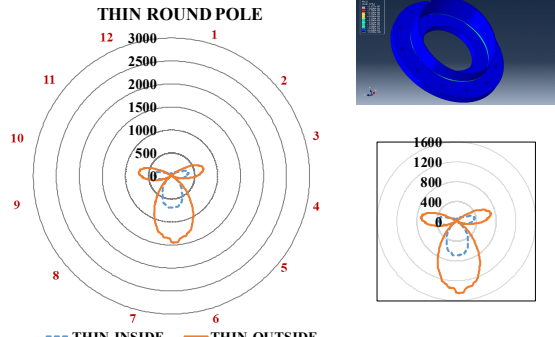
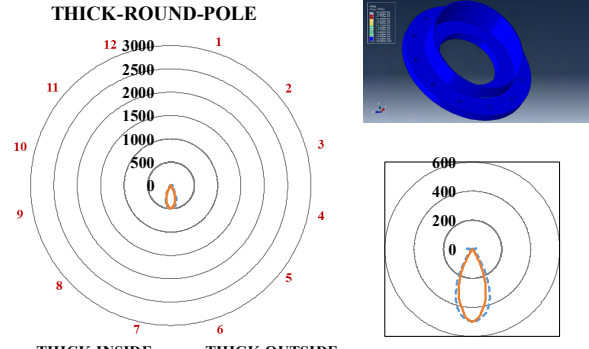


Table D-3: Analysis results of poles with geometric variants (Base plate thickness: 3 in.)

Radar charts of PEEQ (unit: $\mu\epsilon$)	Notes:
<p style="text-align: center;">EIGHT SIDED- THICK POLE</p> <p style="text-align: center;"> --- EIGHT-THICK-INSIDE --- EIGHT-THICK-OUTSIDE </p>	<p>Model # 7 Base plate thickness = 3 in. B P ratio = 6 Maximum recorded PEEQ = 1100 $\mu\epsilon$</p>
<p style="text-align: center;">TEN SIDED- THIN POLE</p> <p style="text-align: center;"> --- TEN-THIN-INSIDE --- TEN-THIN-OUTSIDE </p>	<p>Model # 5 Base plate thickness = 3 in. B P ratio is 9.6 Maximum recorded PEEQ = 2300 $\mu\epsilon$</p>

<p>TEN SIDED- THICK POLE</p>  <p>--- TEN-THICK-INSIDE — TEN-THICK-OUTSIDE</p>	<p>Model # 8 Base plate thickness = 3 in. B P ratio = 6 Maximum recorded PEEQ = 1100 $\mu\epsilon$</p>
<p>THIN ROUND POLE</p>  <p>--- THIN-INSIDE — THIN-OUTSIDE</p>	<p>Model # 3 Base plate thickness = 3 in. B P ratio is 9.6 Maximum recorded PEEQ = 1500 $\mu\epsilon$</p>
<p>THICK-ROUND-POLE</p>  <p>--- THICK-INSIDE — THICK-OUTSIDE</p>	<p>Model # 6 Base plate thickness = 3 in. B P ratio is 6 Maximum recorded PEEQ = 500 $\mu\epsilon$</p>